Irina Nicoleta Cimalla

AlGaN/GaN sensors for direct monitoring of fluids and bioreactions

AlGaN/GaN sensors for direct monitoring of fluids and bioreactions

Irina Nicoleta Cimalla

Universitätsverlag Ilmenau
2011

Impressum

„Unde dragoste nu e, nimic nu e"
„Wo Liebe nicht ist, ist gar nichts"

Marin Preda:
„Cel mai iubit dintre pamanteni"

Abstract

In this thesis, AlGaN/GaN heterostructures, which have shown to be reliable pH sensors, have been characterized and further developed for the *in situ* monitoring of cell reactions. For this reason, NG108-15 nerve cells were cultivated on sensor surfaces and their response on different neuroinhibitors was clearly monitored.

First, a measurement setup for extracellular recording was designed in connection with an improved chip design and sensor technology. To select optimal sensors for the cell-transistor coupling, heterostructures grown by PIMBE and MOCVD were characterized with respect to electronic transport properties and their performance as pH sensor in well defined pH buffer solutions.

Generally, a good proliferation of different cell lines was observed on AlGaN and GaN surfaces without using any kind of thin films of organic material for improving of the cellular adhesion and biocompatibility. The impact of several technology- and sensing-relevant treatments on the surface properties of AlGaN/GaN sensors was studied. For a deeper understanding of the mechanisms in cell-transistor coupling, the stability of the media for cell-transistor measurements was studied. In an open setup with contact to normal atmosphere, the monitoring of the spontaneous cell activity ("breathing") was recorded, that is not the case for covered measurement setup due to reduced gas exchange with the environment. The sensor sensitivity to potential changes by Na^+ and K^+ ions and their reactions with neurotoxin were also confirmed. By titration in complex electrolytes and by cultivating NG108-15 nerve cells on the sensor surface, it was demonstrated that these sensors are able to monitor complex cell reactions. The calculations using simulation of the heterostructure as well as simplified expressions for the ion flux give strong evidence that the signal in the cell-transistor coupling experiments is primarily generated by the Na^+ flux. A fairy good agreement between the experimental observations and the model could be found.

In conclusion, the AlGaN/GaN-ISFETs show stable operation under physiological conditions, exhibit a very good signal resolution and are suitable for long-time monitoring of cell reactions on different stimuli.

Zusammenfassung

In dieser Arbeit wurden AlGaN/GaN-Heterostrukturen, die ein hohes Potenzial für pH-Sensoren aufweisen, charakterisiert und weiterentwickelt für die elektronische Erfassung von Zellreaktionen. Dazu wurden NG108-15 Nervenzellen auf den Sensoroberflächen kultiviert und deren Antwort auf Stimulierung mit verschiedenen Neuroinhibitoren aufgezeichnet.

Zunächst wurde ein Messaufbau für das Erfassen extrazellularer Potenzialänderugen entworfen und das bestehende Chipdesign sowie die Herstellungstechnologie weiterentwickelt. Für die Auswahl optimaler Sensoren für die Transistor-Zell-Kopplung wurden sowohl mittels PIMBE und MOCVD gewachsene Heterostrukturen charakterisiert bezüglich ihrer elektronischen Transporteigenschaften und ihres Verhaltens als pH-Sensor.

Auf AlGaN- und GaN-Oberflächen konnte eine sehr gute Kultivierung verschiedener Zelllinien erzielt werden ohne die sie sonst übliche Verwendung organischer Zwischenschichten zur Erhöhung von Adhäsion (z.B. Fibroplasten). Der Einfluss verschiedener Technologie- und sensorrelevanter Behandlungsschritte auf die Oberflächeneigenschaften der AlGaN/GaN-Sensoren wurde untersucht und die Medienstabilität bzw. Wechselwirkungen wurden analysiert. In einem offenen Setup mit Gasaustausch zur Umgebung wurde eine spontane Zellaktivität erfasst („Zellatmung"), die in einem abgeschlossenen Setup aufgrund des reduzierten Gasaustausches nicht auftrat. Weiterhin wurde die Empfindlichkeit des Sensors auf Potenzialänderungen durch Na^+ and K^+ Ionen und deren Reaktionen mit Neurotoxinen bestätigt. Durch Titration in komplexe Elektrolyte und durch Kultivierung von NG108-15 Nervenzellen auf der Sensoroberfläche wurde demonstriert, dass die Sensoren in der Lage sind, komplexe Zellreaktionen zu erfassen. Berechnungen mit Hilfe von Simulationen und vereinfachten analytischen Beschreibungen für die Ionenflüsse belegten, dass bei der Zell-Transistor-Kopplung das Sensorsignal im Wesentlichen durch die Na^+-Flüsse erzeugt wird. Die experimentellen Beobachtungen und die theoretische Modellierung zeigte dafür eine gute Übereinstimmung. Zusammenfassend wurde in dieser Arbeit gezeigt, dass AlGaN/GaN-ISFETs stabil unter physiologischen Bedingungen arbeiten, sehr gute Signalauflösung ermöglichen und für Langzeitmessungen mit lebenden Zellen geeignet sind.

i Table of contents

ii List of acronyms

2DEG ....two-dimensional electron gas
ac....................alternating current
ACh.................acetylcholine
AChE ....acetylcholinesterase
AES.................Auger electron spectroscopy
AFM................atomic force microscopy
AlGaN ....aluminum gallium nitride
AlN.................aluminum nitride
APS ....3 aminopropyl triethoxysilane
APTES ....aminopropyltriethoxysilane
APTMS ....aminopropyltrimethoxysilane
ATCC..............American tissue-type culture collection
ATP.................adenosine triphosphate
BioFET............biosensing ISFET
BSA.................bovine serum albumin
c-EnFET..........EnFET with covalent immobilization of enzymes
CHO-K1 ....Chinese hamster ovary cells
CPFET ....cell-based field effect transistor (cell-potential FET)
C-V..................capacity-voltage (measurements)
CVD ....chemical vapor deposition
dc....................direct current
DEP.................dielectrophoretic alignment
DFP ....diisopropylfluorophosphate
DMEM............Dulbecco's modified Eagle's medium-high glucose
DMSO.............dimethyl sulfoxide
DNA................deoxyribonucleic acid
DNA-FET ....DNA-modified field effect transistor
dsDNA ....double stranded DNA
EBSS...............Earle's buffered saline
ECR.................electron cyclotron resonance
EGFET............electrolyte gate field effect transistor
ELISA ....enzyme-Linked ImmunoSorbent Assay
EnFET.............enzyme-modified field effect transistor
FCS ....fetal calf serum

FET .... field effect transistor
ImmunoFET ... immunologically modified field effect transistor
ISFET .... ion sensitive field effect transistor
FWHM .... full width at half maximum
GaN .... gallium nitride
GBSS.............. Gey's buffered saline
HBSS.............. Hank's buffered saline
HEK 293FT ... Human embryonal kidney
HEMT .... high electron mobility transistors
HEPES .... n-2-hydroxyethylpiperazine-n'-2-ethanesulfonic acid
ICP .... inductively coupled plasma
InN .... indium nitride
LDH .... lactate dehydrogenase
LTCC .... low temperature cofired ceramics
MBE .... molecular beam epitaxy
MEA............... multi electrode array
MEMS .... microelectromechanical system
MIF................. metal ion free
MOCVD......... metal-organic chemical vapor deposition
MPTMS......... mercaptopropyltrimethoxysilane
MT.................. Mettler-Toledo
NG 108-15...... euroblastoma-glioma hybrid nerve cell line
o.n.................. over night
ODTMS.......... octadecyltrimethoxylane
p-EnFET......... EnFET with physisorption of enzymes
PBC .... printed board circuits
PBS................. phosphate buffered saline
PIMBE............ plasma induced molecular beam epitaxy
PMSF .... phenylmethanesulphonylfluoride
PSA .... prostate specific antigen
PVC................ polyvinylchloride
RHEED .... reflection high-energy electron diffraction
RIE .... reactive ion etching
RNA .... ribonucleic acid
RT................... room temperature
SCI .... substituted cell media with ion concentration as in cells
SCR .... substituted cell media with reduced concentration of ions
SCZ .... substituted cell media with zero ions

14

SEM ....scanning electron microscopy
ssDNA.............single stranded DNA
TEA.................quaternary ammonium ion
TEM ....transmission electron microscopy
TLM ....transmission line method
TMAH.............tetramethylammoniumhydroxide
TRIS 2-amino-2-hydroxymethyl-propane-1,3-diol
TTX.................tetrodotoxin
UV...................ultraviolet
XPS ....X-ray photoelectron spectroscopy
XRD ....X-ray diffraction
XRR ....X-ray reflectivity
ZMN...............Centre of Micro and Nanotechnologies

iii List of symbols

a ....lattice constant [Å]
A ....(contact) area [m²]
a_{Me} ....activity of one type of ions (Me)
b ....bowing parameter
B ....magnetic flux density [T]
c ....lattice constant [Å]
C......................capacitance [F]
   C_{ox} .... gate insulator capacitance [F]
C_{31}, C_{33} ....elastic constants [GPa]
C_a, C_b...............analytical concentrations of acid HA and base B
C^i_{ion}.................ion concentration inside a cell [mol]
C^o_{ion} ....ion concentration outside a cell [mol]
c_M ....specific membrane capacitance [F]
d ....(barrier) thickness [nm]
e......................electron charge ($1.602*10^{19}$ As)
e_{31}, e_{33}..............piezoelectric constants [C/m²]
E_C ....conduction band minimum [eV]
  ΔE_C.............. .... conduction band offset at an interface [eV]
$E_F(x)$ ....Fermi level [eV]

E_g .... energy gap (300K) [eV]

E_{ion} .... equilibrium potential [mV]

E_{ref} .... reference electrode potential relative to vacuum [V]

E_V .... valence band maximum [eV]

F .... Faraday constant (9.648×10^4 C/mol)

F .... Lorentz force [N]

f_p .... dissociation fraction

g_m .... transconductance [S]

I .... electrical current [A]

$\quad I_D$ .... (drain-source) channel current

$\quad I_{D,0}$ .... at the time $t = 0$

$\quad I_{D,e}$ .... at $t \rightarrow \infty$ (equilibrium value)

K_a, K_b .... acid, base ionization constant

K_W .... water equilibrium constant

L .... (channel) length [μm]

$\quad L_{act}$ .... active area length

$\quad L_{real}$ .... drain-source distance

L .... correlation length [Å]

n .... (bulk) electron concentration [cm^{-3}]

n .... number of exchanged electrons

$n_{cleft}(K^+)$ .... concentration of K^+ ions in the cleft

$n_{cleft}(Na^+)$ .... Na^+ ions in the cleft [cm^{-3}]

$n_{flow}(Na^+)$ .... Na^+ ions flux [cm^{-2}s^{-1}]

N_{CV} .... carrier concentration from C-V [cm^{-3}]

$N_{disl.}$ .... threading dislocation density [cm^{-2}]

n_s .... sheet carrier concentration [cm^{-2}]

N_s .... surface sites [cm^{-2}]

pH .... negative decimal logarithm of [H^+]

q .... elementary charge

$\qquad$ (q = -e for electrons and q = +e for holes)

Q .... charge [As]

$\quad Q_B$ .... depletion charge in the AlGaN

$\quad Q_{ox}$ .... fixed oxide charge

$\quad Q_{SS}$ .... surface state charges

Q .... concentration or activity quotient

R .... gas constant (8.315 J*K^{-1}*mol^{-1})

R .... (channel) resistance [Ω]

$\quad R_s$ .... sheet resistance [Ω/]

R_H ....Hall coefficient [cm³/Vs]

rms ....root-mean-square (roughness) [nm]

S ....sensitivity of the sensors

   S_{pH} .... in constant current mode [mV/pH]

   $S_{I,pH}$............ .... in constant voltage mode [µA/pH]

t ....time

T ....absolute temperature [K]

u ....internal Cell parameter [Å]

U....................voltage [V]

   U_{DS} .... drain source voltage

   U_{GS} .... gate source voltage

   U_H............. .... Hall voltage

   U_{ref}............ .... reference voltage

V ....volume [m³]

v ....particle velocity [m/s]

V_m ....resting potential [mV]

W ....(channel) width [µm]

x ....Al concentration

Δ ....interface roughness [Å²]

χ_{so} ....interface potential at the gate oxide-electrolyte interface [V]

ε_0 ....dielectric constant ($8.85*10^{-14}$ C/Vcm)

   $\varepsilon_r, \varepsilon(x)$ .... relative dielectric constant

$\varepsilon_x, \varepsilon_y, \varepsilon_z$ ....strain in corresponding directions x,y,z

$\phi_b(x)$.................Schottky-barrier [eV]

ϕ_{AlGaN} ....work function of AlGaN [eV]

Φ_F...................Fermi-potential [V]

$\Delta\varphi$ ....electrical potential difference at a solid/liquid interface [V]

μ.....................(electron) mobility [cm²/Vs]

ρ....................specific resistivity [Ωcm]

σ ....specific conductivity [S/cm]

τ....................time constant [s]

Ψ_0 ....surface potential [V]

1. Introduction

Mammalian neuronal cells represent one of most sophisticated and complex signaling and processing systems in any living organisms. Many diseases (such as Alzheimer's and Parkinson's disease or amyotrophic lateral sclerosis to name only a few) have there background in disturbed processes on nerve cells. The study of the mechanisms of the physiological changes in nerve cells, which are induced by stressors such as neuroinhibitors or analgesics, represent one way to obtain helpful information for understanding such neural disorders and open the way for the development of treatments. However, new drugs for efficient treatments of such diseases are the products of a long development process, the first step of which is often the discovery of a new enzyme inhibitor. In the past, the only way to identify such novel inhibitors was by trial and error: screening huge libraries of compounds against a target enzyme and studying the response with the hope that useful results would emerge. This "brute force" approach is to some extend successful and has even been extended by combinatorial chemistry approaches that quickly produce large numbers of novel compounds as well as by the high-throughput screening technologies to rapidly screen these huge chemical libraries for useful inhibitors. Despite the increasing demand for high-throughput functional screening methods in the areas of environmental protection, toxicology and drug development [1-5] these methods are not yet efficient in case of cellular measurements [3, 5, 6].

In pharmacology it is important to study the side effect spectrum of a given compound, thus, the application of complex functional tests at the whole-organism-level are necessary [7, 8]. To assess the global toxicity of the wide variety of chemicals that are possible drugs, the research on functional cells using biosensors could be more effective than pure physico-chemical methods [9]. In the last years, the application of whole-cell biosensors for toxin detection, drug screening and recording of cell action potential has developed from an academic principle to an accepted method [9-19]. Already in the early fifties, Hodgkin and Huxley studied the electrical properties of single cells by impaling the cellular membrane with carefully designed glass microelectrodes. With this procedure, the action potential of the neuronal cells was recorded and the presence of voltage gated ion channels has been demonstrated [20]. Two decades later, further

improvement of this method lead to the development of the patch-clamp technique by Neher and Sakmann (1976) [21]. In this case, the glass electrode is placed close to the cell membrane and a low impedance electrical contact to the cells interior is established [22]. Using this whole-cell configuration, the investigation of voltage gated ion-channel ensembles or even the function of single ion-channels on the cell membrane are studied. However, this novel and nowadays widely accepted method for medical, pharmaceutical and physiological research exhibited some disadvantages. The patch-clamp procedure is mostly complicated to handle, is invasive and it invariably destroys the cell after measurement. It is also limited to observe only a few cells at the same time and long time measurements are not feasible as the cells are subjected to a high degree of stress during a patch clamp measurement, which makes an observation over several hours impossible.

Almost in the same time with the development of the patch-clamp system, a planar microelectrode array for the recording of extracellular electrical activity of cells cultured *in vitro* was designed by Thomas *et al.* (1972) [23]. The system was created using gold plated nickel electrodes of known spacing and size on a glass substrate passivated with patterned photo resist. A glass ring was fixed to the substrate with wax to form a culture chamber. Using Thomas's techniques, eventually with slightly improvements, numerous researchers have utilized microelectrodes arrays to examine a wide variety of cell types under different conditions. In this mode the first recording of extracellular electrical responses from explanted neural tissue was reported by Gross *et al.* (1977) [24]. Only a few years later (1980), Pine *et al.* proposed to combine the two developed methods: a glass micropipette inserted through the cell membrane and a microelectrode array, in order to record in the same time the intracellular and extracellular signal, respectively, from dissociated neurons [25]. This was an important simultaneous experiment for the validation of the extracellular technique and a calibration of the recorded extracellular signal for comparison with the large number of available data on intracellular recording in the literature. Pine was also the first who replaced the organic photo resist passivation layer with silicon dioxide in order to use standard silicon chip processing technologies. Based on the structure and techniques mentioned above the study on cultured cells was continued by numerous research groups examining many different cell types over the years [26-30].

In 1991, Fromherz *et al.* [12] launched a new era of biosensing by utilization of an integrated field effect transistor (FET) as the sensing element instead of the previously used bare metal electrodes. The extracellular signal from single dissociated cells, which were manually placed on transistor, was recorded. A glass micropipette was inserted through the cell membrane and used to stimulate the cell and monitor the intracellular voltage. Later, Fromherz used similar systems to explore the physical characteristics of the neuron-silicon junction using an array of transistors positioned below the neurons [31] as well as capacitive stimulation of the neuron through a thin oxide layer [32].

Basic sensing element is the pH sensitive FET proposed by Bergveld in 1970 [33], which initiated a large number of publications devoted to ion sensitive FETs (ISFETs) based on the established silicon technology. A historical overview, which also highlights future challenges and possibilities, is given by Bergveld [34]. Silicon based biosensing ISFETs (BioFETs) were further classified as enzyme-modified FETs (EnFET), immunologically modified FETs (ImmunoFET), DNA-modified FETs (DNA-FET) and cell-based (or cell-potential) FETs (CPFET) [35, 36]. Despite high prospects and promising demonstrations of these devices, the fact that they are based on silicon technology, while being beneficial for mass production, impairs their long-term chemical stability and thus, limits the areas of application [37]. This triggered the search for new functional and passivating surface layers which has not yet lead to entirely satisfying results or to commercial available devices employing BioFETs.

At the beginning of this decade, a novel ISFET based on the group III-nitrides (GaN, AlN and alloys) was reported. Group III-nitrides exhibit a number of superior properties compared to Si or conventional III-V semiconductors, which make them promising candidates for biosensors [38-40]. In 2003 Steinhoff *et al.* reported the first application of these ISFETs for pH sensing [41]. Two years later, the same authors reported the recording of action potential from hearts muscle cells using sensor arrays and demonstrated the superior electrical characteristics of ISFETs based on group III-nitrides compared to similar devices based on Si technology [19].

For future applications, the basic understanding of the recorded signals is still a crucial precondition. In the present study, ISFETs based on an AlGaN/GaN heterostructure are further characterized with respect to the coupling to nerve cells in order to enable the application in CPFETs. The present approach involves the following major tasks:

➤ The previously developed extracellular sensors and the extracellular recording systems [41, 42] as well as the stability of the setup are improved.

➤ The biocompatibility and the impact of the typical device processing steps on the reaction of living cells is evaluated

➤ The neuroblastoma-glioma hybrid NG 108-15 nerve cell line as a cellular system for the extracellular sensors is employed.

➤ The applicability and reliability of the nerve cell-to-FET hybrid system are investigated.

The thesis is organized as follows:

Chapter 2 will firstly describe the functions of electrically active nerve cells. An introduction is given how these systems communicate using weak electrical signals and what kind of influence neurotransmitters have in the neuronal function. Based in the function, the goal for biosensing and the requirements for the device will be derived.

Chapter 3 gives an introduction on the properties of group III-nitrides, which have been the materials of choice for the fabrication of biosensors in this work. Based on these properties, the function of the AlGaN/GaN heterostructure ISFETs is explained.

Chapter 4 summarizes the fabrication and the basic electrical characterization of the ISFETs.

Chapter 5 demonstrates the operation of the fabricated ISFET devices in aqueous solutions with special focus on pH sensing and corresponding significant parameters. A stable and well characterized pH sensor represents a major requirement for the subsequent biosensing experiments.

Chapter 6 focus on the biocompatibility of the ISFET surfaces, which is an indispensable precondition for the operation as CPFET. A review of possible functionalization of AlGaN/GaN ISFET with applicability on biosensing is also presented. Based on this studies,

Chapter 7 describes the Cell –Transistor Coupling and characterizes the sensor sensitivity to different ions. The investigation of the applicability of the NG 108 – 15 nerve cell – FET sensor hybrid system in terms of drug screening was performed by application of different neurotoxins to the cells. Finally,

Chapter 8 provides the conclusions from this work and proposes possible further developments of the cell – based biosensors.

The *Appendix* contains the detailed technological processes of AlGaN/GaN FET and the NG 108 - 15 nerve cells growth protocol.

2. Cellular function and response

The understanding of the electrical properties of cellular systems is essential for future coupling of living biological cells with the transistor chip. Cell biology cannot be fully understood without knowledge and understanding of biochemistry, metabolism, molecular biology and genetics of cells. Because this field is very diverse and represents not the scope of the present work, this chapter will focus on the basics of cellular function as it relates to electrical activity in cells. The cell is the basic unit of modern biology. Every organism is a system of many cells or is itself a single cell. To understand how the cells are constructed and how they carry out the intricate functions necessary for life is the key on the way to develop appropriate treatments for many diseases. Significant for this work is the dynamic nature of the cell, as evidenced by its capacity to grow, reproduce and become specialized, and by its ability to respond to stimuli and to adapt to changes in its environment.

2.1. Cellular construction

By observing through a microscope the empty cell walls of a dead plant tissue, Robert Hooke defines for first time the term cell – "*cellulae*" in Latin means "little rooms"[43]. Thanks to the improved microscopes, the English botanist Robert Brown found in the 1830s that every plant cell contained a rounded structure, which he called a "*nucleus*". In 1838 the German Matthias Schleiden came to the conclusion that all plant tissue were composed of cells and that an embryonic plant always arose from a single cell. For animal world, Theodor Schwann came to the same conclusion just one year later. Moreover, Schwann formulated also the cell theory, which stood the test of time and continues to provide the basis for our own understanding of the importance of cells and cell biology. The cell theory had two basic postulates:

➢ 1. All organisms consist of one or more cells.
➢ 2. The cell is the basic unit of structure for all organisms.

By 1855, Rudolf Virchow added a third postulate:

➢ 3. All cells arise only from pre-existing cells.

In this case the cell is not only the basic unit of structure for all organisms but also the basic unit of reproduction.
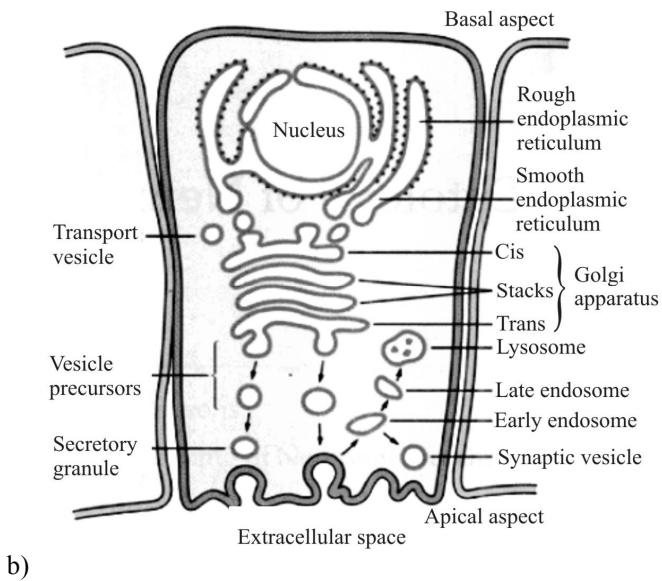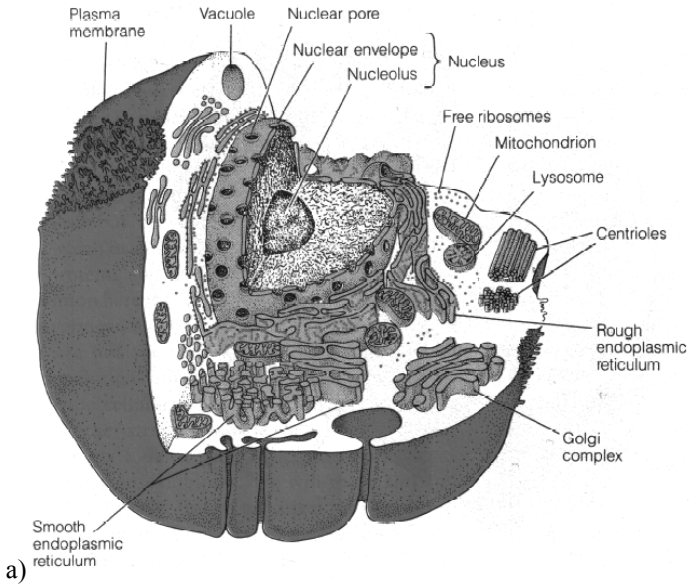
a)

b)

Fig. 2.1: (a) Different parts of a cell [43] and (b) for a nerve cell [44].

Nowadays, the modern cell biology covers three main domains of research:

- ➢ **Cytology** which is concerned primarily with cellular structure,
- ➢ **Biochemistry** for understanding of cellular function and
- ➢ **Genetics** which evolved with the realization that DNA (deoxyribonucleic acid) contains all genetic information in most life forms.

The cells are very complex systems (Fig. 2.1). For the present work, the discoveries in cytology are used to understand the biochemical processes, which take place in intracellular and extracellular medium. As will be shown later (chapters 3.7), field effect transistors such as the studied AlGaN/GaN device are able to study the extracellular processes, which take place close of the cell plasma membrane. For this reason the function of the cell membrane will be explain in more detail in the next chapter.

2.1.1. Biomembranes

In 1890s Overton observed that cells are enveloped by some selectively permeable layer, which allowed selectively the passage of some specific substance while blocking others [43]. He found a good correlation between the lipophilic (lipid–loving) nature of the substances and the ease, with which it could penetrate into the cell and he even suggested that such membranes are probably a mixture of *cholesterol* and *lecithins*.
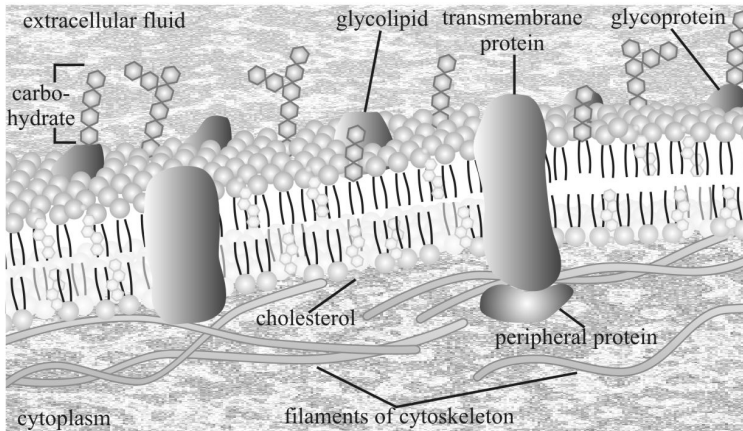

Fig. 2.2: Plasma membrane and its fluid mosaic model [45].

Some years later, Langmuir studied the behavior of lipids by spreading them out as a thin lipid monolayer on a water surface (Langmuir-Blodgett trough). This lipid layer represents the foundation of a cell membrane. It is composed of molecules called phospholipids, which have a backbone derived from a three-hydroxy alcohol called glycerol. Attached to this backbone are fatty acids, long chains of carbon atoms ending in a carboxyl (—COOH) group. Phospholipids have two fatty acid chains attached to its backbone. The third oxygen on the backbone is attached instead to a highly polar aminoalcohol that readily forms hydrogen bonds with water. Because this aminoalcohol (choline) is attached by a phosphate group, the molecule is called a phospholipid. One end of a phospholipid molecule is strongly nonpolar (water-insoluble), and the other end is strongly polar (water-soluble). The two nonpolar fatty acids extend in one direction, roughly parallel to each other, and the polar alcohol group points in the other direction. Because of this structure, phospholipids are often diagrammed as a polar head with two dangling nonpolar tails (as in Fig 2.2.).

When a collection of phospholipid molecules is placed in water, polar water molecules repel long nonpolar tails of phospholipids as water molecules seek partners for hydrogen bonding. Due to the polar nature of water molecules, nonpolar tails of phospholipids end up packed closely together, sequestered as far as possible from water. Every phosphorlipid molecule orients to face its polar head toward water and its nonpolar tails away. When two layers form with tails facing each other, no tails ever come in contact with water. The resulting structure is called a lipid bilayer [45].

The lipid layer function was discovered first time in 1925 by Gorter and Grendel [43]. Lipid bilayers form spontaneously, driven by the tendency of water molecules to form the maximum number of hydrogen bonds. To explain the differential permeability of membranes to solute molecules, Davson and Danielli invoked the presence of proteins as continuous sheets on the membrane surface. In 1972, S. Singer and G. Nicolson improve the Davson-Danielli model in a simple but profound way: they proposed that the globular proteins are inserted into the lipid bilayer, with their nonpolar segments in contact with the nonpolar interior of the bilayer and their polar portions protruding out from the membrane surface. In this model, this is called fluid mosaic model, a mosaic of proteins floats in the quasi-fluid lipid bilayer (Fig. 2.2). Most membranes contain steroid lipids like cholesterol, which can either increase or decrease membrane fluidity, depending on temperature.

In 1975 Henderson and Unwin found out that some proteins have several helical segments that thread their way back and forward through the membrane, forming a channel through the plasma lipid bilayer. For example, bacteriorhodopsin is one of the key transmembrane proteins that carry out photosynthesis in bacteria. The construction and their working function of the transmembrane proteins are very important for the present work and will be discussed in detail in the next.

2.1.2. Transmembrane proteins

Cell membranes represent a barrier to the free movement of solutes into and out of cells and have four components [43-45]:

➢ a lipid bilayers (working as a permeable barrier),
➢ supporting fibers (determine the shape of the cell),
➢ cell surface markers as glycoproteins and glycolipids (cell identity markers), and
➢ transmembrane proteins (major components of every membrane).

The transmembrane proteins that float on or in the lipid bilayer provide transport ways, independent of direct membrane diffusion, for substances and information to cross the membrane. This exchange process, which takes place through the cell membrane, is called membrane transport and can be either passive (does not required energy) or active (require always the input of energy). Passive transport is achieved with channels which create a tunnel as a passage through the membrane (sodium and potassium channels in nerve cells). This diffusion driven transport is a movement of dissolved molecules from higher to lower concentrations. To help larger solutes to cross the membrane barrier, a carrier protein is required in passive transport process. For small nonpolar (hydrophobic) molecules such as O_2 and N_2 as well as small uncharged polar molecules such as urea and ethanol and for water the membrane is permeable. Active transport is catalyzed directly or indirectly by specialized membrane-associated enzymes referred as "pumps". This active process can result in the production of a concentration gradient between inside and outside of the cell. These pump proteins can push ions (electrical charges) such as Na^+, K^+, Ca^+, and H^+ across the membrane and for this reason the resulting concentration gradient can produce an electrical voltage, or membrane potential (Fig. 2.3). The concentration gradient and associated membrane potential is referred to as electrochemical gradient.
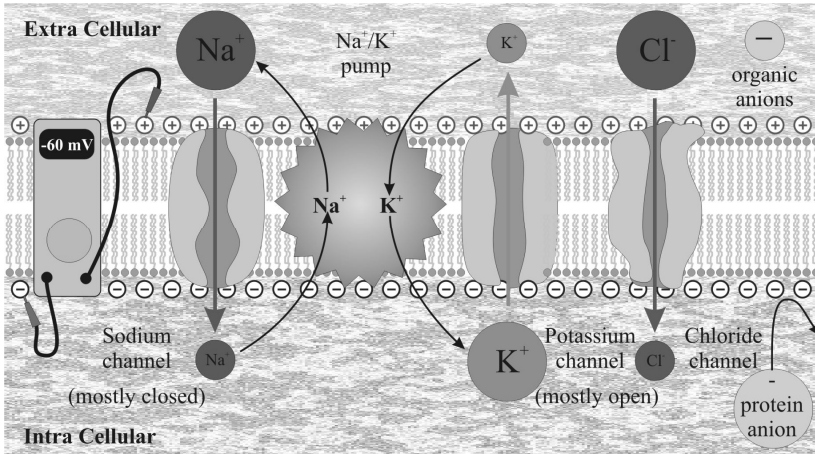
Fig. 2.3: Mechanism of membrane potential [46]

Another component of transmembrane proteins is the receptor, which transmits information into cells. Signal molecules bind to the cell receptor protein and this alters the portion of the receptor protein within the cell, inducing activity. Peptide hormones and neurotransmitters are examples of receptors. The last one will be discussed in more detail later (chapter 2.4).

2.2. Nerve cells and neuron membrane potential

The best study of cellular functions is done in cells that are highly specialized. In the present work an understanding of the function of nerve cell and its transmembrane protein is important for interpreting the result of the recorded extracellular potential on pharmacological manipulation. The nervous system is a characteristic of living vertebrate. The nervous system has three functions [43, 44, 47]:

➢ it collects information from the environment,
➢ it processes that information and
➢ it responds to that information by triggering specific effectors, usually muscle tissue or glands.

To accomplish these functions, a nervous system has special components for sensing and processing information, most important are nerve cells or neurons. Only nerve cells are directly involved in the conduction and transmission of information through the nervous system.
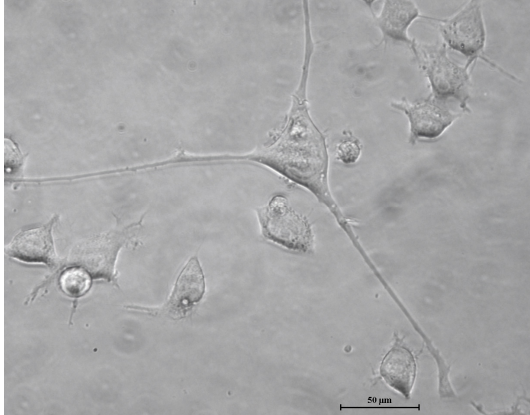
Fig. 2.4: NG 108–15 single nerve cells that were used in this work for transistor - cell coupling and experiments with neuroinhibitors (chapter 7).

The nerves cells are differentiated in sensory neurons (receive and send signals from sensory organs) and motor neurons (stimulate muscle cells to contract or to cause relaxation). The structure of a motor neuron that has been used also in this work (see chapter 7) is shown in Fig. 2.5. The nerve cell contains a cell body that is similar to other cells, with a nucleus and other expected organelles and two types of extensions called processes. One of the processes are called dendrites (receives signals and transmit them inward to the cell body) and other one are called axons (conduct signal away from the cell body). A nerve cell has multiple dendrites and only one axon, which away from the cell body forms multiple branches and terminates in structures called synaptic knobs (nerve terminals). The junction between a neuron to the next or to a muscle and gland cell is called synapse. The transmission of a signal across a synapse can be made directly by electrical connection, but more often it involves certain chemical compounds called neurotransmitters (see chapter 2.4).

For the present work it is essential to understand how nerve signals are generated and how the ion sensitive FET sensors can be used to display the changes of membrane potential. As already discussed, a very important property of almost all cells is the presence of an electrical potential (membrane potential) (Fig. 2.3) across the plasma membrane. In the case of nerve cells, the equilibrium membrane potential (when the cell not transmits a signal) is called resting potential V_m.
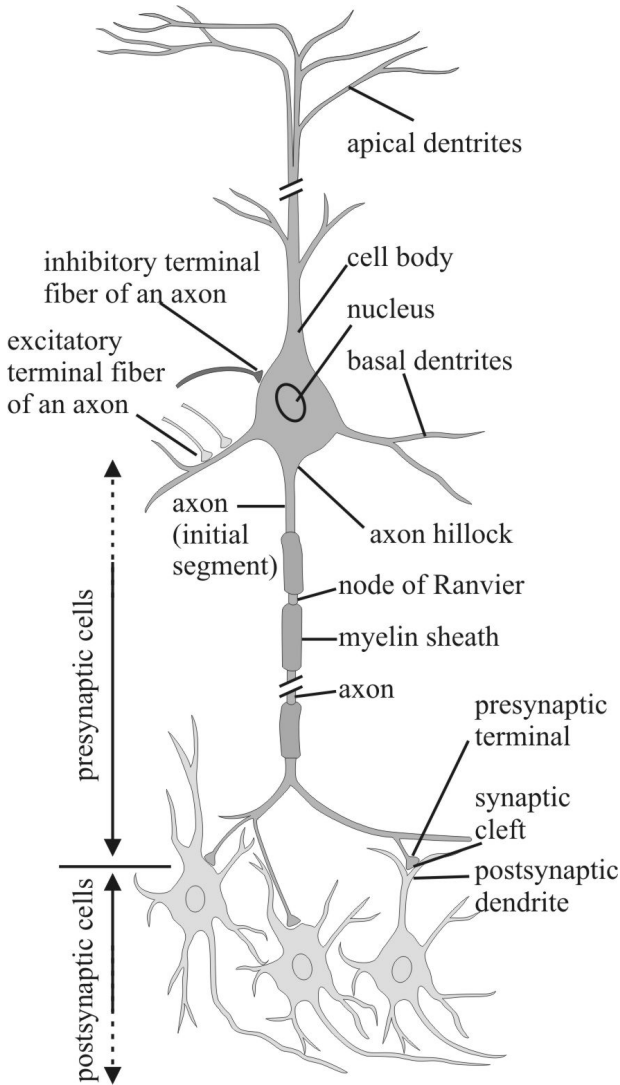
Fig. 2.5: Structure of a typical motor neuron. a) Schematic drawing after Kandel [44].

The nerve cell has also the capacity, called excitability, to change electrical properties of their plasma membranes as response to stimuli. During the reaction time of a membrane to a stimulus, the resting potential undergoes a transient change called the action potential. The action potential transmits an electrical signal along the axon and this represent the unit of information by which cells communicate in the nervous system.

The flow of ions across the lipid membrane is driven by an electrochemical gradient. The gradient is actually a sum of two components, the electronic part which refers to the potential difference across the membrane and a chemical part that refers to the concentration gradient of the ion across the membrane. Because of the concentration gradient between inside and outside of the cell, mainly positively charged ions diffuse down their concentration from higher to lower concentrations, leaving negatively charged ions behind. The separation of positive and negative charge polarizes the membrane and the degree of polarization is measured in millivolts. In this case, two opposite forces act on the positive charged ions: one to be attracted by the negative membrane potential and another one to equilibrate its own concentration gradient. The particular membrane potential that will balance the two competing tendencies for given ionic specie is called the equilibrium potential with respect to that species. This equilibrium potential E_{ion} can be calculated using the Nernst equation as in case of pH determination (see chapter 5.1.2). In case of nerve cells, E_{ion} of a single ion specie is related to the ion concentration C^i_{ion} (inside of the cell), C^o_{ion} (outside of the cell) in mol, the valence n of the ion species and the temperature.

$$E_{ion} = E_{inside} - E_{outside} = \frac{RT}{nF} \ln \frac{C^i_{ion}}{C^o_{ion}}, \qquad (2.1)$$

where T is the absolute temperature in Kelvin, R is the gas constant (8.315 J*K^{-1}*mol^{-1}) and F is Faraday's constant (9.648x10^4 C*mol^{-1}).

In biological systems, Na$^+$, K$^+$, Ca^{2+} and Cl$^-$ ions are responsible for almost all actions. To establish and control their concentration gradient and equilibrium potential is an important step in understanding cell function [43, 44, 47-49]. Typical physiologic values for these ions are given in table 2.1. From the table 2.1 it is possible to see that between intracellular and extracellular compartments, a strong asymmetrical distribution of the ions appears which enables a dynamic state necessary for cell to cell signaling.

Table 2.1: Physiological values of the main ions presents in and out of the cell membrane.

Ion	Mammalian skeletal muscle*				Mammalian neuron**			
	C^i_{ion} [mM]	C^o_{ion} [mM]	ratio ***	E_{ion} [mV]	C^i_{ion} [mM]	C^o_{ion} [mM]	ratio ***	E_{ion} [mV]
Na^+	12	145	12	+67	7	140	20	+80
K^+	155	4	0.026	-98	140	3	0.021	-103
Ca^{2+}	10^{-4}	1,5	15000	+129	10^{-4}	1.5	15000	+129
Cl^-	4.2	123	0.034	-90	7	140	0.05	-80

* after Hille, E_{ion} calculated from equation (2.1) at 37°C [48].

** after Hammond, E_{ion} calculated from equation (2.1) at 37°C [49].

*** ratio of concentration outside/inside for cations and inside/outside for anions [43, 48, 49].

At the resting potential of a membrane, the net flow of charged species across the membrane is zero, because any net flow would result in a change in membrane potential. Even if the net flow of charge is zero the ions still move across the membrane at resting potential. The resting potential of a neuron lies in a range of -30 to -80 mV. This potential is close to the K^+ equilibrium potential, which is about -20 to -70 mV more negative. Therefore, K^+ ions tend to move outward in time. In contrast, Na^+ has a positive equilibrium potential and these ions have the tendency to move inward. Here, the driving force is much greater, since the difference between to the resting potential is about 100-150 mV. According to the Bernstein theory [43], under resting conditions the cell membrane permeability is minimal to Na^+, Ca^{2+} and Cl^- while it is high to K^+. Thus, whenever the membrane potential differs much from the equilibrium potential for K^+, these ions will flow in or out to equilibrate the potential difference. Taking in the account the influence of the three monovalent ions (K^+, Na^+ and Cl^-) that establish the resting potential and by integrating them in Nernst equation, the value of resting potential can be determined by:

$$V_m = \frac{RT}{F} \ln \frac{P_K [K^+]_o + P_{Na}[Na^+]_o + P_{Cl}[Cl^-]_i}{P_K [K^+]_i + P_{Na}[Na^+]_i + P_{Cl}[Cl^-]_o}, \qquad (2.2)$$

where P_K, P_{Na}, and P_{Cl} are the relative permeabilities of the membrane for the respective ions. Because chloride ions have a negative valence, the $[Cl^-]_i$ appears in the numerator.

Relative values of P_K, P_{Na}, and P_{Cl} are 1, 0.04, and 0.45, respectively. Using these values and table 2.1 the membrane potential of a mammalian neuron at room temperature is calculated by:

$$V_m = 58 \log_{10}\left(\frac{1*3 + 0.04*140 + 0.45*7}{1*140 + 0.04*7 + 0.45*140}\right) = -71 \ \text{mV}. \qquad (2.2a)$$

At 37°C the value for RT/F is 61.5 mV and then the membrane potential is V_m = -76 mV. Relation (2.2) is called the Goldman-Hodgkin-Katz equation and was developed and named after these pioneering researchers in neurobiology. When $E_{ion} = V_m$, there is not diffusion of ions through the membrane and when this equality is disturbed, there is a passive diffusion of certain ions through an open channel. The difference V_m - E_{ion} is called the electrochemical gradient and represents the force on the ions to move through the open channel. The electrochemical gradient is responsible for the passive movement of the ions across the membrane. But this passive transport would normally cause concentration changes in the extracellular and intracellular cell compartments if they were not constantly regulated by transport of ions against passive diffusion. This type of transport is described as active because it requires energy in order to oppose the electrochemical gradient of the transported ions. It is realized by pumps, which are special proteins that couple the hydrolysis of ATP (adenosine triphosphate) to active translocations of ions across the membrane. The Na/K – ATPase and Ca – ATPase pumps are responsible to maintain the unequal distribution of Na^+, K^+ and Ca^+ ions across the membrane. In case of Na^+ and K^+ ions, the pump operate continuously at a rhythm of 100 ions per second compared to $10^6 - 10^8$ ions per second for a passive transport through a channel. If the resting potential is highly disturbed, than ionic channels and pumps will react fast to establish again the resting membrane potential and this is known as an action potential.

The permeability changes described above were empirically modeled in 1952 by Hodgkin and Huxley [20]. They predicted the flux of ions across a cellular membrane and resulting changes in the membrane potential. They combine the model with a core conductor theory to predict propagation of an action potential along a cylindrical nerve fiber. Conform to this theory, total membrane current is given by (c_M: specific membrane capacitance):

$$I_{total} = c_M \frac{dV_m}{dt} + I_{ionic}. \qquad (2.3)$$

In every living organism, in every second, a multitude of such processes proceed and their role is to transmit the information from cell to cell in order to keep the system alive and functional. The interaction of the cells and the transmission of the signal in the nervous system is the base of present study and will be the subject of the next chapter.

2.3. Neurotransmitters - acetylcholine

Nerve cells come in contact with each other and also with muscles and glands at junctions called synapses. The synapses can be electrical and chemical transmitters of the signal. The electrical synapses are responsible for transmission with no delay and appear in the nervous system where speed of transmission is of essential importance, for example in the central nerve system.

But most of the synapses are chemical. Chemical synapses depend on specific chemicals called neurotransmitters to conduct the signal across the junction. The neurotransmitter binds to a receptor on the membrane on the second cell and this produces a change in ionic conductance of the receptor or the signal is transmitted to the cytoplasm of the second cell, which is called the second messenger system. Between the membranes of the two cells is a gap of about 20-50 nm, which is called the synaptic cleft.
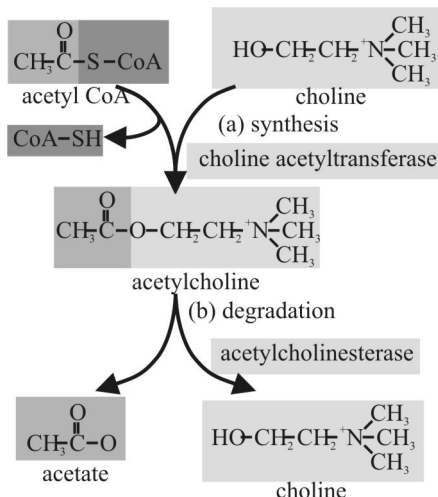

Fig. 2.6: The structure of acetylcholine (ACh), its synthesis from choline and acetyl coenzyme A and its hydrolysis into choline and acetate [43].

Because of this distance, no electrical signal transport is possible (in contrast to the electric synapse). In this case, the nerve signal is transmitted to the postsynaptic membrane by means of a neurotransmitter. One of the most common neurotransmitter for synapses between neurons outside the central nervous system as well as for neuromuscular junction is acetylcholine (ACh) (Fig. 2.6).

The ACh molecules are confined in numerous synaptic vesicles situated near the terminus of the presynaptic axon (Fig. 2.7). The release of the ACh critically depends on Ca^{2+} ions which are present at higher concentrations in the synaptic cleft. The presence of the nerve pulse causes large transient increases in the permeability of the presynaptic membrane to Ca^{2+} ions, thus, Ca^{2+} ions flow down their electrochemical gradient into the axoplasm. In the cell Ca^{2+} ions cause synaptic vesicle to move to the presynaptic membrane and fuse with it. In this mode the ACh is released in less than a millisecond into the synaptic cleft. The ACh molecules diffuse across to the postsynaptic membrane of another cell, where they bind to specific receptor proteins.

Neuroreceptors are always integral membrane proteins with a high degree of specificity for the neurotransmitters. The binding of transmitter causes a conformational change in the receptor that permits increased ionic conductance. When ACh binds to its receptor in the neuromuscular junction, a channel in the receptor opens for about a milliseconds and approximately 30.000 Na^+ ions pass through into the cell and simultaneous the K^+ ions are moving outwards.
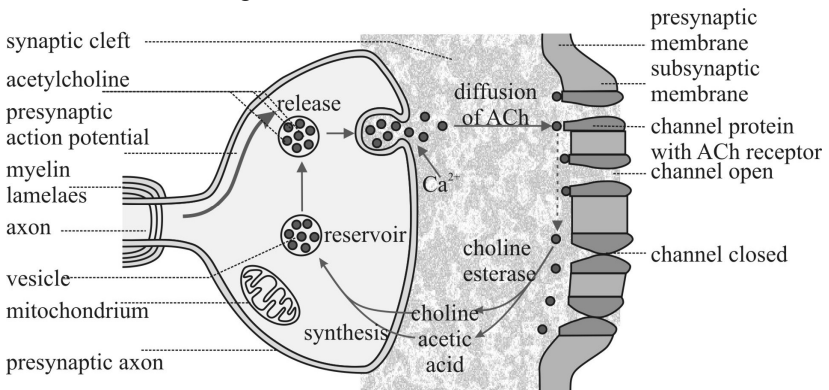

Fig. 2.7: Signal transmission across a cholinergic chemical synapse [50].

This process takes place simultaneously in thousands of receptors at the junction, causing depolarization of the postsynaptic membrane (from $V_m = -60$ mV to $+40$mV) and respective muscle contraction.

An enzyme called acetylcholinesterase (AChE) immediately begins to degrade the ACh into acetate and choline so that the resting potential of the postsynaptic membrane is rapidly restored [43, 44, 47, 51]. The prompt degradation of ACh is absolutely essential. Without the effect of AChE, the ACh would continue its stimulatory effect until the ACh diffuses away, and the control of nervous activity would quickly be lost. For example, the control of the ACh / AChE is an important task in diseases such as Alzheimer and Parkinson [51-53]. There are several organic compounds that act as inhibitor of AChE and therefore, which are potential neurotoxins. Such compounds are synthesized for use in pharmacological screening [53], as insecticides [54] in agriculture and as nerve gases for chemical warfare. The effect of such kind of neurotoxins on nerve cells will be studied in this work using AlGaN/GaN FET (see chapter 7).

Table 2.2: Small molecules transmitter substances and their key biosynthetic enzymes [44]

Transmitter	Enzymes	Activity
acetylcholine	choline acetyltransferase	specific
biogenic amines		
dopamine	tyrosine hydroxylase	specific
norepinephrine	tyrosine hydroxylase and dopamine β-hydroxylase	specific
epinephrine	tyrosine hydroxylase and dopamine β-hydroxylase	specific
serotonin	tryptophan hydroxylase	specific
histamine	histidine decarboxylase	specificity unknown
amino acids		
Γ-aminobutyric acid	glutamic acid decarboxylase	probably specific
glycine	enzymes operating in general metabolism	specific pathway undetermined
glutamate	enzymes operating in general metabolism	specific pathway undetermined

There are further compounds known to act as neurotransmitters. Several criteria must be satisfied to qualify a compound as neuro-transmitters:

➢ it must elicit the appropriate response when microinjected into the synaptic cleft,
➢ it must occur naturally in the presynaptic axon, and
➢ it must be released at the right time when the presynaptic membrane is stimulated [43, 44, 51].

Compounds that satisfy these criteria are listed in the table 2.2. There are also neurotransmitters which act not to excite the postsynaptic cell, but to inhibit it. In the nervous system function, the inhibition plays the same important role as excitation. The neuroinhibitors, which are used in this work, are discussed in the next chapter.

2.4. Neuroinhibitors

The good functioning of the human body critically depends on its nervous system and anything that disturbs it is considered to be very toxic. As explained before, ACh is one of the most important neurotransmitters and any substance that disrupts its function can be lethal for the human organism. Researchers have found a lot of substance that disrupt nerve and muscle function by specific effects on cholinergic synapses. In the present chapter we will consider some of these neurotoxins and try to explain their action in order to understand the importance of such compounds as effective research tools in studying the disruption phenomena.

Once ACh has been released into the synaptic cleft and depolarization of the postsynaptic membrane has occurred, the excess ACh must be rapidly hydrolyzed. Without this process the membrane cannot be restored to its polarized state and further transmission will not be possible. The responsible enzyme for hydrolysis is AChE and every substance that inhibits the AChE activity is potentially toxic.

Carbamoyl esters represent such family of AChE inhibitors. The inhibition of AChE is realized - in the case of carbamates - by reversible blocking the active site of the enzyme, thus, effectively preventing the breakdown of ACh. To this family is included the physostigmine (eserine), a naturally occurring alkaloid produced by the Calabar bean.

There are also many synthetic organic phosphates, which are more potent inhibitors because they form very stable covalent complexes with the active site of AChE. Such compounds are for example the insecticides Parathion and Malathion [54], as well as nerve gases such as Tabun and Sarin. The effect of these compounds is muscle paralysis, caused by an inability of the postsynaptic membrane to recover its polarized state.

An irreversible, potent AChE inhibitor is also diisopropyl-fluorophosphate (DFP). It has a lethal dose LD50 for rats of 4 mg/kg. It is a structural analogy to Sarin, is an oily, colorless or faint yellow liquid with the chemical formula $C_6H_{14}FO_3P$. It is used in medicine and as an organophosphate insecticide. It is stable, but undergoes hydrolysis when subjected to moisture, producing hydrofluoric acid [55].

The high toxicity of esters of monofluorophosphoric acid was discovered in 1932, when Willy Lange and his PhD student Gerda von Krueger prepared the methyl, ethyl, n-propyl, and n-butyl esters and incidentally experienced their toxic effects. The homologue of this series of esters, DFP, was developed by British scientist Bernard Charles Saunders. It combines with the amino acid serine at the active site of the enzyme AChE (Fig. 2.8).
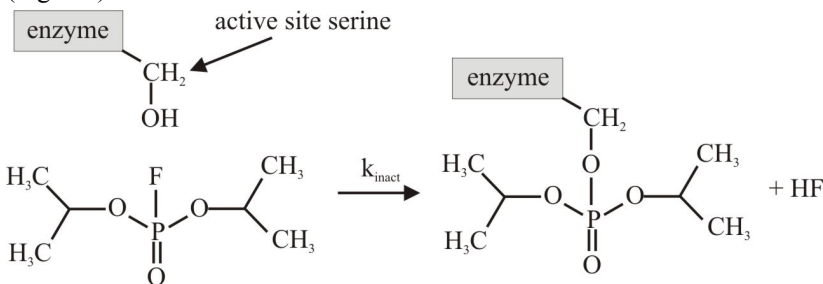

Fig. 2.8: Reaction of the irreversible inhibitor diisopropylfluorophosphate (DFP) with a serine protease.

Phenylmethanesulphonylfluoride (PMSF) with the molecular formula $C_7H_7FO_2S$ (Fig. 2.9) is a serine protease inhibitor, which acts weaker than DFP. PMSF is rapidly degraded in water and stock solutions are usually made up in anhydrous ethanol, isopropanol, corn oil or dimethyl sulfoxide (DMSO). Proteolytic inhibition occurs when a concentration between 0.1 and 1 mM PMSF is used. The half-life time is small in aqueous solutions.

The LD50 is about 500 mg/kg. Both DFP and PMSF are used successfully to inhibit the AChE in this work (see chapter 7).

Nerve transmission at cholinergic synapses can be blocked not only by inhibitors of AChE, but also by substances that compete with ACh for binding to its receptor on the postsynaptic membrane. An example of such a neurotoxin is curare, a plant extract used by Indians to poison arrows. The active factor in curare is d-tubocurarine. α-bungarotoxin and cobratoxin snake venoms are small, basic proteins that bind noncovalently to the ACh receptor and in this mode block the depolarization of the postsynaptic membrane. These kind of neurotoxins described above are called antagonists of cholinergic systems and other compounds are referred as agonists and have just the opposite effect. Agonists also bind to the ACh receptor, but doing so they mimic ACh, causing depolarization of the postsynaptic membrane. The exception is that they cannot be rapidly inactivated, so the membrane can not recover its polarized state.

Other kinds of neurotoxins are the one which are designed to block the ion channels. The tetrodotoxin is a lethal toxin from the Pufferfish and saxitoxin from the Gonyaulax that partially enter and block the voltage sensitive Na^+ channel. Similarly, dendrotoxin from the Black Mamba snake inhibits the voltage sensitive K^+ channel. Such inhibitors of ion channels have important research potential by allowing scientists to "turn off" specific channels and in this mode to understand the other channels contributions to the operation of cells or in assaying their concentration.
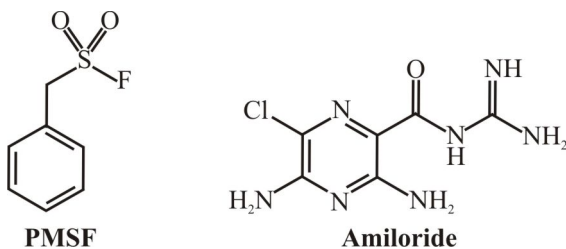
Fig. 2.9: Chemical formulas of the Phenylmethanesulphonylfluoride (PMSF) and Amiloride used in the present work as neuroinhibitors.

A synthetic and reversible channel blocker, which is also used in this work, is amiloride (Fig. 2.9), $C_6H_8ClN_7O$.

It works by direct blocking the epithelial sodium channel (ENaC) thereby inhibiting Na^+ reabsorption in the distal convoluted tubules and collecting ducts in the kidneys (this mechanism is the same for triamterene). This promotes the loss of Na^+ and water from the body, without depleting K^+. The compound is soluble in hot water (50 mg/ml), yielding a clear, yellow-green solution.

Amiloride is freely soluble in DMSO, slightly soluble in isopropanol and ethanol, practically insoluble in acetone, chloroform, diethyl ether, and ethyl acetate. The amiloride was used in this work together with PMSF and DFP inhibitors to study the combined reaction of nerve cells and to identify the ions which contribute to the sensor signal.

Consequently, all processes and cell reactions result in a change of specific ion fluxes across the cell membrane. The goal of this work is to establish a measurement technique for the changes in ion concentrations outside the cell as a reaction to neuroinhibitors, i.e. of the cell action potential, by a planar sensor, where the nerve cells are cultivated on. These sensors will be the AlGaN/GaN field effect transistors. In the next chapters the basic background of these sensors regarding the specific materials properties, the transistor function and its reaction in electrolyte will be discussed in more detail before coming to the description of the cell-transistor coupling experiments and the monitoring of the cell response to neurotoxins in chapters 6 and 7.

3. Group III Nitrides: from material to device

3.1. Basic properties of group III nitrides

The first report about Gallium Nitride (GaN) appeared in 1938 by Juza and Hahn [56]. They synthesized it by passing ammonia over hot gallium. Using crystals grown by the same technique, photoluminescence spectra were presented in 1959 [57]. Ten years later, the first growth of GaN by chemical vapor deposition (CVD) was demonstrated by Maruska and Tietjen [58]. Further techniques developed in the 60s were Ga_2O_3 / NH_3 reaction [59] and evaporation of Ga in nitrogen plasma [60]. All these GaN materials were n-type and the donors were believed to be caused by nitrogen vacancies. Due to the high density of structural defects and the impossibility for p-doping, the material was not used to fabricate electronic devices until the late 80s. After 1983, the establishment of metal-organic chemical vapor deposition (MOCVD) [61] and molecular beam epitaxy (MBE) [62, 63] gave the possibility to grow GaN with improved structural and electrical properties. The very first GaN based violet light emitting diode was demonstrated as early as 1972 [64]; an effective p–doping, however, was not demonstrated until the proposal of a post growth low energy electron beam irradiation of GaN:Mg by Amano and Akasaki [65]. A more technical process was the annealing of GaN:Mg films at 750°C in N_2 reported by Nakamura in 1992 [66]. This discovery led to an explosion in GaN research and soon commercialization of optoelectronic devices started. Furthermore, outstanding electronic properties of GaN promote its use for high temperature, high power and high frequency electronics, which caused a second field of commercial GaN applications. After 2000, unique properties of group III nitrides attracted increasing interest for mechanical and sensing applications. First developments and basic principles were summarized in the early reviews of Ambacher and Pearton [67, 68].

The group III nitrides are direct semiconductors and the band gap energy spans a wide range from 0.7 eV for InN (Indium Nitride) [69], to 3.4 eV for GaN and 6.2 eV for AlN (aluminum nitride) [70] for wurtzite semiconductors. In addition to the binary compounds, group III nitride material can form also ternary (AlGaN, InAlN, InGaN) and quaternary (InAlGaN) alloys, which opens wide possibilities for band gap-engineering in the spectral range from near infrared to deep ultraviolet (UV).

As a result, green, blue and UV light emitters, laser diodes [67, 68] and UV detectors [71-74] were developed. Furthermore, high electron mobility transistors (HEMT) for high power and high frequency applications based on AlGaN/GaN heterostructures have been intensely investigated since the early 90s and are on the verge of commercialization [75]. Profiting from the research on HEMT devices and utilizing the basic HEMT structure, chemical sensors for gases and liquids were developed which received increased attention in the last five years, see the reviews of Eickhoff [39] and Pearton [40]. Due to their wide band gaps and strong bond strengths, this material system has a very good chemical stability as seen in their resistance to wet etching procedures [68, 76], and their biocompatibility [77, 78]. In combination with low noise due to the wide band gap [19] and high sensitivity to changes of the surface charge [38], group III-nitrides are considered to be one of the most promising materials for biosensor devices [79]. Moreover, the transparency in the visible range of light opens up the possibility to combine standard optical and electrical measurements. With respect to the construction of integrated devices, the monolithic integration of chemical sensors with group III nitride optoelectronics for combined spectroscopic analysis, transistors for on-chip signal processing, and surface acoustic wave devices [80] for analogue signal filtering are possible. Wireless sensor networks using radio frequency identification (RFID) have also been suggested [40].

The following chapter gives a short introduction to the main properties of group III nitride semiconductors and the formation of a two dimensional electron gas (2DEG) in an AlGaN/GaN heterostructure.

3.1.1. Crystal structure

Group III nitrides can crystallize in wurtzite, zincblende or rocksalt structures [81]. In practical devices, mainly the wurtzite polytype is used, because it is thermodynamically the most stable one at room temperature. The wurtzite structure consists of alternating biatomic close-packed (0001) planes of Ga and N pairs stacked in an ABABA sequence (Fig. 3.1). Atoms in the first and the third layers are aligned with each other. This crystal structure is characterized by the edge length a of the basal hexagon, the height c of the hexagonal prism and an internal parameter u defined as the anion (Ga) − cation (N) bond length along the (0001) axis. The cell parameter $u = \sqrt{c/a}$ is a non-linear function of alloy composition [82, 83].
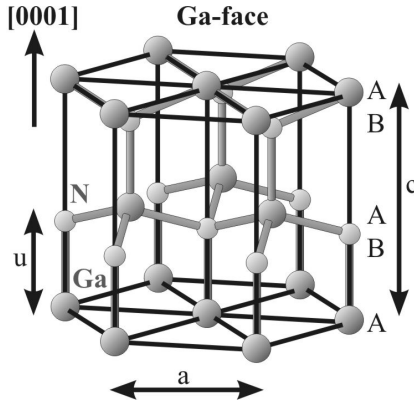
Fig. 3.1: Schematic representation of GaN wurtzite structure with Ga-face polarization.

InN, GaN and AlN have different lattice constants, band gaps and binding energies because of the different cations and ionic radii as shown in Table 3.1 on the example of AlN, GaN and AlGaN alloys, which currently are the most important materials for sensing applications.

The polarity of the crystal is an important property of group III nitrides, especially GaN since for the developed sensors it is always the basis material to start growing heterostructures. The common growth direction of hexagonal GaN is normal to the basal plane, where the atoms are arranged in the bilayers consisting of two closely spaced hexagonal layers, one with cations and the other with anions, so the bilayers have polar faces. This means that the crystal structure is non-centrosymmetric, the sequences of atomic layering parallel to the crystallographic planes is different as is illustrated in Fig. 3.1. The [0001] direction which usually is given by a vector pointing from Ga atom to a nearest neighbor N atom is known as the Ga face (Ga on top position of the (0001) bilayer) and the inverse [000$\bar{1}$] is known as the nitrogen faces. The polarity is a bulk property and not a surface property while a Ga face material can be Ga terminated or N terminated as well. The chemical properties of the material are very different depending on the polarity and the termination of the material [86]. The polarity of the crystal also determines the direction of the polarization vector, which determines the sign of the charge found at a hetero-interface.

The polarity of the crystal can be determined experimentally using convergent beam electron diffraction [87], photoelectron spectroscopy [88] or Auger electron spectroscopy (AES) [89] as well as by studying the etching behavior of the crystals using KOH or NaOH [90]. Usually, Ga face material is smoother than N face material, is harder to etch and AlGaN/GaN transistors with high mobility two dimensional electron gases (2DEG) are commonly formed on Ga face material. The Ga-face polarity is achieved by MBE or MOCVD growth on c-plane sapphire substrates using a thin AlN nucleation layer [91]. Both methods were used for the development of biosensors with an AlGaN/GaN heterostructure (Fig. 3.2).

3.1.2. Spontaneous and piezoelectric polarization

The spontaneous and piezoelectric polarization in group III nitrides was first predicted and calculated by Bernardini and Florentini [82] and the values are given in table 3.1.

Table 3.1: Material parameters for AlN, GaN and AlGaN as function of Al concentration x. (a) and (b) correspond to theoretical and experimental values, respectively. All the data are from references [82-85].

	AlN	GaN	$Al_xGa_{1-x}N$
Lattice constant a [Å]	3.112	3.189	$3.189-0.077x$
Lattice constant c [Å]	4.982	5.185	$5.185-0.232x$
Cell parameter u	0.382	0.377	$0.382x + 0.377(1-x) - 0.0032x(1-x)$
Energy gap E_g (300K) [eV]	6.28	3.42	$6.28x + 3.42(1-x) - 1.00x(1-x)$
Dielectric constant ε_r	9	9.5	$-0.5x+9.5$
Elastic constant C_{13} [GPa]	108(a) 120(b)	103(a) 70(b)	$5x+103$
Elastic constant C_{33} [GPa]	373(a) 395(b)	405(a) 379(b)	$-32x+405$
Piezoelectric constant e_{31} [C/m²]	-0.60	-0.49	$-0.11x-0.49$
Piezoelectric constant e_{33} [C/m²]	1.46	0.73	$0.73x+0.73$
Spontaneous polarization P_{SP} [C/m²]	-0.090	-0.034	$-0.090x - 0.034(1-x) + 0.021x(1-x)$

x – Al concentration

The *spontaneous polarization* is the polarization at zero strain and is a bulk effect due to the non-centrosymmetric crystal structure and the ionic character of the metal-nitrogen bond. It is very large in the group III nitrides. The spontaneous polarization is described by a vector P_{SP} (table 3.1.) with a fixed orientation in the crystal. It can appear only in the crystals (known as pyroelectric crystals) that satisfy the Neumann's principle: "The symmetry elements of any physical property of a crystal must include the symmetry elements of the point group of the crystal". The non-centrosymmetric wurtzite structure, with its six symmetry axis and mirror planes containing it (Fig. 3.1), satisfies this principle and can therefore have a spontaneous polarization which is parallel to the polar c-axis [0001]. The sign of the spontaneous polarization is determined by the polarity and is opposite to the direction [0001]. Similar to the band gap [92], also the spontaneous polarization vector of AlGaN depends nonlinearly on the Al mole fraction [93] (table 3.1). AlN has significantly stronger polarization than GaN and an alloy of the two, i.e., AlGaN should have stronger polarization than GaN as well. Therefore the polarization vectors in Ga-face material points from the surface into the bulk.

The spontaneous polarization can be altered by additionally induced polarization such as the piezoelectric polarization caused by mechanical strain. The piezoelectric polarization is calculated by [84]:

$$P_{PE} = e_{33}\varepsilon_z + e_{31}\left(\varepsilon_x + \varepsilon_y\right), \tag{3.1}$$

where $\varepsilon_z = (c - c_0)/c_0$ is the strain along the c axis, $\varepsilon_x = \varepsilon_y = (a - a_0)/a_0$ is the in-plane strain that is assumed to be isotropic, e_{33} and e_{31} are piezoelectric coefficients (table 3.1) and a_0, c_0 are the equilibrium values of the lattice parameters. In the case of biaxial stress, which is the typical case for epitaxial layers, the relation between the lattice constants in wurtzite materials is given by

$$\frac{c - c_0}{c_0} = -2\frac{C_{13}}{C_{33}}\frac{a - a_0}{a_0}, \tag{3.2}$$

where C_{13} and C_{33} are elastic constants (table 3.1). Using the equations (3.1) and (3.2), the piezoelectric polarization in the direction of the c-axis is

$$P_{PE} = 2\frac{a - a_0}{a_0}\left(e_{31} - e_{33}\frac{C_{31}}{C_{33}}\right). \tag{3.3}$$

3.1.3. AlGaN/GaN heterostructure

For the biosensors in this work, a heterostructure is grown in c-axis direction. A heterostructure is a combination of at least two different semiconductors, in this case with an AlN nucleation layer, a thick GaN buffer layer and a tensile strained $Al_xGa_{1-x}N$ barrier layer on top. AlN, AlGaN and GaN exhibit different lattice constants (table 3.1). This mismatch results in defect generation at the heterointerfaces. In the case of GaN on the AlN nucleation layer, the density of these defects can be reduced by growing thicker GaN buffer layers, where partial annihilation of the defects occurs [67, 94]. Similar defects to accommodate the lattice mismatch are generated if thick layers of AlGaN are grown on top of GaN. However, if the AlGaN on top of GaN is very thin (up to ~30 nm) AlGaN can grow pseudomorph with the in plane lattice constant *a* of GaN. Therefore the AlGaN barrier has biaxial tensile strain.

This tensile strain induces a piezoelectric polarization in the AlGaN barrier, which adds to the spontaneous polarization of the heterostructure [84]. Since $\left(e_{31} - e_{33} \dfrac{C_{31}}{C_{33}} \right)$ is below zero, for AlGaN the piezoelectric polarization is negative for tensile and positive for compressive strained AlGaN barriers. Thus, for the present tensile strain, the orientation of the piezoelectric polarization is parallel to the spontaneous polarization (Fig. 3.2) and would be antiparallel for compressively strained AlGaN layers.
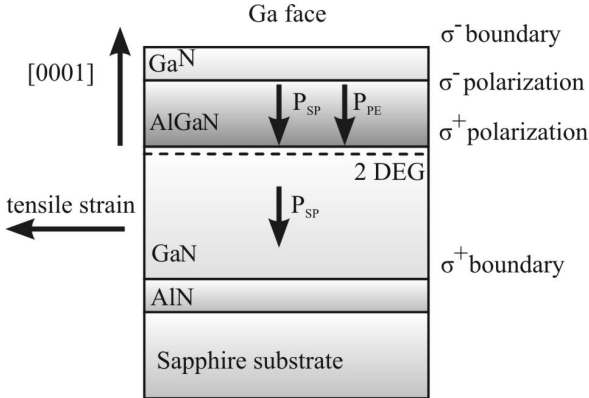

Fig. 3.2: Spontaneous and piezoelectric polarization bound interfaces charges and 2DEG in an AlGaN/GaN heterostructure with Ga-face polarity.

It has been shown that in the investigated heterostructures the total polarization of the strained AlGaN barrier is larger than that of GaN buffer and therefore a polarization gradient at the AlGaN/GaN interface is present. This results effectively in a positive polarization charge (Fig. 3.2). Electrons from bulk GaN material tend to compensate this positive polarization charge leading to the formation of a two dimensional electron gas (2DEG). The spontaneous and piezoelectric polarization in the investigated AlGaN/GaN heterostructure is sufficiently large to accumulate 2DEGs with high sheet carrier concentration ($n_s \geq 10^{13}$ cm^{-2}) and mobility ($\mu = 2000$ cm²/Vs) even without intentional doping of the barrier [36]. The sheet carrier concentration n_s can be calculated using equation 3.4 and depend on Al content x of the barrier and its thickness d [84].

$$n_S(x) = \frac{+\sigma(x)}{e} - \left(\frac{\varepsilon_0 \varepsilon(x)}{de^2}\right)[e\phi_b(x) + E_F(x) - \Delta E_C(x)], \qquad (3.4)$$

where ε_0 and $\varepsilon(x)$ are the dielectric constants (see table 3.1), $e\phi_b(x)$ is the Schottky-barrier on the active surface, $E_F(x)$ is the Fermi level and ΔE_C is the conduction band offset at the Al$_x$Ga$_{1-x}$N/GaN interface. Using this equation it was possible to simulate the formation of 2DEG with different sheet carrier concentration (see chapter 3.2).

Obviously AlGaN/GaN HEMTs contain high sheet carrier concentrations in the 2DEG even in absence of doping. The sources of these electrons are supposed to be the surface states at the AlGaN surface [95, 96]. Other possible sources for the mobile carrier are unintentional dopants, interfaces states and deep level defects. All of these possible sources of carrier may contribute in different proportion to the 2DEG in an actual device. In the Fig. 3.3, a schematic conduction band diagram for an AlGaN/GaN heterostructure is shown.

As described in the model of Ibbetson *et al*. [95], the structure contains different space charge components. The concentration of surface states on AlGaN/GaN is difficult to estimate. For an undoped barrier, the number of 2DEG electrons are due to ionized donors in the AlGaN plus (minus) the number of ionized donor (acceptor) – like states on the surface. If for an undoped barrier, the surface states are considered to be donor-like (neutral when occupied, positive when empty) with a corresponding energy E_D to be below the conduction band, it is possible to approximate the occupancy of this states and thus its energy relative to the Fermi level E_F.
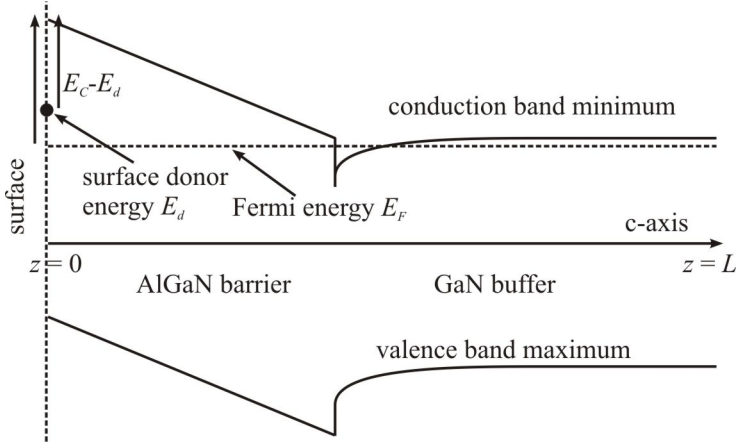
Fig. 3.3: Electronic band scheme of an AlGaN/GaN HEMT device perpendicular to the surface. The conductive channel is formed by a 2DEG. E_C is the conduction band minimum, E_V the valence band maximum, E_F the Fermi level [95].

States, which are sufficiently deep in the band gap, have an energy E_D below E_F. These states are filled with electrons and are neutral. As the barrier becomes thicker, the polarization field increases the surface potential. At a critical thickness the donor energy E_D reaches the Fermi level and electrons can be transferred from occupied surface states to empty conduction band states of GaN close to the interface. In this mode electron are confined in the triangular potential well at the AlGaN/GaN interface and the 2DEG as well as the positive surface charge is created. As the AlGaN layer becomes thicker, more and more electrons move to the channel until the channel charge density saturates at a certain AlGaN thickness.

The 2DEG density was calculated and simulated as function of barrier thickness, AlGaN mole fraction, and GaN cap layer thickness [70, 95, 96]. Such simulations will be shown later in chapter 4 in context with the experimental results. All simulations performed until now shows that the surface traps are the main source of the channel electrons, and the polarization induced electric field is the driving force to move the trapped electrons to the AlGaN/GaN interface to form a 2DEG.

3.2. AlGaN field effect sensors

In a conventional high electron mobility transistor, the 2DEG forms the channel between the two Ohmic contacts drain (D) and source (S) and is modulated by a top gate. On an uncovered gate, the surface potential and thus, the 2DEG density is affected by presence of charge species from the environment. Although the strong response on charges was first termed as a parasitic effect, which had to be controlled for the optimization of HEMTs, the potential for sensor applications was demonstrated shortly afterwards and represents the basic idea to realize ion sensitive field effect transistors (ISFETs). Its function and the particularities for AlGaN/GaN FETs and for the operation in electrolytes, which are essential for biosensors, will be described in the following chapter.

3.2.1. AlGaN/GaN ion sensitive FETs

Since the proposal of a pH sensitive device, based on the technology of field effect transistors by Bergveld in 1970 [33], a large number of publications has appeared devoted to ISFETs. A historical overview, which also highlights future challenges and possibilities, is given by Bergveld [34]. Despite high prospects and promising demonstrations of these devices, the fact that they are based on silicon technology, while being beneficial for mass production, impairs their long-term chemical stability and thus limits the areas of application [97].

In contrast to conventional ISFETs, the AlGaN/GaN heterostructure utilizes the piezoelectric and spontaneous polarization properties of the material system. As a consequence, the AlGaN/GaN heterostructure exhibits a captivating simplicity in its structure without the need for additional passivation films or elaborate designs while retaining or exceeding the sensitivity, noise characteristics, and chemical and thermal stability of Si-based ISFETs.

The modulation of the 2DEG charge density by electric fields was exploited for the construction of chemical sensor devices. Leaving a bare GaN surface by omitting the gate metallization, a modulation of the channel current I_D by external ions was first observed by Neuberger *et al.* [38]. Ions were generated by a plasma spray device and directed to the surface. The change in the surface charge by the incident ions affected directly the 2DEG density (Fig. 3.4).
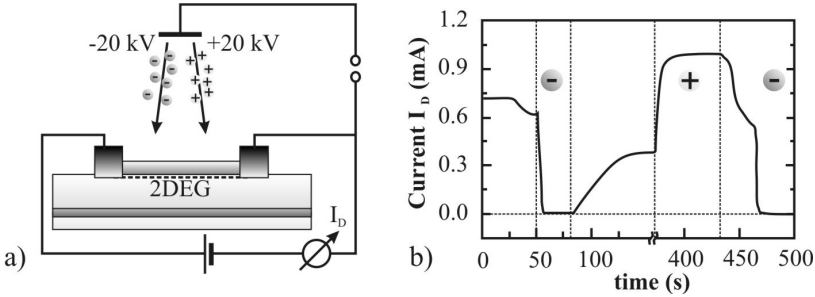
Fig. 3.4: (a) Schematic setup for the detection of positive and negative ions from a plasma spray technique using an AlGaN/GaN heterostructure. (b) Depletion and enhancement of the 2DEG due to incident ions reflected in the change of the drain current [98].

A negative ion flux of about 10^{13} cm^{-2}s^{-1} depleted the 2DEG with a sheet carrier concentration of $1.2*10^{13}$ cm^{-2} and a response time of approximately 1 s, indicating that every incident negative ion displaces one electron from the 2DEG. As cyclic changes were found to be completely reversible [98], irreversible processes like trap formation or surface oxidation could be ruled out.

Applying water as well as different organic solvents to the surface of the same structure illustrated that on the one hand I_D is influenced by the dipole moment of the liquid (Fig. 3.5b) with acetone leading to the greatest current reduction. On the other hand, it was noted that the molecule size yielded different results for similar dipole moments [99]. This and the unordered dipole orientation in liquids impair quantitative determination of dipole moment but allows for qualitative evaluation of polar contaminations in nonpolar liquids (e.g. hydraulic oil, Fig. 3.5c). Similar results were later reported for the exposure of similar heterostructures to organic solvents [100, 101] and polymer solutions [102]. Acetone and ethanol significantly reduce I_D relative to the value in air and water. Polar polymers also cause the channel current to decrease. The smaller dipole moment of polystyrene (PS: 0.123 D) [103], however, induced a larger reduction than polyethylene oxide (PEO: 1.89 D) which was not consistently explained by Kang *et al.* [102], but is likely to be due to a 10 times higher concentration of PS compared to PEO. Also for the block copolymer PS-PEO a decreasing I_D was demonstrated for increasing concentrations.
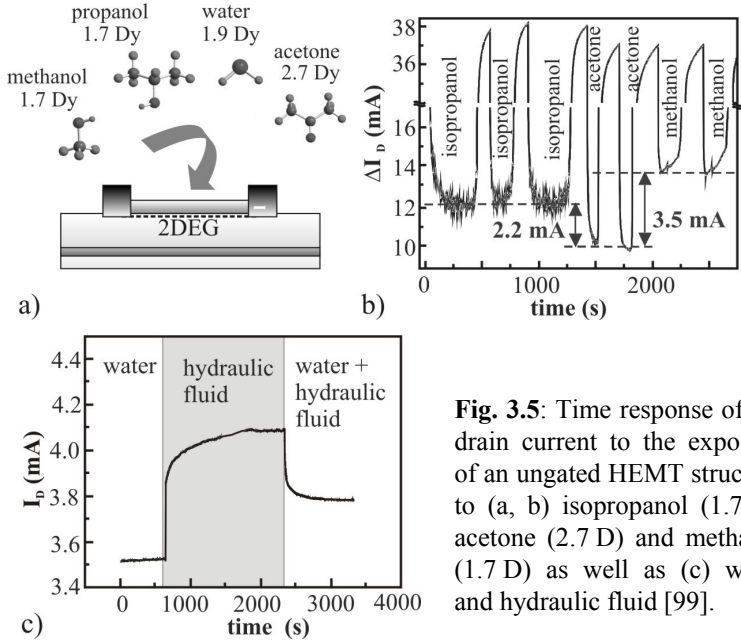
propanol
1.7 Dy

water
1.9 Dy

acetone
2.7 Dy

methanol
1.7 Dy

2DEG

a)

b)

c)

Fig. 3.5: Time response of the drain current to the exposure of an ungated HEMT structure to (a, b) isopropanol (1.7 D), acetone (2.7 D) and methanol (1.7 D) as well as (c) water and hydraulic fluid [99].

3.2.2. AlGaN/GaN electrolyte gate FET

In AlGaN/GaN electrolyte gate FETs (EGFETs) as special case of ISFETs, the open gate area is directly exposed to an electrolyte, whose concentration of certain ions has to be determined. This EGFET is the basic element of all AlGaN/GaN based biosensors. Instead of fixed gate voltage, a reference potential U_{ref} is applied to the electrolyte–oxide–semiconductor system via a reference electrode (see chapter 3.2.3), which is dipped into the electrolyte [104] (Fig. 3.6). A positive drain voltage U_{DS} drives a drain current I_D parallel to the AlGaN/GaN interface. Transistor action is possible since an additionally applied reference voltage U_{ref} shifts the Fermi level with respect to the conduction band of the undoped GaN layer. Due to charges on the open gate surface (donors in the AlGaN layer are not occupied), most of the voltage drop is across this AlGaN layer, thus establishing a quasi-insulating barrier between the open gate and the 2DEG. The barrier has a similar function as SiO_2 layers in a Si-MOSFET.
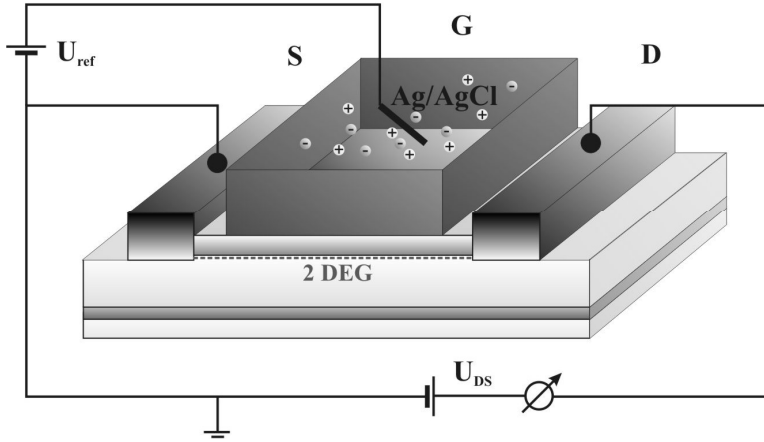
Fig. 3.6: Schematic view of an AlGaN/GaN EGFET. The metal gate is replaced by an electrolyte contacted with an Ag/AgCl reference electrode.

Depending on the reference voltage, the triangular potential well at the interface is raised or lowered in energy and the channel is emptied or filled. This corresponds to alteration of the drain-source current. For large enough reference bias, 2DEG region completely depletes, and the current channel is pinched off. The corresponding relative reference voltage is called threshold voltage U_T. For AlGaN/GaN devices the common equation for FETs describes the drain current in the non-saturated region (below pinch-off):

$$I_D = \beta \cdot \left(U_{ref} - U_T - \frac{1}{2}U_{DS} \right) \cdot U_{DS}, \tag{3.5}$$

where β is a parameter depending on the geometry (the channel width to length ratio W/L), the mobility μ of the electrons in the 2DEG and the gate insulator capacitance per unit area C_{ox}:

$$U_T = E_{ref} - \Psi_o + X_{sol} - \frac{\phi_{AlGaN}}{e} - \frac{Q_{SS} + Q_{ox} + Q_B}{C_{ox}} + 2\Phi_F. \tag{3.6}$$

In case of an ISFET, the gate voltage is the voltage at the reference electrode $U_{ref} = U_{GS}$. The threshold voltage contains also terms which reflect the interfaces between the liquid and the gate oxide on the one side and the liquid and the reference electrode at the other side.

52

The work function of the gate metal in a conventional MOSFET is here replaced by the reference electrode potential relative to vacuum E_{ref} for the ISFET The vacuum level can be calculated with the electrode potential relative to the normal hydrogen electrode (NHE) plus the value of the Fermi level relative to the vacuum states (U_{NHE} = 4.7 V [105]). For the widely used Ag/AgCl electrode, a value of U_{ref} = 4.9 V is calculated. The interface potential at the gate oxide-electrolyte interface is determined by the surface dipole potential of the solution χ_{sol}, which is a constant, and the surface potential ψ_0, which results from a chemical reaction, usually governed by the dissociation of oxide surface groups. In this case the threshold voltage is given by:

$$U_T = E_{ref} - \Psi_o + X_{sol} - \frac{\phi_{AlGaN}}{e} - \frac{Q_{SS} + Q_{ox} + Q_B}{C_{ox}} + 2\Phi_F, \tag{3.7}$$

where Q_B is the depletion charge in the AlGaN, Φ_F the Fermi-potential, ϕ_{AlGaN} the material work function, Q_{SS} the charges in surface states at the GaN surface and Q_{ox} the fixed oxide charge.

All terms are constant except ψ_o, which causes the sensitivity of an ISFET to the electrolyte pH, as the controlling parameter for the dissociation reactions of the oxide surface groups. The influence of the ion concentration on ψ_o can be explained by applying the Site-Binding model (in the case of pH – sensitivity), which was introduced by Yates *et al*. in 1983 [106]. It proposes that atoms in the surface layer of metal- as well as semiconductor oxides are acting as amphoteres, when they are in contact with an electrolyte. Thus, depending on the H^+ (OH^-) concentration in the electrolyte, they can release protons into the electrolyte (acting as donor) and thus, are negatively charged, form neutral OH sites or bind protons from the electrolyte (acceptor), resulting in a positive surface charge.

donor: $M–OH \leftrightarrow M–O^- + H^+$ (3.8a)

acceptor: $M–OH + H^+ \leftrightarrow M\text{-}OH_2^+$ (3.8b)
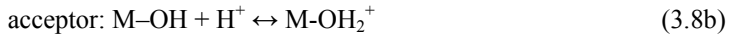
These surface reactions depend on the acidity and the alkalinity constant of the oxide groups, as well as the concentration of H^+ in the electrolyte. In the case of a high concentration of H^+ (low pH), the M-OH groups are rather tending to accept a proton, instead of releasing one, and thus most of them are acting as acceptors, and the oxide surface becomes positively charged.

In contrast, if the concentration of H^+ is low (high pH), most of the M-OH groups release a proton, and the surface charge becomes negative. To determine the total change in surface charge, the sum over all surface sites N_s has to be considered, which depends on the material (e.g. $N_s(SiO_2) \sim 5 \cdot 10^{14}$ cm^{-2}, $N_s(Al_2O_3) \sim 8 \cdot 10^{14}$ cm^{-2}, $N_s(Ga_xO_y) \sim 9 \cdot 10^{14}$ cm^{-2} [107]. These changes in surface charge due to the change of pH in the electrolyte, directly affect the surface potential ψ_o.

For AlGaN/GaN based sensors, first reproducible and quantitative results for pH sensing were reported in 2003 by Steinhoff *et al.* [41]. They compared different transistor structures with respect to their pH response and found that the thin surface oxide layer forming upon exposure to atmosphere is sufficient for a linear response in the range from pH 2 to 12. X-ray photoelectron spectroscopy (XPS) analysis of as-deposited GaN revealed the almost immediate formation of a thin oxide film at the surface [108]. In contrast to the established Si-based ISFETs, neither thermal oxidization nor specific ion sensitive oxide layer, e.g. Ta_2O_5 or Al_2O_3 are needed. Thus, although the site-binding model [106] was developed for Si-ISFETs [105, 109, 110], it was also proposed to explain the pH response of AlGaN/GaN-ISFETs.
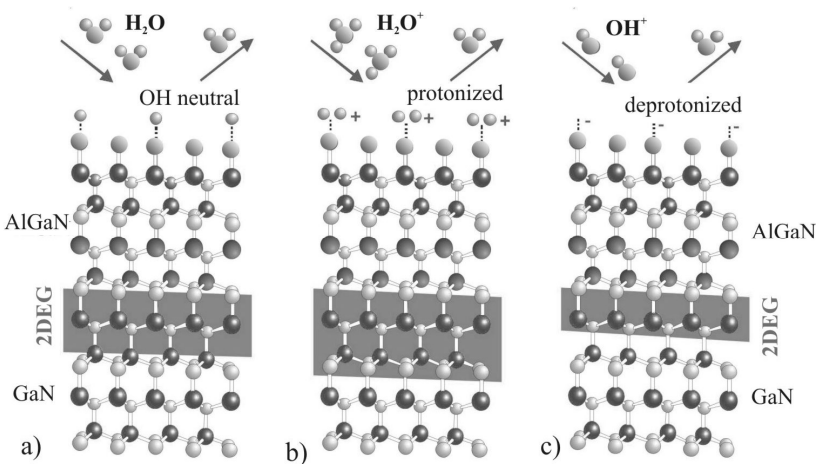

Fig. 3.7: Hydroxyl groups on the surface of AlGaN/GaN heterostructures in (a) water, (b) acidic and (c) alkaline solutions and resulting impact on the 2DEG carrier density [111]
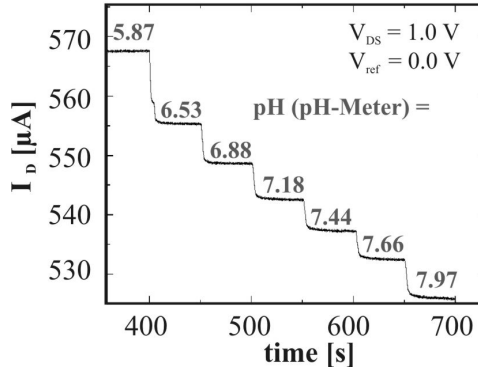
Fig. 3.8: Drain current I_D vs. pH value during a titration of KOH into HCl solution [112].

According to this model, amphoteric hydroxyl groups are bonded to Ga surface atoms (Ga-OH) when in contact with aqueous solutions, and can be protonated (Ga-OH$_2^+$), neutral (Ga-OH) or deprotonated (Ga-O$^-$) depending on the pH of the solution (Fig. 3.7) as described above. This modifies the surface charge σ_s which in turn influences the sheet charge density n_s in the 2DEG, i.e. enhancing and depleting the 2DEG at low and high pH, respectively. The resulting response of the drain current for a sensor investigated in this work is shown exemplarily in Fig. 3.8.

A theoretical study [107] employing this model and the Poisson-Boltzmann equation are in good agreement with the reported experimental results. The study also predicts that a higher sensitivity can be achieved for N-face ISFETs and through increased thickness of the oxide layer and decreased Al-content in the AlGaN-barrier.

For higher concentrated acidic or alkaline solutions, deviations from the simple site-binding model with stable amphoteric are observed. Mehandru *et al.* [100] noticed that 5 and 10 % HCl solution lead to a depletion of the 2DEG in contrast to the enhancement observed by Steinhoff *et al.* [41]. This contradiction was not further discussed, however, since very high concentrations of HCl were used (pH < 0), wet etching of the surface metal oxide is likely, which in turn reduces the number of amphoteric groups at the surface. Therefore the number of positively charged groups is also reduced leading to a decrease of the sheet carrier density in the 2DEG.

This etching of the surface oxide layer by 15 % HCl has been demonstrated by XPS analysis [78] and will be discussed in more detail in chapter 6. Similarly hysteresis effects were also observed at high pH values and attributed to modifications in the surface composition [113].

It should be noted that an alternative model for the pH response of GaN proposes the direct interaction of the electron deficient gallium in Ga-face polarity with anions [114, 115]. The response to different anions was reported to be in the range of 100 µA per concentration decade [116], which was similar to the response of the same sensors to pH. Following this approach, the pH response would arise from the interaction with OH^- ions rather that H_3O^+. They also propose that the results obtained by Mehandru *et al.* [100] are attributed to the interaction with the high concentration of Cl^- ions. Evidently, the pH response is not fully understood but the site-binding model seems to be the most suitable explanation up to now. The influence of the anionic selectivity of GaN on the sensor effect however has to be taken into consideration for further investigations.

In addition, already pH monitoring in well known solution has often shown hysteresis and drift effects [112, 117, 118], which can be attributed to instabilities of the group III nitride surface and the used passivation of the contacts. Thus, despite the well known basic AlGaN/GaN heterostructure, technological issues and passivation strategies are very important to develop sensors for "real" applications. Thus, before discussing the sensing properties of AlGaN/GaN based biosensors, the technological steps for the fabrication as well as the basic electrical characterization is described in detail in the following chapter. Comprehensive reviews on further details for growth, properties and applications of group III nitrides can be found elsewhere [67, 68, 119].

4. Fabrication and characterization of AlGaN/GaN sensors

4.1. AlGaN/GaN sensor technology

First AlGaN/GaN heterostructures for sensor applications were grown by plasma induced molecular beam epitaxy (PIMBE) [38, 41, 99, 113, 116]. More recent studies [19, 78, 100, 102, 120-122] however illustrate that most groups have switched to MOCVD. Suitable substrates for epitaxial growth include SiC or sapphire. The latter is preferred due to similar thermal coefficients compared to alumina or AlN ceramics, which is beneficial for packaging sensors for use at high temperature or in aggressive media. Moreover, transparency to visible light permits optical spectroscopy techniques in conjunction with the transparency of AlGaN. A thin AlN nucleation layer (10-150 nm) is usually grown to lower the dislocation density and thus, to improve the crystal quality. This layer also defines the polarity of the following layers to be metal-face. A GaN buffer (1-3 µm) is covered with an $Al_xGa_{1-x}N$ barrier with an Al-content of 15-30% and a thickness between 10-30 nm. To enhance chemical stability, the device is topped with a 2-5 nm GaN layer. This also facilitates Ohmic contacts to the 2DEG which are based on a conventional Ti/Al or Ti/Au metallization. Mesa etching in Cl-plasma process is usually performed to isolate the device and confine the 2DEG to the gate area [68]. Alternative methods include ion implantation [123] or UV laser cuts [112]. For the passivation of the metal contacts a multitude of additional isolating layers have been employed: SiN_x [100, 102, 120, 121], polymethylmethacrylate [121], silicon rubber [38, 99, 41], epoxy [19], and polyimide [78, 113, 116]. A summary of the structures used to fabricate biosensors is given in annex 1.

4.1.1. PIMBE and MOCVD growth of the structures

The AlGaN/GaN heterostructure was grown on sapphire substrates using PIMBE and MOCVD. Both methods are available in the Centre of Micro and Nanotechnologies (ZMN) and in this chapter the main growth parameter are summarized. The sapphire substrates were preferred because of the high crystal quality and its availability at relatively low cost compared with SiC or GaN substrates. For biosensors the transparency and chemical stability are further important criteria of substrate selection.

Last but not least sapphire is the most extensively used substrate for group III nitrides and the technology of growth is quite mature [67, 81].

The crystal orientation of sapphire and GaN is parallel but the unit cell of GaN is rotated by 30° around the c-axis with respect to the sapphire unit cell [124]. For GaN and AlN, the lattice mismatch with sapphire is about 15% and 13%, respectively, which is accommodated by an interface superstructure. The GaN growth on AlN starts pseudomorph, and relaxes after a critical thickness of about 3 nm through generation of misfit dislocations [119]. For a thickness above 100 nm, the relaxation is nearly complete and the lattice constant approaches bulk value for GaN. On top of this GaN buffer layer, an $Al_xGa_{1-x}N$ barrier is grown. The heterostructure is completed with a GaN cap layer which enhances the chemical stability of the device. The presence of other atoms (O, Si, C, N vacancies) in the crystal lattice of group III nitride are known to produce different kind of structural defects. These defects and mismatches can also influence the stability of the sensor [42].

In PIMBE, the thin films are formed in vacuum on a heated substrate through various reactions between thermal molecular beams of the constituent elements and the surface species on the substrate. In nitride growth, the metal species are provided by Ga and Al metal sources. Highly reactive atomic nitrogen is supplied by a plasma source. The growth process is controlled in situ using reflection high-energy electron diffraction (RHEED), which allows a real time evaluation and manipulation of the crystal quality and morphology. In a typical growth process, the sapphire substrate is first annealed in vacuum at 1050°C and after that is treated with active nitrogen for 2-3 min in order to build a thin AlN film by nitridation of sapphire. The growth of the AlN layer continues in the next 40 min at a temperature of about 880°C with a growth rate of 4 - 4.5 nm/min. After that the substrate temperature is decrease to 700°C and the growth of GaN buffer layer is started and continued for the next 60 min with a growth rate similar to AlN. Finally, at the same temperature the AlGaN barrier and GaN cap layer are grown. The resulting thickness of the GaN buffer is about 250 nm and was varied for the AlGaN barrier between 8 and 30 nm. The Al concentration for the biosensor was fixed at 22%. During the growth the substrate is mounted face down on a substrate holder and is rotated around its c–axis to improve uniformity. Furthermore, in order to ensure a uniform temperature all over the wafer, the backside of the substrate is covered with a layer of Ti/W metallization.

The growth of AlGaN/GaN heterostructures by MOCVD entails the transport of gas phase metal organic precursors, and transport gases to a heated substrate on which the precursors are pyrolyzed and the nitride film is deposited. The growth process depends of many parameters that have a big influence on the final material structure and properties [125].

The MOCVD epitaxial growth of AlGaN/GaN heterostructures for biosensors is accomplished at 1120°C and 50 mbar using a commercial Aixtron AIX200RF reactor. Triethylgallium, trimethylaluminum and ammonia in hydrogen served as precursors with a V-III ratio of 2000. The sapphire substrate is cleaned *in situ* by etching in a hydrogen atmosphere at 1180°C. The growth it is initiated by a low-temperature (460°C) AlN nucleation layer of about 20 nm thickness. Afterwards, a 1.2 µm thick GaN buffer layer is deposited to reach the structural quality required for the 2DEG in the AlGaN/GaN heterostructure. Finally, the growth is completed with $Al_{0.32}Ga_{0.68}N$ barrier and a cap layer of 2 nm GaN. The growth of GaN buffer layer, barrier and cap layer is accomplished at a temperature between 1030°C and 1120°C. The thickness of the barrier is between 9 and 27 nm and is grown within 1 to 3 min. A doping of the layers with Si it is possible using 50 ppm silane (SiH_4). More details about the MOCVD growth process and material properties can be found in reference [125].

Clearly, PIMBE and MOCVD growth are quite different methods and therefore also film parameters are different despite the nominal identical heterostructure design. Due to the lower growth temperature, PIMBE layers exhibit a higher number of material defects [94]. MOCVD grown material has higher structural quality; however, more impurities can be expected due to high temperature and high pressure (50-200 mbar compared to 10^{-8} mbar in MBE). Moreover, MOCVD grown layers are more homogeneous and due to the higher growth rate thicker buffer layers can be achieved. In order to characterize the influence of the different properties series of AlGaN/GaN heterostructures were grown by both methods with varying thickness and Al content in the barrier (see for example Tab. 4.1 and Fig. 4.4 for a series of samples for the investigation of pH sensing properties).

4.1.2. Device fabrication

To transform AlGaN/GaN heterostructure confining the 2DEG into a biosensor device, the technologies, which are available at ZMN, TU Ilmenau are employed

After growth, capacity-voltage (C-V) measurements are performed (chapter 3) in order to determine sheet carrier concentration n_s of the 2DEG and AlGaN barrier thickness. X-ray diffraction was performed in order to evaluate the Al concentration in the barrier and its thickness. In the following chapters the technological processes to realize an ISFET device are discussed shortly in chronological order. Prior to any technological steps, the wafers were cleaned in acetone, isopropanol and dried in N_2 flux. Optical microscopy was used for characterization during all technologic steps. A technological plan is attach at the end of this work (annex 2).

4.1.2.1. Photolithography

Photolithography is one of the most critical steps in the fabrication technologies of ISFET sensors. By photolithography, Ohmic contacts, the active area, stable bond pads and defect free passivation layer are defined. For this process it is necessary to have a mask, a standard positive photo resist and a good developer. For the fabrication of the ISFET biosensors five photolithographic steps are performed. A foil mask was used to create structures with sizes larger than 35 µm on a half wafer as illustrated in annex 2. The advantages of these masks are the very low cost and short time preparation, which enables the fast development of test structures. Standard positive resist has been AR-P 3510. KOH free developer AR300-25 (TMAH: tetrametylammoniumhydroxide) was used since KOH is known to attack group III nitrides [19, 78, 112]. After spinning the photo resist, a soft back process of 90 s at 115°C was performed. After that the wafer is introduced into a mask aligner. The system is illuminated for 4 s with a light of 365 nm wavelength. The next step is developing the structures and controling them using optical microscopy. In case of mesa etching, the photo resist is used as etching mask, which requires a further hardening at 130°C for 30 min. For all the other steps, a thin metal film is deposited on top of the developed photo resist followed by a patterning through lift-off processing. The first lithography is performed to realize the adjustment marks on the wafer. They are made by sputtering 20 nm Ti and 100 nm Al. After the definition of the adjustment marks, a mesa etching is performed.

4.1.2.2. Mesa etching

Inductively coupled plasma (ICP) mesa etching in Cl_2/Ar gas mixture [38] is used to laterally confine the active area of the ISFET sensor.

Bse pressure of the etching system is 2×10^{-6} mbar. Gases are injected through a showerhead located ~100 mm above the sample. Hgh-density ICP discharge is generated by applying 13.56 MHz rf power. The wafer is powered separately (600 W, 13.56 MHz) for reactive ion etching (RIE). Since ion energy and plasma density are effectively decoupled for the ICP-RIE system, uniform density and energy distribution are transferred to the sample with low ion and electron energies. The substrate was cooled by He flowing through the electrostatic chuck. Using this method, mesa etching of about 130 nm is performed within 100 s (Fig. 4.1).

4.1.2.3. Ohmic contacts

After etching, Ohmic contacts to the 2DEG channel were realized. Conventional optical lithography followed by a lift-off process is also used to define the metallization. For electrical characterization of the AlGaN/GaN ISFET, Ti/Al/Ti/Au-Ohmic contacts were deposited by sputtering and annealed in nitrogen atmosphere by rapid thermal processing (RTP). The characteristics of the Ohmic contacts to GaN were subject of intense research and development activities during the last years [126-128]. At the ZMN, the formation of Ohmic contacts to GaN was also studied [129] and the Ti 20 nm / Al 80 nm / Ti 30 nm / Au 100 nm was found to be the best metallization schema for our heterostructure. The Ti interlayer is of crucial importance in forming stable Ohmic contacts because it forms an alloyed contact layer to the group III nitride surface and it serves as a barrier film. The contacts become Ohmic upon annealing due to the formation of a thin TiN or $AlTi_2N$ layer at the metal/semiconductor interface, with depletion of N from the GaN, but without decomposing the crystal structure. N vacancies act as donors in GaN and in this case the interface region becomes highly n -doped, providing the configuration needed for tunneling contacts [130]. For the PIMBE grown heterostructures, an annealing at 750°C for 60 s was found to be optimal, while MOCVD grown heterostructures required a higher annealing temperature of 850°C for 50 s. To evaluate the electrical properties of the contacts a transmission line method (TLM) is used [131]. A second metallization layer with 20 nm Ti and 200 nm Au was deposited on the bond pads in order to achieve the necessary mechanical stability of the bond contacts with Au wires to the printed board or ceramic frames. An annealing of this second metallization layer was not necessary. The final sensor structures are shown in Fig. 4.1.
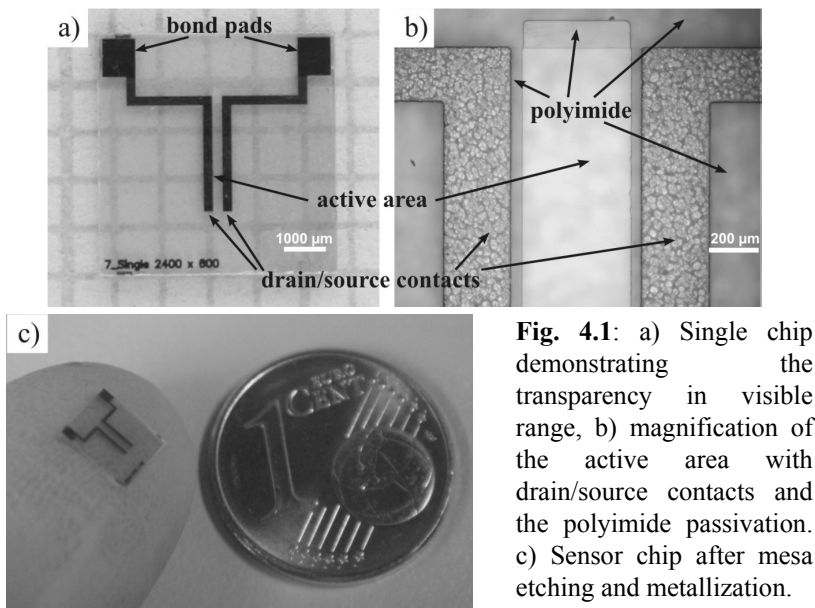
Fig. 4.1: a) Single chip demonstrating the transparency in visible range, b) magnification of the active area with drain/source contacts and the polyimide passivation. c) Sensor chip after mesa etching and metallization.

4.1.2.4. Passivation

The passivation of the sensor structure is a very important factor to achieve stability and reproducibility of the device in liquids such as electrolytes. The passivation layer eliminates the possible electrochemical reaction between metal contacts and electrolyte. Therefore the passivation must be mechanically and chemically stable in both acidic and alkaline solutions. In addition, for biosensors the layer biocompatibility it is an important requirement. At ZMN, an extensive study of possible passivation layers on GaN sensor was performed [99]; however, most of the candidates could not fulfill the requirements mentioned before.

For ISFET biosensors, the polymer polyimide PI-2610 from DuPont revealed to be the most promising passivation material. Polyimide has been used already for different sensor applications [132, 133] and has shown good chemical stability in contact with biological cells and organic solutions [78]. It is also biocompatible and facilitates cellular attachment as will be shown in chapter 6. The PI-2610 exhibits a desirable combination of beneficial film properties such as low stress, low coefficient of thermal expansion, low moisture uptake, high modulus elastic and good ductility.
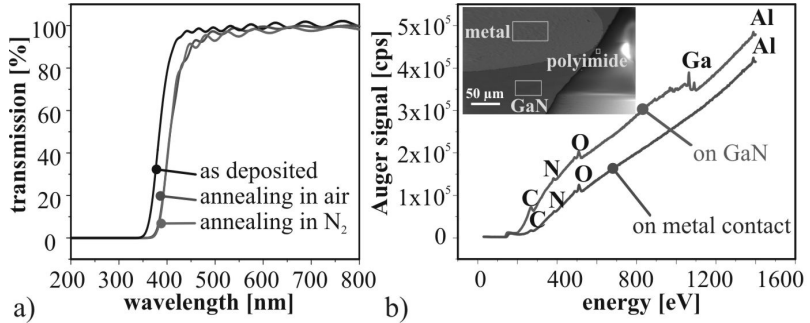
Fig. 4.2: a) Optical transmission through polyimide layer before and after curing. b) AES on the GaN surface and on metal contacts after polyimide removal demonstrating low level of residual contamination (carbon).

The transparency in visible light region is also a big advantage of this polyimide passivation material (Fig. 4.2), which allows the examination of cells using inverse optical microscopy. The dielectric constant was measured to be 2.9 and the moisture uptake of 0.5% for the PI-2610 series is relatively low for high temperature polymers [134]. The low moisture uptake is an important property for sensors working in electrolytes to avoid memory effects by modification of the passivation in dependence on the environment. The precursors for polyimide PI-2600 are dissolved in N-methyl-2-pyrrolidone (NMP), which is suitable for spin coating. After application the polyamic acid precursor is thermally cured into a fully aromatic polyimide film. For better adhesion, VM-651 adhesion promoters are used. This polyimide can also easily be patterned using conventional photolithography. In this work, a patterning scheme was developed (see annex 3) in order to passivate the contacts, but remove all polyimide from active area and bond pads. After developing and curing procedure, AES was used to verify that the active sensor area is free of organic contamination (Fig. 4.2 b).

To enhance the passivation layer stability, it is necessary to cure it in nitrogen atmosphere at a temperature of about 350°C (see annex 3). A cured polyimide layer shows very good chemical stability [134] and the signals of the final sensor device are stable and reproducible (see chapter 5). After curing procedure the polyimide thickness is found to be about 1.2 μm and the compact layer covers all the sensor contacts and the areas between the sensors leaving only the active transistor area and the bonding pads free.

After passivation the wafer is sawed into single sensor devices, which individually need an optimal encapsulation and sensor characterization.

4.1.2.5. Encapsulation

For measurements in liquids, the sensors are encapsulated using two kinds of holders (Fig. 4.3). The first variant uses a printed board circuits (PBC) holder with Cu metallization, where the chip is glued on using silicon rubber. The contacts are made with Ag paste or by bonding technique using Au wires. This encapsulation can be realized very quickly, it is flexible (the sensor chip can be taken out and mounted again without to be damaged) but has the disadvantage of instable contacts (using clamps), which can generate undesired noise effects and which have to be replaced from time to time. The second encapsulation variant was chosen in order to avoid these noise effects and to allow the use of the sensor for longer time without renewed encapsulations. For this, a special low temperature cofired ceramics (LTCC) frame was designed. LTCC technology is typically used in the fields of rf-circuits, automotive, avionic and medical electronics. This multilayer technique is based on glass- or glass-ceramic composites with a sintering temperature of less then 920°C. Unfired tapes of this material have a typical thickness of 50 to 300 μm and are easily to structure by punching or laser cutting. Passive electrical elements like conductors, resistors or capacitors can be applied on the unfired tapes by screen printing. The final result of the stacking, lamination and sintering processes is a rigid substrate with high reliability and chemical resistivity [135].

The substrates, which are used for the biosensors in this work, were produced with the DuPont 951 Green Tape® system. Four tapes with an unfired thickness of 254 μm were structured by laser cutting to form the LTCC chip carrier. Conductor lines are made from gold layers and are passivated by an additional LTCC layer of 50 μm thickness. The LTCC material offers a thermal coefficient for expansion (TCE) of 5.8 ppm/K, Young's modulus of 152 GPa and a thermal conductivity of 3.0 W/(m*K) [136]. The sensor chip is glued on this ceramic using "Vitralit 5603" (2-hydroxyethylmethacrylat) paste from Panacol-Elosol GmbH and contacts are bonded with Au wires using ultrasonic bonding at a sample temperature of 150°C. Finally they are passivated with silicon rubber using a "Dispense Masters" from firma DIMA, SMTSystems. This second encapsulation is not flexible and requires longer time to be realized. After encapsulation, the sensor device was characterized as described in the following chapter.
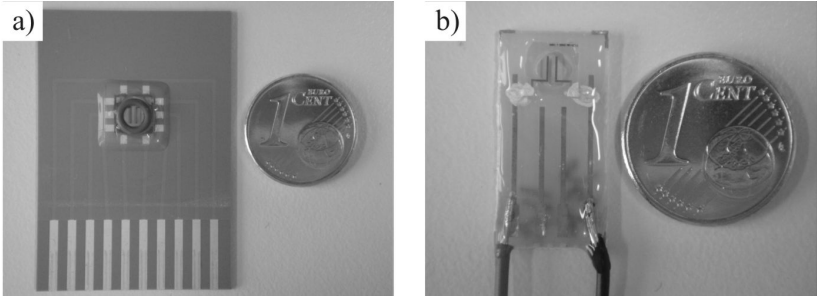
Fig. 4.3: Encapsulation of the sensor chip: a) on a LTCC frame, b) on conventional PBC frame.

4.2. Characterization of AlGaN/GaN structures

After growth, the AlGaN/GaN heterostructures were characterized to evaluate electronic characteristics, crystal quality, and surface properties. Main techniques for the surface analysis have been atomic force microscopy (AFM), scanning electron microscopy (SEM), Auger electron spectroscopy (AES), and the investigation of the surface wetting behavior. XRD, ellipsometry, transmission electron microscopy (TEM), *C-V-* and Hall measurements are used to characterize crystal structure, chemical composition and electrical properties. TLM is applied to investigate the metal contacts to the group III nitride heterostructures. All these measurements have been performed at ZMN. In this chapter, the electrical investigation of the AlGaN/GaN heterostructures by C-V and Hall measurements will be presented in more detail and the results will be discussed. The surface properties will be discussed in chapter 5.

4.2.1. Measurements methods

4.2.1.1. *C-V* measurements

C-V measurements are commonly used to obtain information about the sheet carrier concentration in the confined 2DEG and the thickness of the AlGaN barrier. The measurements are performed using a mercury probe with a Solartron Impedance/Gain–Phase Analyzer 1260 and the Dielectric Interface 1296 for impedance measurements [42]. For these measurements, no special sample preparation is needed. Only two circular concentric front contacts realized by liquid mercury are used.

The inner circular contact dot with a diameter of nominally 786 μm forms the Schottky contact, while the outer ring with 50 times larger area realizes the Ohmic contact. A vacuum pump pushes mercury against the wafer. For a given vacuum range, the size of the dot contact is very well defined. The capacitance C of the devices is approximated by a parallel plate capacitor, which is given by:

$$C = \frac{\varepsilon_0 \varepsilon_r A}{x_d},$$
(4.1)

where ε_r is the dielectric constant of the material ($\varepsilon_0 = 8.85 \times 10^{-14}$ C/Vcm), A is the area of the Schottky contact (mercury inner dot), and x_d is the distance between the capacitor plates. In the case of AlGaN/GaN heterostructures x_d is approximately the distance from the surface to the 2DEG. The carrier concentration can be determined as a function of the voltage applied to the Schottky contact to the measured differential capacitance per unit area [84]:

$$N_{CV} = \frac{C^3}{e \varepsilon_0 \varepsilon} \frac{dV}{dC}.$$
(4.2)

For homogeneously doped semiconductors, the determined carrier concentration is equal to the free carrier concentration in the layer. In the case of the investigated AlGaN/GaN heterostructures, carriers are electrons, and by integrating equation (4.2) it is possible to obtain information about the sheet carrier distribution in the heterostructure and the 2DEG:

$$n_s = \int_{-\infty}^{\infty} N_{CV}(x_d) dx_d = \int_{-\infty}^{\infty} n(x) dx.$$
(4.3)

If the applied potential on the Schottky contact is negative, the 2DEG will be depleted. The dependence of the sheet carrier density in the confined 2DEG on the properties of the AlGaN barrier (Al content and thickness) is well investigated [42, 84]. In accordance to these studies, a decreasing of the 2DEG density was observed for smaller Al contents or thinner AlGaN barriers, which also causes a lower negative voltage to achieve depletion of the 2DEG.

This measurement method is very easy to perform but is not very precise. Because the setup uses mercury to define the Schottky contact to semiconductor, the quality of the measurements critically depends on the accurate contact area, which is affected by several factors such as:

> ➢ mercury quality,
> ➢ vacuum level,
> ➢ sample surface roughness and
> ➢ cleaning of the semiconductor surface.

For this reason, this method is mainly used to obtain first information about the 2DEG and its presence in the AlGaN/GaN heterostructure. To obtain more precise information about the quality of the 2DEG and heterostructures parameters, Hall measurements are more adequate.

4.2.1.2. Hall measurements

The Hall measurement is a standard technique for electrical characterization of semiconductors. By this method, the carrier type, the concentration and the mobility in semiconductors can be determined. Usually these measurements are performed with Ohmic contacts in van der Pauw geometry. A quadratic mesa of 5 x 5 mm² was defined and etched on every wafer and standard Ti/Al/Ti/Au Ohmic contact (see chapter 4.1.2.3) are deposited in every corner. The contacts are circular with a diameter of 500 µm. For the measurements an Accent HL5500PC system was used.

The Hall effect is related to the force that acts on charged particles that moves in a magnetic field. In general case of arbitrary velocity and magnetic field directions, the force is defined as Lorentz force:

$$\vec{F} = q\vec{v} \times \vec{B},\tag{4.4}$$

where q is elementary charge ($q = -e$ for electrons and $q = +e$ for holes); v is the particle velocity and B is the magnetic flux density.

The Hall voltage which generates the force opposite to Lorentz force is:

$$U_H = \frac{1}{qn}\frac{I}{d}B_z,\tag{4.5}$$

with d: sample thickness, n: bulk electron concentration, I: current which flows in the semiconductor and B_z: magnetic flux perpendicular to the current. When the effect was discovered in 1879 by Edwin Hall, he observed that the electric field is directly proportional to the magnetic flux density and the current is inversely proportional to the sample thickness,

$$U_H = R_H \frac{I}{d}B_z,\tag{4.6}$$

where the proportionality factor R_H is now known as the Hall coefficient. Comparing the equations (4.5) and (4.6) the Hall coefficient is obtained by:

$$R_H = \frac{1}{qn} = \frac{\mu_n}{\sigma},$$

$$(4.7)$$

where μ_n and σ are the Hall mobility and the conductivity, respectively. According to van der Pauw [137], it is possible to measure the specific resistivity $\rho = \dfrac{1}{\sigma}$ and the Hall effect on an arbitrary shaped sample. Then the measured sample has to fulfill the following requirements:

> ➤ the thickness of the sample must be constant,
> ➤ the contacts are small compared to the sample size and must be positioned on the sample edge, and
> ➤ the surface must form an uninterrupted coherent area.

Using the experimental parameters I, t_s and B_z and by introducing them in the upper equations, the parameters V_H and R_H are determined and the sheet carrier concentration and the mobility are calculated.

4.2.2. Characterization of the MBE and MOCVD grown heterostructures

To find the proper heterostructure for cell based biosensors, different samples were grown using the two at the ZMN available growth methods. In the following discussion three samples by PIMBE and four samples by MOCVD (Fig. 4.4) with varying barrier thickness are compared (table 4.1).
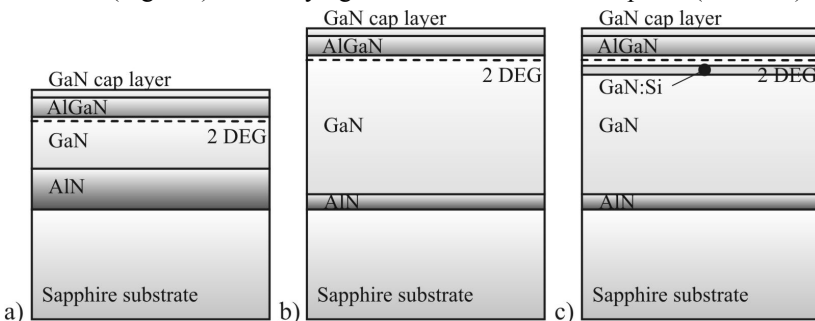

Fig. 4.4: Undoped a) PIMBE and b) MOCVD heterostructures for ISFETs, as well as c) modified MOCVD heterostructure with doped GaN interlayer.

Table 4.1: AlGaN/ GaN heterostructure parameters

Sample	AlN nucleation	GaN buffer	AlGaN barrier*	GaN Cap layer
PIMBE: I II III	180 nm	270 nm	d_1 = 10 (10.3) d_2 = 13 (12.1) d_3 = 15 (13.7)	2 nm
MOCVD: IV; V VI VII	20 nm	1200 nm	d_1 = 10 (8.1; 8.5) ** d_2 = 15 (14.3) d_3 = 20 (18.4)	2 nm

    * The barrier thickness is calculated from growth rate and in brackets from *C-V* measurements (GaN cap layer is included).

    ** Modified MOCVD heterostructure with Si doped GaN interlayer.

    The Al content in the AlGaN barrier is fixed at 22% and 32% for PIMBE and MOCVD grown heterostructures, respectively. In order to ensure good transparency of the sensor for additional optical analysis of cellular activity, the sapphire substrate is polished on both sides. In MOCVD grown heterostructures with thinnest barrier (sample IV, V), an additional Si-doped GaN layer is included close to the AlGaN/GaN interface (Fig. 4.4c). It enhances sheet carrier concentration in the confined 2DEG and minimizes persistent photocurrent effects, which are often present in group III nitrides [42, 125]. After growth, the wafers were routinely characterized by *C-V*. These results are summarized in Fig. 4.5. As expected, a decreasing of the AlGaN barrier thickness results in increased capacity at 0 V, while increasing sheet carrier density in the confined 2DEG shifts the threshold voltage to more negative values.

    The calculated N_{CV} profiles for the PIMBE and MOCVD heterostructures are shown in Fig. 4.6. The dependence of the electrical properties on the barrier thickness and the Al concentration is obvious as already mentioned before. For the PIMBE grown samples, the lower Al concentration in the barrier decreases the sheet carrier concentration in the confined 2DEG. Therefore, depletion starts for PIMBE grown samples already at small applied potentials. For both techniques an increasing barrier thickness directly results in a higher electron concentration in the confined 2DEG. In the case of the samples with Si doped GaN interlayer, an enhancement of carrier concentration is observed close to the interface.
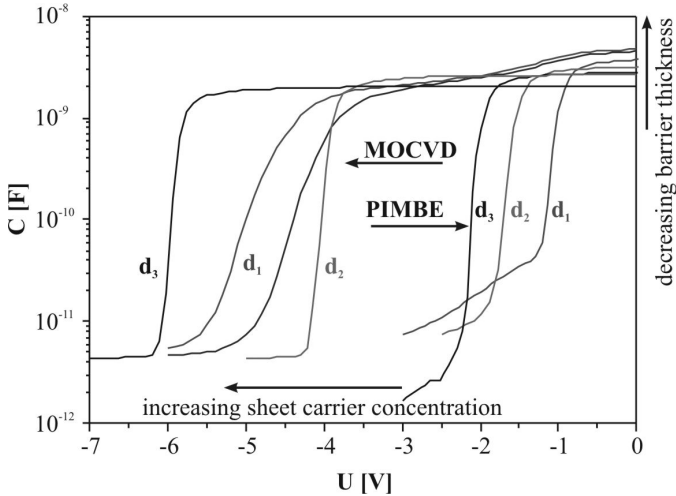
Fig. 4.5: *C-V* measurements for the AlGaN/GaN heterostructures.
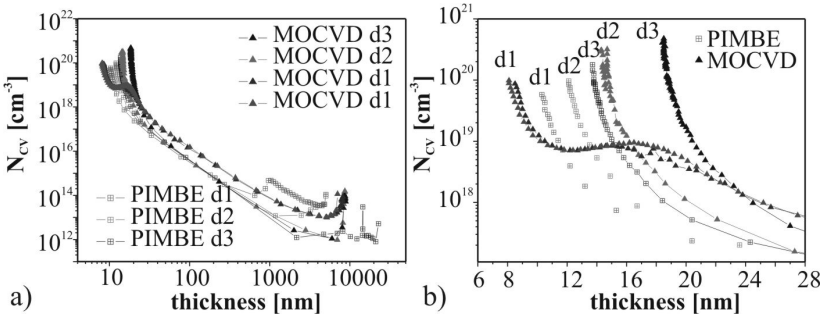

Fig. 4.6: *C-V* concentration profile for PIMBE and MOCVD grown samples with different barrier thicknesses: a) whole AlGaN/GaN depth profile, b) detailed view of the topmost layers. The abnormal behavior of the sample with thinnest barrier is caused by Si doping of the buffer.

Hall data are in good agreement with the experimental results from *C-V* profiling. Except the results from doped samples, all data fit very well with the calculated 2DEG density for a critical barrier thickness (Fig. 4.7) from Ibbetson *et al.* [95]. With decreasing barrier thickness also the sheet carrier concentration is decreasing and below a critical barrier thickness, no 2DEG is confined anymore at the interface of the AlGaN/GaN heterostructure.
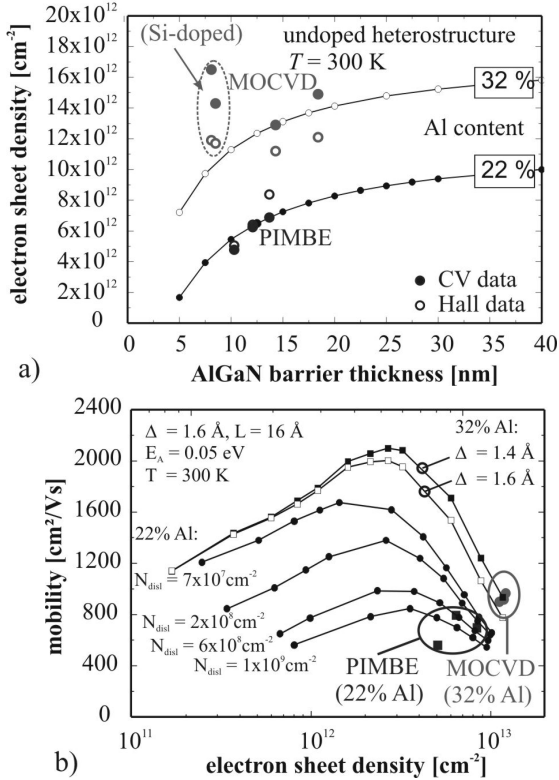
Fig. 4.7: Comparison of measured transport properties in AlGaN/GaN heterostructures with simulations: a) electron sheet carrier concentration vs. barrier thickness for the two investigated Al concentrations. Marked points represent the results on heterostructures with additional Si-doped interlayer. b) 2DEG mobility at $T = 300$ K as a function of electron sheet density for different threading dislocation densities N_{disl}. The interface roughness parameters are the root mean square Δ and the correlation length L [138].

A theoretical study of the transport properties in AlGaN/GaN heterostructure has been performed by Polyakov [138].

Table 4.2: Summary of the results of the *C-V* and Hall measurements.

Barrier [nm]	n_s - CV [cm^{-2}]	n_s - Hall [cm^{-2}]	μ [cm^2/Vs]	R_s [Ω/]
PIMBE				
10	$4.78*10^{12}$	$5.06*10^{12}$	563	2192
13	$6.26*10^{12}$	$6.41*10^{12}$	798	1221
15	$6.88*10^{12}$	$8.38*10^{12}$	700	1065
MOCVD				
10	$1.65*10^{13}$	$1.19*10^{13}$	920	571.6
10	$1.43*10^{13}$	$1.17*10^{13}$	918	579.8
15	$1.29*10^{13}$	$1.12*10^{13}$	901	577.4
20	$1.49*10^{13}$	$1.21*10^{13}$	969	570.7

The electron density and the low-field mobility of the carriers in AlGaN layer have been calculated by self-consistent solving the Schrödinger and Poisson equations and by ensemble Monte Carlo (EMC) simulations, respectively.

Material and band structure parameters of ternary AlGaN barrier layer have been obtained through the linear interpolation between binary GaN and AlN constituents. The sheet density is manipulated by a variation of the voltage applied to the AlGaN/GaN heterostructure. The positive polarization bound charge at the AlGaN/GaN interface formed due to the polarization discontinuity was considered as that for the unrelaxed AlGaN barrier layer [67]. However, due to a finite barrier height of the AlGaN/GaN heterojunction, the electron wave functions were allowed to penetrate into the AlGaN barrier layer, which can remarkably modify the interface roughness scattering rate [139]. Thus, depending on the interface quality, the mobility can change significantly, and at low sheet carrier densities, the presence of impurities diminishes the mobility [84].

To characterize an interface roughness, the root-mean-square (rms) Δ (average height of terraces present at the surface or/and interface) and the correlation length L (average length of terraces) were used. As third parameter characterizing the structural quality of the heterostructures, the dislocation density N_{disl} was varied (Fig. 4.7b). Other details of the theoretical model including scattering mechanisms due to phonons and charged threading dislocations can be found elsewhere [138].

For this study, the input parameters were adapted to the experimental conditions for the investigated heterostructures, especially for the dislocation density, the barrier thickness and the Al concentration in the barrier. It was found that for high electron sheet densities (strong electron accumulation in the near-interface region) the low-field mobility is mostly limited by the interface roughness scattering.

The low-field mobility calculations for $\Delta = 1.6$ Å and $L = 16$ Å, which roughly coincidences with the morphology studies on AlGaN/GaN heterostructures [125], are plotted in Fig. 4.7b. The dislocation as the remaining free parameter was varied by two orders of magnitude. For the MOCVD grown samples, a good agreement between simulation and experiment is achieved for dislocation densities below 10^9 cm^{-2}, which is consistent to the value $\sim 1.5*10^9$ cm^{-2} obtained by preferential wet etching and AFM analysis [125]. In contrast, the lower mobility values for the PIMBE grown heterostructures imply a significantly higher dislocation density about 10^{10} cm^{-2} [94], which might be a consequence of the lower growth temperatures and the lower GaN buffer layer thickness.

In summary, the electrical characterization of the selected heterostructures revealed that MOCVD grown samples are more homogeneous and exhibit superior electronic transport properties. The lower electrical performance in PIMBE grown samples is mainly caused by the higher dislocation density.

This effect has important consequences for the application as chemical or biosensor, since such defects are preferentially etched and can be the origin of early breakdown for such sensing devices. Moreover, it has been shown that high dislocation densities in PIMBE grown samples also limit the possibilities of cleaning in alkaline solutions, which is a required procedure for applications in food industry [67].

On the other side, smaller negative potentials are necessary to be applied to deplete the 2DEG in PIMBE grown heterostructures. For biosensors, it is very important to work with small potentials close of the cells in order not to influence the measured cell signals. It is also important for encapsulations and contacts passivation. Moreover, PIMBE grown heterostructures have shown to exhibit a better light stabilities [42, 140]. In the case of MOCVD growth, the Si doped interlayer was necessary to achieve a similar or even improved behavior.

For this reason, a more detailed study on the sensing properties of the different heterostructures is necessary in order to select appropriate devices for biosensing. In the next chapters these heterostructures will be characterized as pH sensors, which represent the basic element for almost all electronic biosensors. Important parameters such as drift and reaction to different buffer solutions will be evaluated and discussed.

5. AlGaN/GaN heterostructures as pH sensors

One of the major tasks for biosensors is to monitor the ion fluxes and concentrations [141]. In electrolytes, most of the processes can be translated into changes of the H^+ concentration and, thus, to the pH value. In consequence, the pH sensors are a reliable base for biosensors in order to detect different reactions which take place *in vitro* or *in vivo*. In the following chapter, an introduction into the definition and the measurement of the pH value in electrolytes is given and the behavior of AlGaN/GaN heterostructures as pH sensors is investigated in detail.

5.1. Introduction to the pH value

pH describes the concentration of H^+ cations in a solution. In solution, solvated protons (H^+) appear as hydronium ions H_3O^+. The concentration of these ions can change in very wide range - most often it has values lying between 1M and 10^{-14}M. In some extreme cases, even higher and lower concentrations can be observed. Using numbers differing by many orders of magnitude is impractical; thus, in 1909 Danish biochemist Søren Sørensen developed the pH concept and introduced a pH definition as negative decimal logarithm of $[H^+]$:

$$pH = -\log([H_3O^+]).$$ (5.1)

The pH defined in this way can be used exactly only to calculate pH for diluted solutions of acids and bases in water. A more precise definition uses the ion activities *a* and not their concentration. In the case of much diluted solutions (below 0.001M), the difference between concentration and activity can be neglected. For highly concentrated solutions, it has to be taken into account and then the pH can be defined as:

$$pH = -\log(a_{H_3O^+})$$ (5.2)

The so defined pH is called "thermodynamic pH" as opposed to "concentration pH" (equation 5.1) and all pH meters measure it as result of the Nernst equation (see chapter 5.1.2).

5.1.1. Acids, bases and pH scale

The pH definition enables to establish the pH scale. In water solutions, the pH is limited in the range 0 – 14, while in other solvents pH values can be negative or higher than 14. Aqueous solutions always contain H_3O^+ and OH^- ions, either from water dissociation or from introduced bases or acids. In pure water at 25°C, the concentration of these two ions is equal, the pH is defined as neutral and its level is 7. Solutions containing more H_3O^+ than OH^- ions have a pH value lower than 7 and are known as acids. A solution in which the concentration of OH^- exceeds those of H_3O^+ has a pH value greater than 7 and is known as base. The pH determination of a solution is usually obtained by comparing unknown solutions to those of known pH. For easy comparison of the different solutions or samples, the pH scale is widely use. In organisms, the pH of different fluids varies with its function. Mostly it is tightly regulated to keep the system in an acid – base equilibrium. To get a better feeling about the pH scale, it is worth to remember few pH values (Table 5.1)

Table 5.1: pH value of some fluids.

Gastric juice:	0.7
Lemon juice:	2.4
Milk:	6.5
Arterial blood plasma:	7.34 – 7.45
Secretions of pancreas:	8.1
Hand soap:	9 - 10

Most solutions containing different ions are in state of equilibrium - all concentrations are constant and not changing in time. This equilibrium is dynamic, which means that forward and reverse reactions in the solution have the same rate. By using classical chemical calculation, the equilibrium in the solution being a mixture of water, acid and base can be calculated. Finding such equilibrium is always a part of pH calculation – and once pH is known, the calculation of all other ion concentrations is realizable.

Let's assume the acid HA, a base B and their analytical concentrations are C_a and C_b, respectively. For the acid ionization reaction

$$HA + H_2O \Leftrightarrow H_3O^+ + A^-, \tag{5.3}$$

the equilibrium is described by the acid ionization constant defined as:

$$K_a = \frac{[H_3O^+][A^-]}{[HA]}. \tag{5.4}$$

For the base ionization reaction

$$B + H_2O \Leftrightarrow BH^+ + OH^-, \tag{5.5}$$

the base ionization constant is defined as

$$K_b = \frac{[BH^+][OH^-]}{[B]}. \tag{5.6}$$

As additional, frequently used parameter to describe dissociation, a dissociation fraction is defined as ratio of the concentration of dissociated molecules to the concentration of all molecules in the solution

$$f_p = \frac{[A^-]}{C_a}. \tag{5.7}$$

It is commonly believed that strong acids and strong bases are fully dissociated. For most practical purposes this is valid, but due to their finite dissociation constants, in some cases partial dissociation can be observed. All chemical reactions are considered to occur in water and the water itself dissociates into H_3O^+ and OH^- ions

$$H_2O + H_2O \Leftrightarrow H_3O^+ + OH^-. \tag{5.8}$$

This reaction represents dynamic equilibrium between hydronium ions, hydroxide ions and water molecules. The equilibrium constant for this proton transfer reaction is called water equilibrium constant K_W defined as:

$$K_W = [H_3O^+][OH^-]. \tag{5.9}$$

Taking the logarithm of both sides of equation (5.9):

$$\log(K_W) = \log([H_3O^+]) + \log([OH^-]), \tag{5.10}$$

or, using the definition of equation (5.1) in "p" notation:

$$pK_W = pH + pOH. \tag{5.11}$$

Bronsted and Lowry proposed independently in 1923 new definitions of acids and bases:

An acid is a substance that can donate a proton and a base can accept a proton. The most important outcome of this definition is that every acid loosing its proton becomes a Bronsted-Lowry base and that every base when protonated becomes a Bronsted-Lowry acid. These pairs of acids and bases are called conjugated. Thus, every acid loosing a proton becomes its conjugated base, and every protonated base becomes its conjugated acid.

Let's take a reaction of conjugated base A⁻ with water:

$$A^- + H_2O \Rightarrow HA + OH^-. \tag{5.12}$$

Its equilibrium constant is

$$K_b = \frac{[HA][OH^-]}{[A^-]}. \tag{5.13}$$

Multiplying this equation with equation (5.4), yields:

$$K_a K_b = [H_3O^+][OH^-] = K_W, \tag{5.14}$$

or, in "p" notation

$$pK_a + pK_b = pK_W. \tag{5.15}$$

The most important outcome is that to describe acid/base properties of a substance in the solution (which is not necessarily to be a water solution) it is possible to use either the K_a or K_b value.

5.1.2. Nernst law

As mentioned above, only the thermodynamic pH can be measured and this is a direct consequence of the Nernst law. The Nernst equation describes the potential in an electrochemical cell as a function of concentrations of ions taking part in the reactions:

$$E = E_0 - \frac{RT}{nF}\ln(Q), \tag{5.16}$$

where Q is the concentration or activity quotient, n the number of exchanged electrons, and F the Faraday constant. For a given temperature, the expression RT/F has a constant value. To simplify the calculations, it is often combined with a conversion factor between natural logarithm (ln) and decimal logarithm (log) resulting in a value of 0.0591 for 25°C.

Most ion sensors are potentiometric sensors, i.e. the electrical potential difference $\Delta\varphi$ at a solid/liquid interface as function of the ion concentration is measured. In this case, the Nernst equation can be written:

$$\Delta\varphi = \frac{RT}{F}\ln a_{Me^+},$$ (5.17)

where a_{Me} is the activity of one type of ions. In this case the maximal potential difference for a pH electrode is 59 mV/pH [104, 142].

For measuring the pH value, the well-known glass electrode makes use of a membrane of conducting glass, which buffers ions of interest in a thin surface layer of the membrane. Glass compositions that are sensitive to specific ions such as H^+ (pH), Na^+ (pNa), K^+ (pK), Ca^{2+} (pCa) and others have been developed. These sensitive glasses are bulb-shaped and molten to a glass shaft. The internal volume of the bulb with its shaft is filled with a liquid of known, constant composition. Thus, an electrochemical cell is built with a constant potential drop at the inner surface of the glass membrane and a "sense potential" at its outer surface, both according to the Nernst equation. The potential drops can only be measured by contacting both, the internal solution as well as the external solution, in which an ion concentration has to be measured, by reference electrodes. A reference electrode is a contact between a metal wire with fixed electrochemical potential and an aqueous solution to determine the electrical potential of this solution. In practice, a reference electrode consists of a chlorinated silver wire (silver coated with insoluble silver chloride) in a KCl solution with constant concentration. This electrochemical couple has constant potential according to the Nernst equation. The inner solution of a reference electrode realizes the contact with the solution, from which the electrical potential has to be measured, by means of a barrier, the so-called frit. Often glass membrane electrodes are combined with reference electrodes in one system.

Applied to the full cell formed from the two junctions inside and outside of the pH glass electrode, the Nernst equation takes the form:

$$E = E_0 - 0.0591\log\frac{[H_3O^+{}_{inside}]}{[H_3O^+{}_{outside}]} = E_0 + 0.0591(pH_{outside} - pH_{inside}).$$ (5.18)

The pH inside of the electrode has known constant values, thus, equation (5.18) can be modified:

$$E = E_0' + 0.0591 pH_{outside}.$$ (5.19)

These equations describe the behavior of the glass electrode used for pH measurements. Although glass membranes are versatile, they have some shortcomings. They are fragile, chemically instable in strong basic solutions and, finally, they must be calibrated before each use because their characteristics change with time and exposure to solutions. For all this reasons, many efforts were made to develop new types of pH sensitive sensors. One of these sensors is the ISFET based pH sensor. Up to date, all this sensors need a calibration procedure, which can be done using buffer solution of known pH. To improve the accuracy of the measurements, two or more buffer solutions of different pH values are used for calibration. These buffer solutions are described in the following chapter.

5.1.3. Buffer solutions

Solutions able to retain constant pH regardless of small amounts of acids or bases added are called buffers. Their resistance to changes in pH makes buffer solutions very useful for chemical manufacturing and essential for many biochemical processes. The ideal buffer for a particular pH has a pK_a equal to the pH desired, since a solution of this buffer would contain equal amounts of acid and base and be in the middle of the range of buffering capacity. Buffer solutions are necessary to keep the correct pH for enzymes in many organisms to work. Many enzymes work only under very precise conditions; if the pH strays too far out of the margin, the enzymes slow or stop working and can denature, thus permanently disabling its catalytic activity. A buffer of carbonic acid (H_2CO_3) and bicarbonate (HCO_3^-) is present in blood plasma, to maintain a pH between 7.35 and 7.45. Industrially, buffer solutions are used in fermentation processes and in setting the correct conditions for dyes used in coloring fabrics. They are also used in chemical analysis and calibration of pH electrodes or sensors.

Classical buffers contain solutions of weak acids and its conjugated bases as major species. Small additional amounts of acids or bases added are absorbed by the buffer and the pH changes only slightly. In case of high or low pH, only solutions of strong acids or bases are used. For example, in case of pH = 1, the acid concentration is relatively high (0.1 M) and small addition of acid or base cannot change the pH of such solution significantly.

To calculate the pH of buffer solutions containing both acids and conjugated bases, the acid ionization constant defined in equation (5.4) is used in logarithmic form:

$$\log K_a = \log[H_3O^+] + \log\left\{\frac{[A^-]}{[HA]}\right\}. \tag{5.20}$$

Multiplying both sides of equation by -1 allows the use of pK_a and pH instead of $\log K_a$ and $\log [H_3O^+]$ and equation (5.20) can be rewritten as:

$$pK_a = pH - \log\left\{\frac{[A^-]}{[HA]}\right\}. \tag{5.21}$$

This so called Henderson-Hasselbalch equation (or buffer equation) can be used to calculate the pH of solutions containing pairs of acids and conjugate bases such as HA/A^-, HA^-/A^{2-} or B^+/BOH. The Henderson-Hasselbalch equation is mostly used to calculate the pH of solution created by mixing known amounts of acids and conjugate bases or by neutralizing acids with strong bases.

> ➢ The organic HEPES buffer is commonly used to maintain pH levels of basal media in cell culture. HEPES is suitable for buffering in the physiological pH range of 7.2-7.6. HEPES buffering system can be used with or without a CO_2 atmosphere. Our study in case of NG 108 – 15 cell cultures show a good behavior for a concentration of 25mM (see chapter 7).
> ➢ TRIS is an extensively used component for buffers in biochemistry especially for solutions of nucleic acids. It is a primary amine and thus undergoes the reactions associated with typical amines.
> ➢ A phosphate is a salt of phosphoric acid. Phosphate is also used in animal cells as a buffering agent. The kinds of phosphate that are useful as buffers include and H_2PO_4-NaH_2PO_4 and Na_2HPO_4 (Sørensen buffer).
> ➢ CS11 was used for titration experiments and prepared immediately prior to use.
> ➢ Finally, a standard buffer system from Mettler Toledo (MT) with fixed pH of 4, 7, and 10 was used for the characterization and calibration of the PIMBE and MOCVD sensors. This commercially available buffer has unknown composition.

These buffer solutions with known, fixed pH value are the base for the characterization and the calibration of the sensors, which is described in the following chapter.

Table 5.2: The buffer solutions used in this work [142, 143].

name	pK$_a$ at 25°C	buffer range	mol. weight	full name and molecular formula
HEPES	7.48	6.8 - 8.2	238.3	n-2-hydroxyethylpiperazine-N'-2-ethanesulfonic acid; $C_8H_{18}N_2O_4S$
TRIS	8.06	7.5 - 9.0	121.14	2-amino-2-hydroxymethyl-propane-1,3-diol; $C_4H_{11}NO_3$
CS11	12	5-8		citrate 25 mM + bis-tris-propane 75 mM $NaH_2PO_4 + Na_2HPO_4$
Mettler-Toledo		4-10		unknown

5.2. Setup for the sensor characterization

For basic characterization of sensors in buffer solutions as well as for the measurements with cells, which are described in chapter 7, two different measurements setup were used (Fig. 5.1). In both cases, the electrolyte bath chamber was realized from PEEK (polyetherketone) by conventional fine mechanic techniques. The advantage of this material is the high chemical stability, the very small conductivity and the easy process technology.

Due to the transparency, low cost and good mechanical properties, Plexiglas was used as holder for the sensor chip, which is encapsulated on PBC (Fig. 5.1a, for the sensor see Fig. 4.3b). Because of these properties the same material was also used as lid for the constructed electrolyte chamber in order to prevent evaporation processes and alkalization of cell medium as the result of CO_2 consumption at room temperature (see chapter 7). The disadvantage of Plexiglas material is the small conductivity, which cannot permit ground contact or screening of the sensor chip to electromagnetic noise. Moreover, the possibility of electric charging can influence the sensor signal by touching the lid during measurements.

A second measurements setup for the LTCC encapsulated sensor chip (Fig. 5.1b, for sensor see Fig. 4.3a) is more electrically stable. It employs an Al holder for electrical screening and mechanically robust contacts.
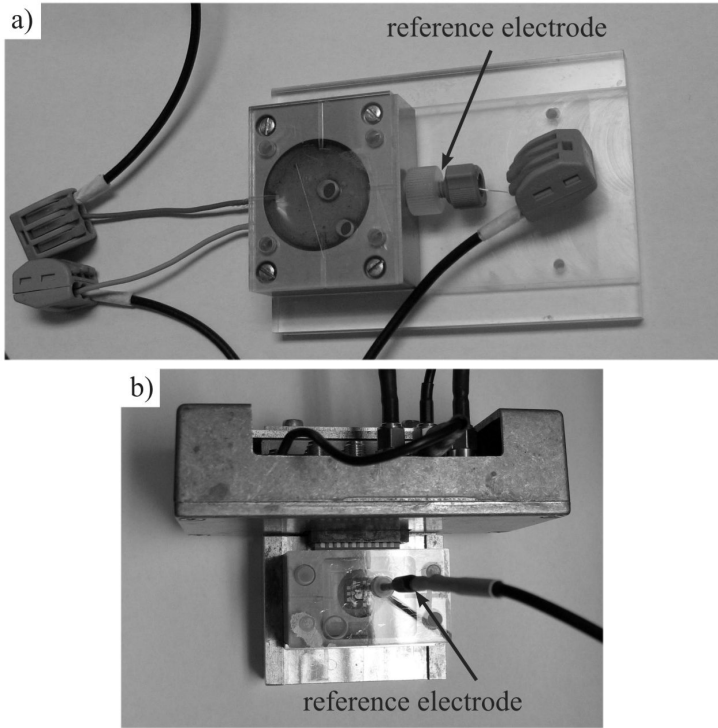
Fig. 5.1: Measurements setup for AlGaN/ GaN sensor characterization and cells research a) on PBC, b) on LTCC.

Three types of reference electrodes can be used with these two systems (Fig. 5.2):

➢ a double cell glass reference electrode InLab from Mettler-Toledo, which have an ARGENTHAL™ lead off and silver ion trap that ensures that the electrolyte remains completely free from silver ions,

➢ a self-made reference electrode with a 2 mm Ag/AgCl pellet incorporated in an agarose gel from Fermentas [144] with 120 mM KCl solution, and

➢ a leak free Amani reference electrode from Warner Instruments with a unique chemically resistant, highly conductive (10 KΩ), and not porous junction.
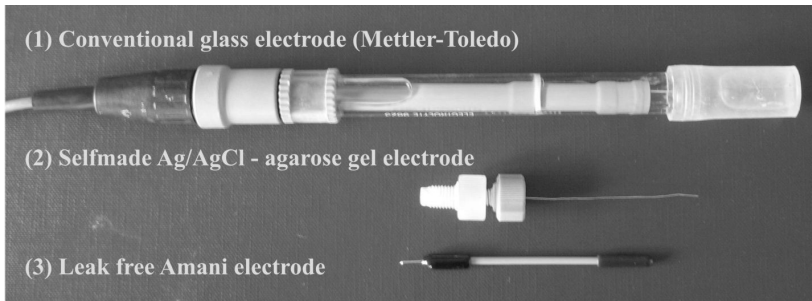
Fig. 5.2: Reference electrodes use together with the measurements setup

The characterization of the different reference electrodes is discussed in context with the noise and drift behavior in chapter 5.3.4. Both measurements setups were successfully used to characterize the AlGaN/GaN FET based sensors described in the next chapter as well as for cell measurements (chapter 7).

5.3. AlGaN/GaN sensor characterization

Before any performance of quantitative measurements, the sensors have to be calibrated, which is accomplished using a known and well defined pH buffer solution (in this case the MT standard buffer solution was used). Calibration means to record the transistor characteristics, to establish its working point and to determine the sensor sensitivity at different pH values. A good pH sensor must show sensitivity to H^+ ions in accordance to the Nernst law. The transistor characteristics are discussed in the following chapter. Based on this, properties of the sensor such as signal to noise ratio and drift behavior of AlGaN/GaN pH sensors are evaluated.

5.3.1. Sensors characteristics

First, the transistor characteristics of the AlGaN/GaN sensor were recorded in neutral MT standard buffer solution at pH7. Fig. 5.3 shows the output characteristics for an open gate AlGaN/GaN FET grown by PIMBE with gate dimensions of 2400 x 500 μm² and an AlGaN barrier thickness of 13 nm. The measurement setup for PBC encapsulated sensors was used and the self made reference electrode with 120 mM KCl in agarose gel was chosen.
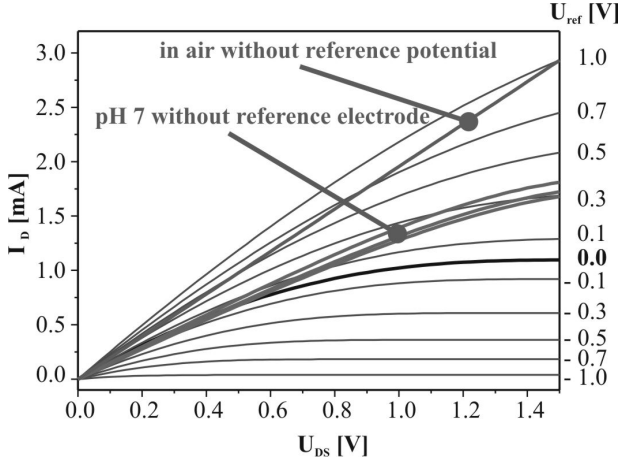
Fig. 5.3: Output characteristics of an AlGaN/GaN sensor in pH 7 and different reference voltages. For comparison, the characteristics in air and at pH7 without reference electrode are shown.

All these measurements are performed at constant temperature in sequence without electrolyte mixing or other changes of the setup. For the output characteristics $I_D(U_{DS})$, U_{DS} was varied from $0\ldots1.5$ V and U_{ref} from $-1\ldots+1$ V. If a negative gate – source voltage is applied, the 2DEG is depleted and negligible small current is flowing in the channel. With increasing gate potential, especially in the positive range, higher drain – source voltages are needed to bring the transistor into saturation regime. Remarkably, if no stabilized reference potential is applied, the signal is drifting very strong (Fig. 5.3). These measurements underline the importance of the reference electrode in fluidic applications. Moreover, the measurements accomplished in air without gate – source potential show ideal Ohmic characteristics of the transistor contacts. The resistance it is found to be about 500 Ω. This resistance it is the result of the serial connection of contacts, the wire resistance, the passivation resistance, the Ohmic contact resistance, and the channel resistance. The channel resistance can be related to the technological and geometric sensor parameters as:

$$R = \rho \frac{L}{Wd} = \frac{1}{e n_s \mu} \frac{L}{W}, \tag{5.22}$$

85

where W and L are the channel width and length, respectively, d is the channel thickness, n_s and μ are the electron concentration and mobility in the 2DEG, respectively. Using the parameters from table 4.2 ($n_s = 6.41*10^{12}$ cm^{-2} and $\mu = 798$ cm²/Vs) and the gate dimensions ($L = 500$ µm and $W = 2400$ µm), a channel resistance value of 255 Ω is obtained.

Fig. 5.4a shows transfer characteristics $I_D(U_{ref})$ for $U_{ref} = -2\ldots2$ V at constant U_{DS} from $0.1\ldots1$ V. The characteristics for $U_{DS} = 0.5$ V have been recorded using two different reference electrodes. The transfer characteristic of the classical glass reference electrode is shifted about $U_{ref} \sim 53$ mV to negative vakues compared to the characteristics using a self made reference electrode. This difference is caused by differences in the electrochemical potential between the reference electrodes (see chapter 5.3.4).

In addition to the transfer and output characteristics, the dynamic properties of the transistor are important. For a standard source circuit, small signal parameters can be determined by partial differentiation:

$$g_m = \left.\frac{\delta I_D}{\delta U_{ref}}\right|_{U_{DS}=cons\tan t}. \tag{5.23}$$

For an ideal transistor, the transconductance g_m is only dependent on the barrier thickness, the channel dimension length L and width W, and on the channel carrier mobility μ. In the linear region, which is shown in the Fig. 5.3 within the range of U_{DS} between 0 and ~0.5 V, the transconductance is independent on the drain-source current I_D with:

$$g_m = \mu \frac{\varepsilon}{d} \frac{W}{L} U_{DS} \tag{5.24}$$

In the saturation region the transconductance is dependent on the square route of I_D:

$$g_m = \frac{\sqrt{2\mu\varepsilon I_D}}{Wd} \tag{5.25}$$

The transfer characteristics (Equation 5.23) of the sensor and the calculated transconductance are shown in Fig. 5.4a and b, respectively. The transistor has a threshold of $U_{th} = -1.2$ V. The maximum transconductance, which is marked in Fig. 3.4b for different drain-source voltages, represents the maximum slope in the transfer characteristics in Fig. 3.4a.

This maximum change of the drain current upon variation of U_{ref} coincidences with the maximum sensitivity of the ISFET device and is usually selected as the working point. In the present case, $U_{DS} = 0.5$ V is chosen due to an optimal signal-to-noise ratio (see chapter 5.3.4) and the working point is at $U_{ref} = -0.35$ V with $g_m = 0.756$ mS.
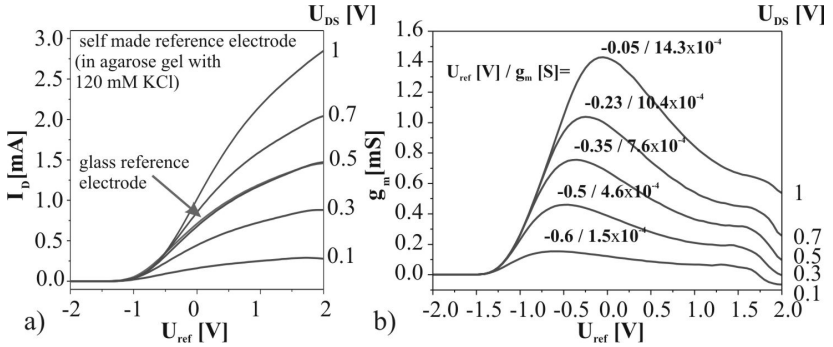

Fig. 5.4: a) Transfer characteristics of a PIMBE grown sensor in pH 7 and b) calculated transconductance. In (b) the maximum transconductance and the corresponding U_{ref} of the working point is given.

The transistor characteristics were analyzed in more detail in dependence on the *W/L* ratio, which is an important value that determines parameters such as the transconductance and, thus, also the sensor sensitivity. In Fig. 5.5, both the drain-source distance and the length of the active area were taken into account. The length of the active area is shorter due to the overlap of the passivation of the contact with the metallization free area between the contacts. The overlap was 5, 15 and 50 µm for the MOCVD samples with smallest active area length of 35 µm, the other MOCVD samples and the larger PIMBE samples, respectively (Table 5.3). While the sensing properties are determined by the active area length L_{act}, while the drain-source distance L_{real} is important for the transistor characterization. Since the measurements have been performed in solution, which is in contact only with the active area, both calculations are shown to demonstrate that the way of calculation has minor influence on the MOCVD grown samples, while it strongly effects the extracted parameters of the PIMBE samples.
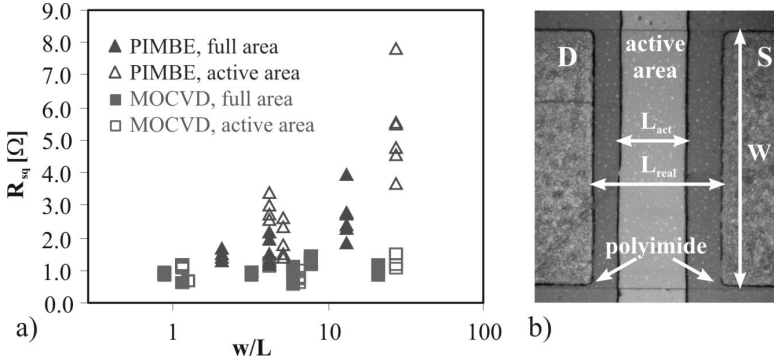
Fig. 5.5: a) Sheet resistance of different sensors vs. w/L ratio for MOCVD or PIMBE grown transistors. The calculation was performed using the drain-source distance L_{real} (full area) or the width of the active area L_{act} (active area). b) Geometry of the sensor for explanation.

Table 5.3: Sensor geometries used in this work (see annex 4).

PIMBE

W [µm]	L_{act} [µm]	L_{real} [µm]	W/L_{act}	W/L_{real}
400	100	200	4	2
2400	100	200	24	12
2400	500	600	4.8	4

MOCVD

W [µm]	L_{act} [µm]	L_{real} [µm]	W/L_{act}	W/L_{real}
40	35	45	1.14	0.89
250	35	45	7.14	5.56
400	100	130	4	3.08
500	400	430	1.25	1.16
2400	100	130	24	18.5
2400	400	430	6	5.58

The MOCVD grown sensors exhibit generally a lower sheet resistance as expected from the electrical characterization (see chapter 4.2) and show also substantially smaller scattering of the properties from sensor to sensor than the PIMBE grown samples. This is mainly due to the higher annealing temperatures for the contacts and the better material properties in MOCVD grown heterostructures. With increasing of W/L value also the resistance is increasing because of higher serial resistors on the chip. Since for all sensors the same chip size was used, transistors with smaller gate lengths required longer contact lines to the bonding pads (see sensor layout in the Appendix) and therefore have a higher serial resistance. The high resistance is the result of the curing of polyimide at 350°C which degrades the electrical properties of the gold lines; however, the underlying mechanisms of this degradation were not investigated further.

As a consequence, also the transconductance is affected by these serial resistors and exhibits strong dependence on the W/L ratio (Fig. 5.6). The expected linear dependence is present only for $W/L < 10$, for higher values a deviation is observed, especially for PIMBE grown sensors.
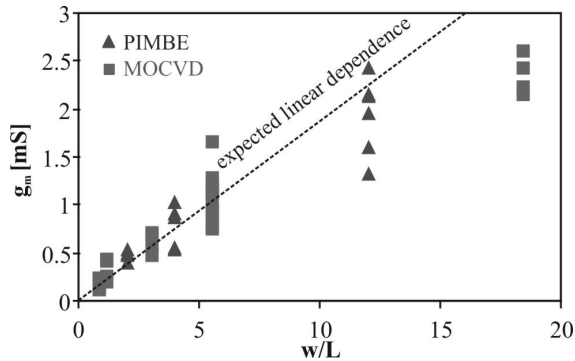
Fig. 5.6: The transconductance calculated from the transfer characteristics of different sensors (PIMBE and MOCVD) at traced in MT pH7 buffer solution using leak free reference electrode and $U_{DS} = 0.5$ V.

5.3.2. Sensors sensitivity

A very important parameter for the characterization of AlGaN/GaN ISFETs is its sensitivity to the pH value. As shown in introduction, GaN based pH sensors were already realized and the high sensitivity to hydronium ions were proofed [41, 42, 112].

According to these results, the sensitivity of the sensors can be defined as the variation of the surface potential Ψ_0 in dependence on the concentration of hydronium ions in the electrolyte:

$$S = \frac{\Delta\Psi_0}{\Delta c_{H_3O^+}} \cdot \qquad\qquad (5.26)$$

To be able to determine the pH sensitivity, it is necessary to measure its transfer characteristic I_D versus U_{ref} for at least two different calibration buffer solutions with known pH. In Fig. 5.7, the transfer characteristics in three buffer solutions (pH 4, 7, 10) of a sensor with an active area 2400 x 500 µm² are shown. Here, the transfer characteristics is recorded by a modulation of the drain-source current I_D as a function of the open gate potential, which in the case of ISFET sensors is defined by the reference electrode, while the source contact is on ground potential. Thus, $U_{GS} = U_{ref}$, and the concentration of ions defines the surface potential Ψ_0 (see Fig. 3.6).

If the reference voltage is kept constant and the ion concentration in the buffer solution is changed, than the surface potential is changing and as already explained (see chapter 3.2). This modulates the sheet carrier concentration and thus, the current I_D. The surface potential is equivalent to a series voltage to the reference voltage and therefore, with every change of the surface potential also the transfer characteristic is shifted parallel to U_{ref} axes to more negative gate-source potential for a positive charge and to less negative potential for a negative charge. In this case the pH sensitivity of the sensor can be written as:

$$S_{pH} = \frac{\Delta U_{ref}}{\Delta pH}, \qquad\qquad (5.27)$$

where ΔU_{ref} is the difference in reference potential for two buffer solution with different pH. The determination of this shift at a given drain current is called constant current mode.

If the current change upon pH value is determined at a fixed reference voltage (constant voltage mode) the sensitivity can be written as:

$$S_{I,pH} = \frac{\Delta I_D}{\Delta pH} \approx g_m \frac{\Delta U_{ref}}{\Delta pH}, \qquad\qquad (5.28)$$

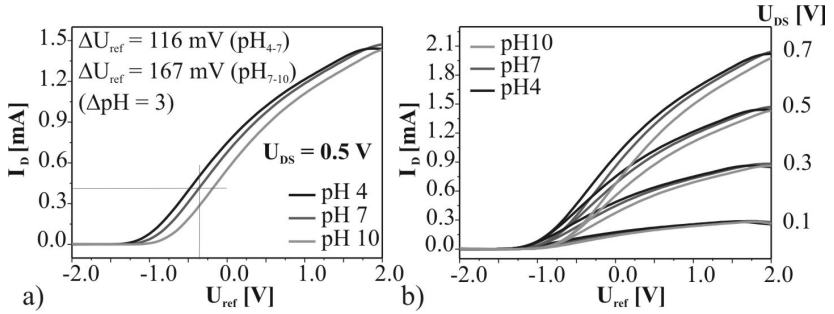where g_m is the transconductance calculated as explained in the previous chapter.

Fig. 5.7: Transfer characteristics of an AlGaN/GaN ISFET (PIMBE) sensor a) for three solutions with different pH values, and b) for different fixed reference voltages.

Using these equations, the sensitivity of the sensor, which transfer characteristics are shown in Fig. 5.7, is calculated. For the pH range from 4 to 7 a sensitivity $S_{pH} = 38.8$ mV/pH or $S_{I,pH} = 28.1$ μA/pH and for the range pH 7 to 10, $S_{pH} = 58.5$ mV/pH or $S_{I,pH} = 46.1$ μA/pH is determined. The values in alkaline solutions are in good agreement with the 59 mV/pH from the theoretic approximation using Nernst equation (see chapter 3.2.3.). All measurements were done at room temperature. For the same sensor the sensitivity was also determined for different U_{DS} (Fig. 5.7b). A summary of the determined sensitivities is given in Fig. 5.8.

Obviously, for this sensor the sensitivity in acidic solutions is lower than in the alkaline region. It is an extreme example, where acidic and alkaline solutions cause strongly different sensitivities. For these differences, no systematic dependence on the sample geometry was found, however, the behavior in Fig. 5.8 is inverted for MOCVD grown samples, i.e., they have higher sensitivities in acidic than in the alkaline solutions. Possible originating surface effects, which could be responsible for these effects are discussed in more detail in the next chapter. It should be mentioned that MOCVD and PIMBE grown samples have different carrier densities in the confined 2DEG, and the corresponding field in the barrier layer may affect the surface potential and, thus, the charge equilibrium. This effect requires further simulation and is taken into account in this work. Averaging the sensor response over all heterostructures and used geometry, a mean sensitivity of 52 mV/pH and 46 mV/pH was obtained for PIMBE and MOCVD grown sensors, respectively.
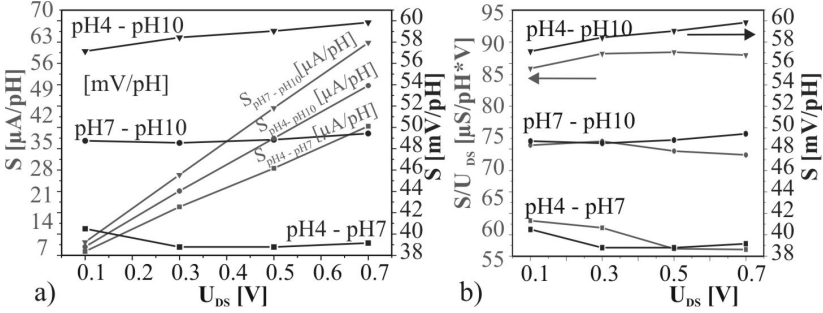
Fig. 5.8: Sensitivities S_{pH} in mV/pH and $S_{I,pH}$ in µA/pH at different U_{DS} for a PIMBE grown sensor with active area of $L = 500$ µm and $W = 2400$ µm.

The general trend of increased sensitivity in constant voltage operation (Fig. 5.8a) with increasing U_{DS} is caused by Ohmic behavior of the 2DEG channel. Dividing the sensitivity in µA/pH by the respective drain-source voltage, also a relative linearity is obtained (Fig. 5.8b).

A determination of sensitivity for PIMBE and MOCVD sensors with different W/L characteristics and different barrier thickness is also illustrated in Fig. 5.9. Because the sensitivity depends on the surface properties as will be shown later, it is necessary to make for every sensor a calibration in known pH solutions before to use this sensor for unknown pH determination. After calibration the determination of unknown pH values of different solutions can be performed. The transfer characteristics are recorded and after that the pH_x can be calculated using the equation:

$$pH_x = pH_1 + \frac{U_{ref,x}\left(I_D^*\right) - U_{ref,1}\left(I_D^*\right)}{S_{pH}}, \tag{5.29}$$

where U_{ref1} is the potential, at which the transconductance reaches its maximum (maximal linearity) for a known pH_1 buffer solution, and U_{refx} is the potential for the transfer characteristics in the solution with pH_x that shall be determined. I_D^* has a constant value, which is derived from the sensor working point as explained in the next chapter.

The sensitivity of several PIMBE and MOCVD sensors is calculated and presented as function of the W/L ratio in Fig. 5.9. Obviously, the sensitivity S [µA/pH] follows the trend of the transconductance (Fig 5.6).
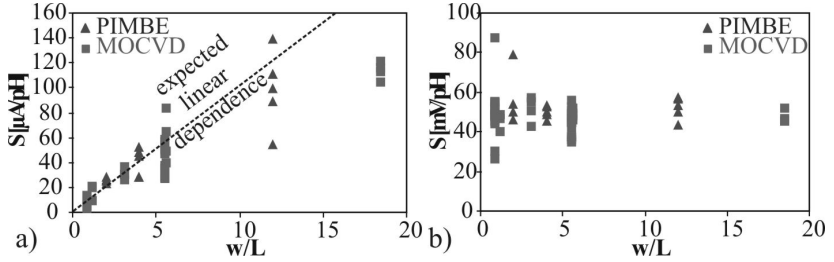
Fig. 5.9: Sensitivity $S_{I,pH}$ (a) and S_{pH} (b) versus W/L of sensors from PIMBE and MOCVD grown heterostructures with different barrier thicknesses.

It increases linearly with small W/L ratios and shows strong deviations for larger $W/L > 10$. In the linear region, the current I_D shows the expected proportional dependence on W/L [145]. As in case of the transconductance and due to the same technological factors, the sensitivity is nonlinear in case of long active areas. This behavior is mainly present in PIMBE sensors.

As mentioned before, the mean sensitivity of PIMBE grown sensors is closer to the Nernst law. One of the main reasons might be the strong light sensitivity of MOCVD grown sensors [42, 140], which also causes strong scattering of the sensitivities from sensor to sensor seen in Fig. 5.9. One of the most important outcomes of these investigations is that the sensor characteristics are most stable in constant current mode for high W/L ratios, where also MOCVD grown samples exhibit sensitivities $S > 50$ mV/pH. However, since at the time of this investigations the MOCVD grown samples exhibited a strong light sensitivity, for the cell transistor coupling measurements the PIMBE sensors were use and a signal characterization as function of multiple noise sources is presented in the next part.

5.3.3. Working point

The working point of the AlGaN/GaN ISFET defines its sensitivity and is very important for further characterization. To choose the working point of a transistor, first of all its transfer characteristic in a known pH buffer solution has to be recorded. In both modes (constant current or voltage) a constant value of U_{DS} must be determined. Large values of U_{DS} lead also to high g_m (see Fig. 5.4) however; increasing U_{DS} enlarges also the potential difference to the reference electrode, which can cause unwanted parasitic effects such as leakage currents and passivation damage.
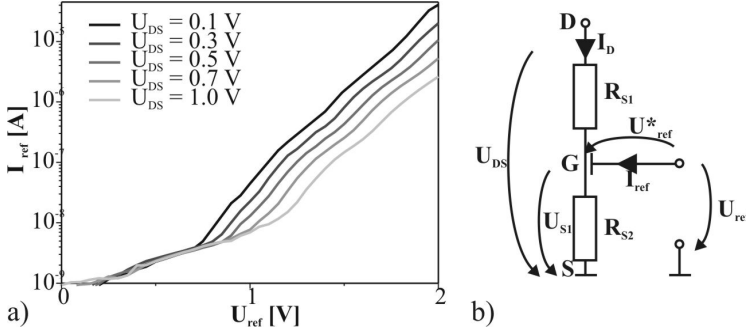
Fig. 5.10: a) Leakage current of the reference electrode I_{ref} versus U_{ref} for different U_{DS}. b) Equivalent circuit for the explanation of the leakage current.

For positive U_{ref}, the AlGaN/GaN heterostructures shows forward characteristics of a diode (Fig. 5.10a), which results in an increased leakage current I_{ref} from the reference electrode to the gate. This current additionally depends on the voltage U_{DS}. With increasing of U_{DS}, the current is decreasing. These can be explained by a voltage drop U_{S1} on a serial resistance R_{S1} (Fig. 5.10b). As a consequence, the effective reference voltage to the gate U^*_{ref}, which finally defines the operational point, is smaller than the externally applied reference voltage U_{ref} ($U^*_{ref} = U_{ref} - U_{S1}$) and thus, depends on U_{DS}:

$$U^*_{ref} = U_{ref} - U_{DS} \frac{R_{S2}}{R_{S1} + R_{S2}}. \tag{5.30}$$

This effect needs to be considered for the selection of the working point. The origin of the serial resistance can be the metallization as well as the part of the active area, which is covered by the passivation and therefore is unaffected by the electrolyte.

For most of the measurements $U_{DS} = 0.5$ V was chosen. In this case, U_{ref} is ~ -1 to 0 V for PIMBE grown sensors and the corresponding leakage current I_{ref} to the gate at the working point is in the pA region. As shown above, by differentiation of the transfer characteristics U_{ref} is obtained, where the transconductance reaches its maximum. At this working point the transfer characteristics are approximately linear and the sensor has its maximum sensitivity (Fig. 5.11).
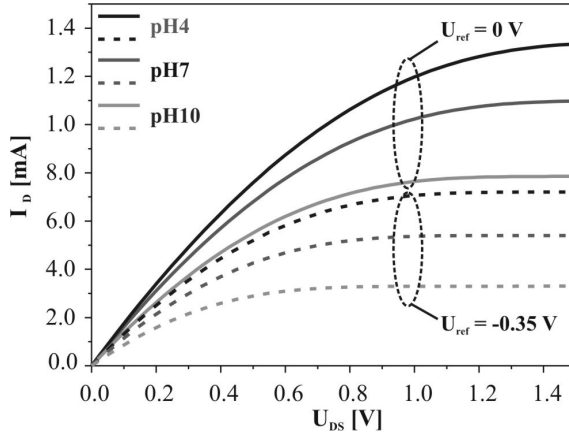
Fig. 5.11: Sensor output characteristics I_D vs. U_{DS} for two different reference potentials. At -0.35 V the transconductance has its maximum and the sensor its maximum sensitivity at $U_{DS} = 0.5$ V.

In constant current mode, the reference voltage is modulated to keep the drain-source current constant. This alteration in U_{ref} is equivalent to the changes of the surface potential in dependence on the chemical environment in the electrolyte. In constant voltage mode, U_{DS} and U_{ref} are kept constant and the variation in I_D is measured.

In this work, the constant current method was chosen for the cell-transistor coupling experiments in order to avoid the influence of variable surface potential to the adherent cells.

5.3.4. Noise and drift

In the measurement setup as described before, several source of noise appear. External noise sources (thermal, electronic, light) are discussed and quantified elsewhere [112]. Noise originating from the heterostructure and its interaction with the electrolyte has a level of about 100 nA. In the case of cell measurements, additional noise caused by the biochemical processes appears which can decrease or increase the overall noise level: decreasing due to the stabilization of the surface chemistry, and increasing if the additional source is stronger. The stabilization effect is caused, because the cells need some couple of days to proliferate on the active area. At the end, the noise level is decreased to 20 – 50 nA.
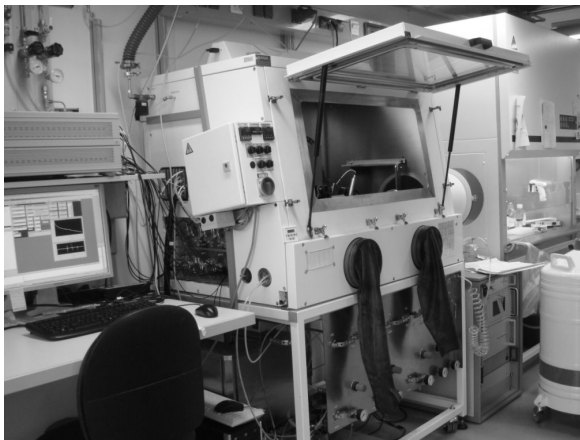
Fig. 5.12: The measurement setup used to record the sensor signal (glove box with sample loading from a laminar box (right) and the PC for monitoring the signals (left)).

In any case these values of noise are acceptable, if we take in consideration that the sensor response to extracellular potential is between 1 and 15 μA. For minimization of the external source it is recommended to perform the measurements in an electrically well isolated box. For the transistor-cell coupling experiments in this work, a glove box is used (Fig. 5.12), which provides also special conditions for the measurements such as constant temperature, humidity, pressure and atmosphere composition. In this glove box, also the light sensitivity of the sensors can be controlled by running the measurements in constant light flux [42].

For the recording of the electrical signals, a "Source-Measurement-Unit" from Agilent is used. It ensures stable potential and good cable isolation against electrical noise. To control this system, a computer and a program in LabView is used [146].

In addition to the noise, a signal drift appears during the measurements, which is a common problem for all chemical sensors. To control the magnitude of drift, the sources of it have to be identified. First, the drift influence from the reference electrode is studied by recording the difference in potential for the three simultaneously used reference electrodes (Fig. 5.13).
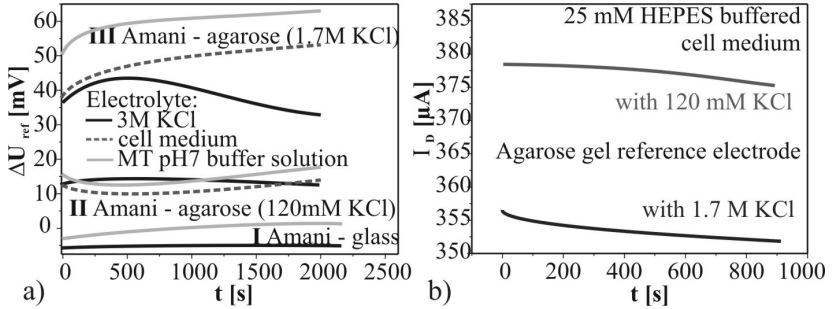
Fig. 5.13: a) Differences in U_{ref} for three pairs of reference electrodes in three different electrolytes: pair I: MT glass electrode against Amani reference electrode, pair II: Amani reference electrode against agarose gel electrode with 120mM KCl, pair III: Amani reference electrode against agarose gel electrode with 1.7M KCl. b) Sensor signal using two different type of agarose gel solutions.

Three different electrolyte solutions were used for characterization: 3M KCl, buffered cell medium with a constant pH 7.5, and MT pH 7 buffer solutions. The 3M KCl solution is identical to electrolyte inside of the glass and Amani reference electrodes. The potential difference between the two electrodes was found to be stable about -5 mV for more than 2000 s, which corresponds to an offset of ~pH 0.1. Theoretically, the potential difference has to be close to zero, however, the two electrodes are quite different in the construction and this causing the observed potential difference.

In case of Amani electrode against agarose gel electrodes in 3M KCl solution, the signal is not stable and a drift of about 10 mV is observed for small concentrated agarose gel. The drift is the result of the smaller KCl concentration in the agarose gel compared to the electrolyte and the potential difference is decreasing in time due to diffusion of ions from high concentrated solution into the agarose gel. As smaller the concentration in the agarose gel as larger is this drift. This effect is obvious comparing the differences of the reference potential $\Delta U_{ref} \sim$ 10-20 mV for agarose gel with 1.7 M KCl and $\Delta U_{ref} \sim$ 35-55 mV for 120 mM KCl. In buffered cell medium and MT pH 7 solutions, the difference in potential is increasing in time due to the diffusion of Cl⁻ ions into the KCl-free electrolyte. It has to be noted that for the differently concentrated agarose gels, the slope of the recorded curves is the same.

A potential difference of about 60 mV is found for the Amani reference electrode against 120 mM KCl agarose gel reference electrode in MT pH 7 buffer solution, which is in perfect agreement with the difference of 53 mV found in transfer characteristics of a sensor comparing two difference reference electrodes: the agarose gel reference electrode and glass electrode (see chapter 5.3.1.).

The shift of about 30 mV between the potential differences between the Amani and the two different concentrated agarose gel reference electrodes as well as the changing behavior in dependence on the environment clearly demonstrate that the miniaturized self made agarose gel electrode is not suitable for quantitative determination of the pH value in an unknown solution. However, these large differences influence not critically the sensor signal (Fig. 5.13b). Thus, the electrode can be used for relative measurements of changes in an electrolyte or for quantitative measurements after calibration prior to the experiments. In this work, these 120 mM KCl agarose gel reference electrode was used for the transistor-cell coupling experiments because of its low concentration of Cl^- and K^+ ions, which prevents the out-diffusion into the cell medium and its impact on the cells experiments.

Another major factor that can influence the sensor signal and create drift is the sensor contact passivation. As already shown (chapter 4.1.2.4), polyimide was used for this purpose due to its excellent chemical stability [134]. To proof its stability in electrolytes, the sensor signal I_D vs. time was recorded for a PIMBE and MOCVD grown sensors with 1.5 µm thick polyimide on the active area (Fig. 5.14).
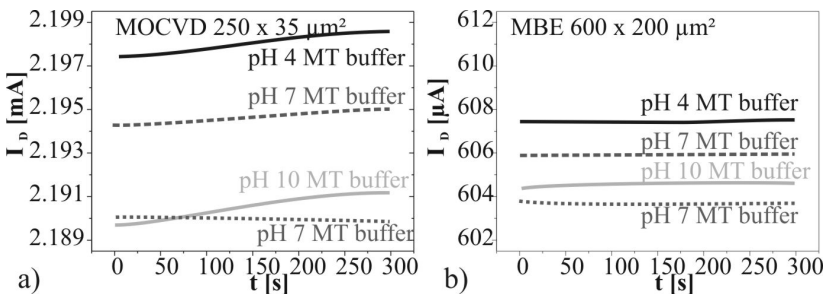

Fig. 5.14: Sensor signal for (a) MOCVD and (b) MBE grown sensors with the active area completely covered by polyimide in different MT buffers.

Standard MT buffer solutions with three different pH values (4, 7 and 10) served as electrolyte and a glass electrode as reference. The signal was stable all over the recorded time. For comparison, another sensor from the same chip with an open active area was measured at the same conditions. The noise was about 160 nA and 550 nA in case of MBE and MOCVD grown sample, respectively. The measurements are summarized in table 5.4.

Table 5.4: Summary of drift experiments for PIMBE and MOCVD sensors with (index "p") and without (index "o") polyimide passivated active area.

Sensor		PIMBE	MOCVD
AlGaN barrier	[nm]	13	15
Active area	[μm^2]	600 x 200	250 x 35
S_o	[mV/pH]	58.2	71.7
	[μA/pH]	27	63.7
S_p	[μA/pH]	0.5	7.3
S_p/S_o	[%]	1.85	11.4
$I_{D,o}$ at pH4	[μA]	310	804
$I_{D,p}$ at pH4	[μA]	607	2200
$g_{m,o}$	[mS]	0.45	0.92
U_{ref}	[V]	-0.5	-2.5
U_{DS}	[V]	0.5	0.5
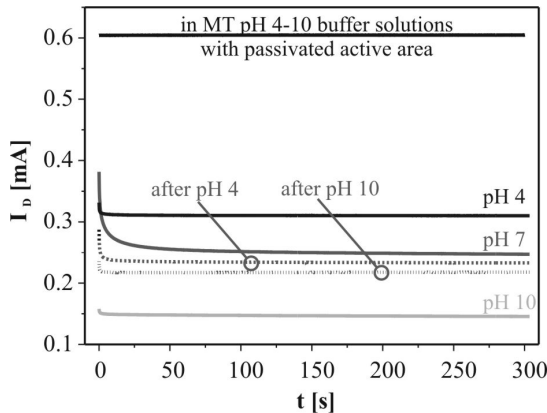
Fig. 5.15: The recorded sensors signal from subsequent measurements with the PIMBE sensor in pH 7 / 4 / 7 / 10 / 7 and comparison to the signals in the same electrolytes using a completely passivated sensor (upper curves).

Both types of sensors are affected by the electrolyte even if the active area is completely covered by the passivation. This phenomenon can be caused by moisture uptake of the polyimide or by selective ion diffusion through the passivation. Table 5.4 shows that the influence on the 2DEG channel in a PIMBE sensor is lower (1.85%) than for an MOCVD sensor (11.4%). The origin of this difference was not further investigated. It can be due different roughness or chemical composition of the sensor surface in dependence on the growth method. It also has to be noted that the used MOCVD grown sensor exhibit a strong non-Nernstian behavior, which could be amplify the observed parasitic effects.

It is known that the group III nitrides can be etched in alkaline media. A pH of 10 represents a strong alkaline electrolyte and during the measurement, the (Al)GaN surface or the thin surface oxide layer degrades and the sensor signal is decreasing. After the surface cleaning in deionized water and drying in nitrogen flux, the surface is not completely recovered and for this reason, subsequent measurements at pH 7 yield a smaller current (Fig. 5.15). Also this phenomenon was observed to be smaller in case of the PIMBE grown sensor.

The mentioned 1.85% shift from the polyimide passivation has a relative small influence on the sensor signal that can be observed in the beginning of the measurements and described as a memory effect (see figure 5.15). After the first 50 s, the passivation is stable but up to this time other factors contribute to the signal drift. The same measurements were repeated for a passivated sensor with a thick polyimide layer of about 2.5 µm. In the case of the sensor with completely passivated active area, the noise and the reference current was found to be in µA region, which is a very high value. Also on the sensor with open active area similar drifts were observed and the recording of current in time was practical impossible due to high signal instability. Thus, the use of a thick passivation layer is not recommended.

For cell-transistor coupling experiments, the drift in sensors with thin layer polyimide passivation is negligible because of the long proliferation time, which the cells need to cover all the active area (see chapters 6 and 7) and because of the small changes in the cell and cell medium composition, (i.e., $\Delta pH \sim 0.5$) during the experiments. In any case, the PIMBE grown sensors were used for the cell–sensor coupling experiments. For this reason the influence of different electrolyte solutions to the PIMBE sensors signals was further studied.

For these experiments, a couple of sensors with different active areas provided from the same wafer were used. The PIMBE grown heterostructure with an AlGaN barrier thickness of 13 nm is the base for the analyzed sensors. The transfer characteristics were recorded three times successively in neutral (MT pH 7) and acidic (MT pH 4) electrolyte solutions, followed by the same sequence for neutral (MT pH 7) and alkaline medium (MT pH 10). For extracellular recording of cell potential, it is important to evaluate the sensor drift at small pH changes in alkaline electrolytes, which was performed in phosphate buffer solutions with pH 7 and pH 8. In every measurement, the value of I_D is decreasing, which leads to the shift of transfer characteristics to a smaller surface potential. This shift was taken into account by using the first measurement as a reference for every sensor (i.e. the recorded transfer characteristic in neutral pH 7 buffer solutions).

The measurements results are presented in Fig. 5.16a, where the measured voltage difference ΔU_{ref} for every measurement performed in the described sequence to the starting value is plotted. The largest shift is observed for sensors with narrow active area, i.e. small L (dark squares). For the successive measurements switching only between acidic (alkaline) to neutral electrolytes (i.e. pH 7/4/7/4… or 7/10/7/10…, squares in Fig. 5.16a), a stabilization of the sensor signal can be observed after 2-3 cycles. In contrast, for the sequence of Fig. 5.15 (7/4/7/10/7/4/7/10…, triangles in Fig. 5.16a), a remarkable stronger scattering of the data and no signal stabilization can be observed.
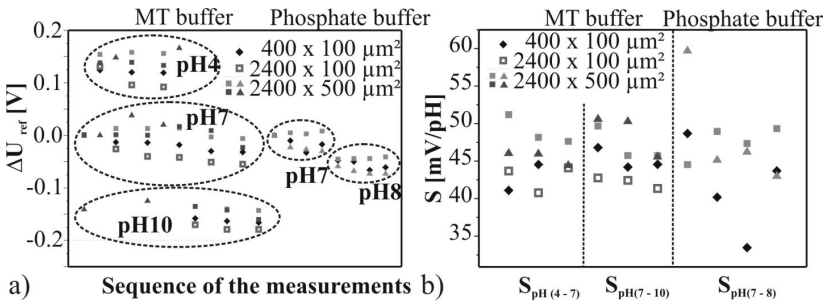

Figure 5.16: The shift of the transfer characteristics (a) and the change of sensors sensitivity (b) after successive measurements in different pH solutions.

Finally, the measurements in phosphate buffer solutions, which covered a pH change between 7 and 8 only (Fig. 5.16a, right side), also revealed a shift in the transfer characteristics and stabilization after a few cycles. Similar to the experiments in MT solutions, the drift is higher for sensors with small active area (dark squares). Remarkably, also for sensors with larger active area the drift is high, when the sensor was not in use before the experiments, which underlines the importance to consider a stabilization time for the sensor prior to quantitative measurements

The calculation of the sensors sensitivity after every couple of measurements (Fig. 5.16b) demonstrates that after the first two measurement cycles the sensitivity is becoming relative constant and the standard deviation was found to be below 10%. For the sensors with small active area, memory effects seem to play an important role in amplifying the drift effect at least in phosphate buffer solution. The deviation of the transfer characteristics in neutral MT buffer solution is summarized in Fig. 5.17. Again, the biggest shift is present in case of small active area sensors.

The above discussed measurements have been performed in the constant current mode. The same shift is present also in the case of constant voltage mode, i.e. the recording of the drain source current versus time (Fig. 5.18a). Here, the sensor with the large active area (2400 x 500 µm²) was used. The reference voltage was kept constant at a value of -0.35 V, which represents the point of maximal transconductance for this device at a drain-source voltage of 0.5 V.
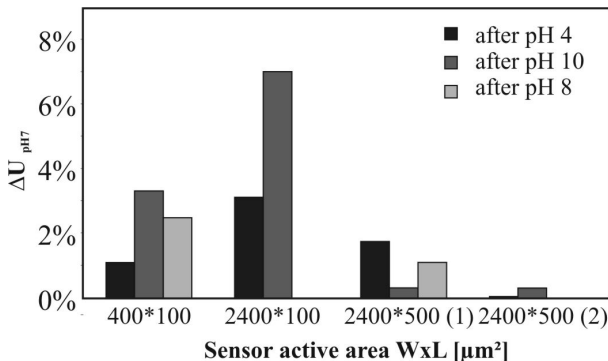

Fig. 5.17: Relative shift of the transfer characteristics for the successive measurements in different pH solutions from Fig. 5.16

As expected, similar to the observed shift of the transfer characteristics to smaller voltages, also the measured drain–source current decreases in time (Fig. 5.18b). If the working point it is changed to another drain–source voltages, the drift in time is decreasing with the applied voltage (Fig. 5.18b). In the same time, also the current value is decreasing (Fig. 5.18a) leading to a decreased sensitivity (see chapter 5.3.3). The normalized drain-source currents versus time are compared in Fig. 5.18b. It is obvious that the sensor signal drifts stronger in acidic or alkaline buffer solutions. After about 400 s the sensor signal stabilizes. The reaction of the sensor in neutral MT pH 7 buffer solutions depends on the previous experiment. After measurements in acid solutions, the drift is almost the same and the sensor signal is shifted to smaller current values. In contrast, for measurements after exposure to alkaline solutions, the current value is increasing in time and tends to approach the same value as during the first measurement in neutral buffer solution. Obviously, the subsequent exposure to acidic and alkaline solution can partly neutralize the drift. Consequently, the drift and memory effects in the sensors are strongly related to diffusion of ions, most probably hydrogen and alkaline metals in the passivation.
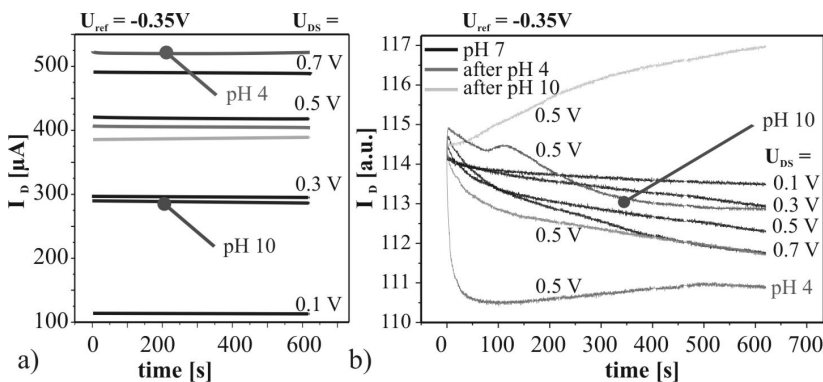

Fig. 5.18: (a) Sensor drift $I_D(t)$ in different pH buffer solutions and for different drain source voltages. (b) Normalized sensor drift $I_D(t)$.

In summary, all the sensors exhibit a strong drift independent of the measurement conditions, which complicates quantitative measurements.

However, for the study of cell reaction to different inhibitors the signal changes are expected to be small and the long preparation periods necessary for the proliferation of cells ensures a stabilization of the sensor signal as far as possible. Moreover, most of the drift can be neglected due to the fast response of cells. Consequently, even if quantitative pH sensing cannot be assured, the cell-transistor coupling can be studied. In addition, drift was found to be more pronounced for MOCVD grown sensors and for small active areas. It should be noted here that for previously published coupling experiments of AlGaN/GaN transistors with cardiac myocyte syncytium, MOCVD grown transistor arrays with small active area have been used [19]. Such smaller transistors have a high potential for spatially resolved analysis. The origin of the poor properties of the MOCVD grown and the small area transistors in this work might have technological reasons; however, these effects were not further investigated. For this reason, the cell-transistor coupling experiments, which are described in chapter 7, were performed using sensors with large active area. Before such experiments can be performed it is necessary to know the biocompatibility of the sensor surface and the influence of different treatments on the proliferation of cells. This topic will be discussed in detail in the next chapter.

6. AlGaN/GaN based biosensors

6.1. Functionalization of sensor surface.

With the mechanisms described in the precedent chapters and the excellent stability, group III nitrides bear a high potential for biosensing applications. Fig. 6.1 illustrates how the basic AlGaN/GaN heterostructure can be employed for sensing applications and which kind of surface functionalization can be used. The different approaches to facilitate the connection of the biological recognition system to the transducer element, i.e. the AlGaN/GaN ISFET, are described in the following section. The oxidation of the GaN surface, the coating with ion selective membranes and finally the attachment of biomolecules to the surface are presented by means of the results published in recent years. An overview of the different functionalization steps is given in table 6.1.
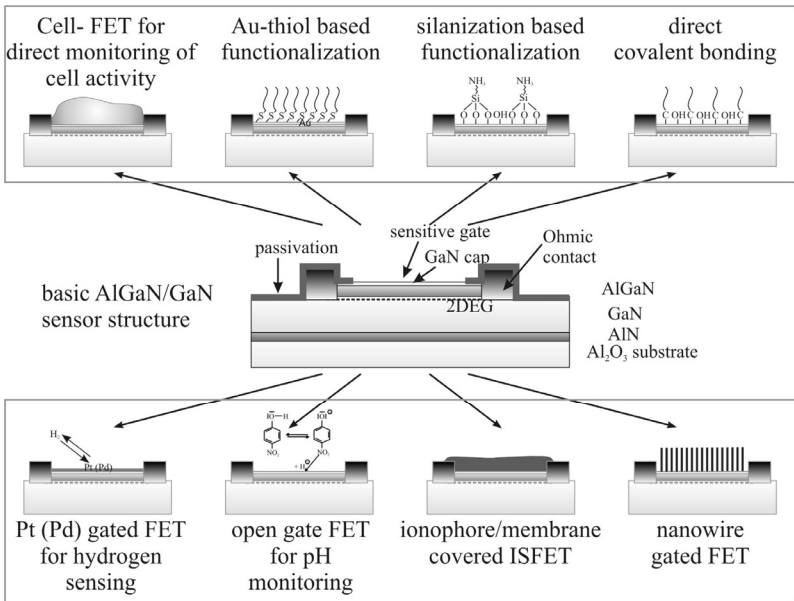
Fig 6.1: Schematic overview illustrating the surface functionalization and possible applications of the AlGaN/GaN heterostructure for biosensors (up) and (bio-) chemical sensors (down) [147, 148].

Tab. 6.1: Reported functionalization methods of AlGaN/GaN surfaces to realize selective Bio-FETs.

detection	surface cleaning	surface functionalization	measurement setup	Ref.
ion selective membranes				
halide ions (F-, Cl-) DNA	water	Au (20 nm) gated device + thiol SH-C$_{18}$	$I_D(U_{DS})$ curves, 25°C, dc and ac measurements.	[98]
Hg^{2+}	oxygen plasma	Au (20 nm) gated device + thiol SH-C$_{18}$	see above	[149]
cations K$^+$	not specified	ionophore doped PVC: 1% K-ionophore I, 33% PVC, 66% bis-2-ethylhexyl)-sebacate as plasticizer	I_D (concentration), $U_{GS} = 0$, Ag/AgCl reference	[113]
Biomolecules				
-	N$^+$ sputtering, annealing 900°C	aniline (C$_6$H$_5$NH$_2$) degassed by repeated freeze – pump – thaw cycles, with freezing at dry – ice temperature	-	[150]
-	see above	3-pyrroline (C$_4$H$_6$NH) – addition of isolated C=C units on Ga – polar GaN	-	[151]
-	Piranha H$_2$SO$_4$ / H$_2$O$_2$ + water	MPTMS monolayer (evaporation) followed by ultrasonic rinsing in xylene	-	[152]
-	Piranha H$_2$SO$_4$ / H$_2$O$_2$	incubation in 1% APTMS solution, ethanol rinsing, exposing to glutaraldehyde (2 h), rinsing with water, exposing to 3 μM amine-terminated ssDNA (1 h) in 750 mM KCl	-	[153, 154]

detection	surface cleaning	surface functionalization	measurement setup	Ref.
-	H_2SO_4/30% H_2O_2 + water, dried in N_2 + UV, 3 h	GaN(0001) surfaces exposed to a hydrogen plasma react with organic molecules bearing an alkene (C=C) group when illuminated with 254 nm light.	-	[155, 156]
botulinum toxin	oxygen plasma	Au (20 nm) gated device + thiol SH-C_{18}	$I_D(U_{DS})$ curves, 25°C, dc and ac meas.	[157]
proteins	water	amine groups by treating with 1% APS (3-aminopropyl triethoxysilane), n-hydroxysulfosuccinimidobiotin (sulfo- NHS-biotin) to immobilize biotin, blocked with 1% BSA to avoid nonspecific binding of nanoparticles	$I_D(U_{DS})$ curves, 25°C	[120]
-	Piranha H_2SO_4:/ H_2O_2	ODTMS (5% in toluene / 0.5% butylamine catalyst) APTES (20 mM in toluene), Schiff-base formation (20 mM glutaraldehyde), 20-mer 5' amino-modified oligonucleotides, in phosphate buffered saline (PBS) (immobilization of DNA)		[158]
enzyme: penicillinase	Piranha H_2SO_4:/ H_2O_2	Schiff-base formation, covalent immobilization of penicillinase from bacillus cereus (see above), coupling of cross – linker and enzymes in presence of sodium cyanoborohydride (NaCNBH$_3$)	ΔU_{GS}, U_{DS}, I_D = const, Ag/AgCl reference	[122]

detection	surface cleaning	surface functionalization	measurement setup	Ref.
DNA	-	Au gated FET, label-free 3'-thiol-modified oligonucleotides (binding layer for hybridization of matched target DNA	$I_D(U_{DS})$ curves, 25°C ac operation to prevent electrochemical side reactions, 500 mV bias at 11 Hz.	[121]
PSA	UV light for 3 min	Au gated FET, binding of thioglycolic acid to Au by submerging in 1 mM thioglycolic acid COOH groups for chemical linking of PSA monoclonal antibody	see above	[158]
glucose	water	dipping HEMT coated with ZnO nanocrystals in aqueous solution of 20 mM $Zn(NO_3)_2 \cdot 6H_2O$ + 20 mM $C_6H_{12}N_4$ to grow ZnO nanorods; expose to 5 μl GO_x; keep 48 h at 4 °C; extensively washing to remove unimmobilized GO_x; activation of enzyme 30 min at 37°C in incubator.	see above	[160]
lactic acid	water	grow ZnO nanorods, see above soak in 100 μl of LOx (lactate oxidase) solution, 48 h at 4 °C; washed with de-ionized water to remove unimmobilized Lox; activation of enzyme 1 H at 37°C in incubator.	see above	[161]

108

detection	surface cleaning	surface functionalization	measurement setup	Ref.
cells				
cell action potential	ethanol / fibronectin PBS	cardiac myocyte cells of embryonic Wistar rats (3000 - 5000 cells/mm^2)	ΔU_{GS}, U_{DS}, I_D = const, Ag/AgCl reference	[19]
-	water, alcohol, autoclave, PBS	cerebellar granule neurons from Wistar rats, washed with PBS and fixed with 2.5% glutaraldehyde in PBS at 4°C	-	[162]
extra-cellular potential	ethanol	NG 108-15 cells	$I_D(t)$, U_{DS}, U_{GS} = const Ag/AgCl – wire reference	[163, 147]
extra-cellular potential	ethanol, UV Fibronectin (15 µg/ml in PBS)	human osteoblast – like cells from Saos – 2 cell line (~4*10^3 cells/cm^2)	extracellular $U_J(t)$, intracellular potential = -40 mV (using a patch pipette), Ag/AgCl reference	[164]

6.1.1. Oxidation

Oxidation of the GaN surface is one of the most basic functionalization for AlGaN/GaN ISFETs. It gives insight into involvement of Ga_xO_y in the sensing mechanism, serves as basis for covalent binding of functionalizing molecules through hydroxyl groups [158] and is advantageous for stable attachment of lipid membranes and therefore whole cells as well [79]. A thin oxide layer is already formed shortly after the exposure of the ISFETs to air as confirmed by XPS [78, 108, 165-167]. Although the pH response is mostly attributed to this oxide layer, no systematic investigation of the effect of intentional oxidation on the sensor characteristic has been carried out so far. The contribution of Ga_xO_y to the pH response was recently questioned by Kokawa *et al*. [168]. They pointed out that Ga_xO_y is soluble in alkaline solutions, which would impair the stable operation over a wide pH range. Such solubility was observed under wet etching conditions, i.e. in NH_4OH for 15 min at 50°C, and the etching of stoichiometric Ga_2O_3 is documented only for hot acids [169]. Hysteresis effects and deviations from a linear response of the sensors at $pH \geq 10$ indeed indicate the influence of a degraded surface oxide on the sensing behavior.

For the thermodynamically and mechanically stable attachment of lipid membranes Steinhoff *et al*. [79] state that the wetting behavior of the membrane/semiconductor surface has to be optimized. Thermal oxidation of the surface was found to lower the wetting angle. Increased Al content in AlGaN results in a further reduction of the wetting angle. In addition, N-face material revealed a lower wetting angle than metal-face and XPS analysis showed the enhanced formation of native oxide on the surface with N-face polarity [166]. Further studies revealed the smallest contact angle of about 5° after wet chemical oxidation and thermal oxidation at temperatures between 650°C and 750°C (Fig. 6.2) [79]. For the best oxide layer, which was obtained at 650°C, the sheet carrier concentration density in an AlGaN/GaN transistor structure decreased about 50% [79].

Similarly, oxidation of ISFET gates can be carried out by rapid thermal processing at slightly increased temperatures between 700°C and 800°C in oxygen [167]. With increasing temperature, the oxygen concentration at the outermost surface decreases slightly, whereas a considerably higher amount is detected in the bulk, which is finally responsible for the degrading of an AlGaN/GaN transistor at higher oxidation temperatures.
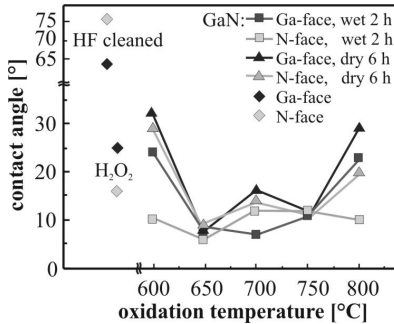
Fig. 6.2: Contact angle on oxidized GaN and AlGaN with Ga- and N-face polarity after wet and dry oxidation as a function of oxidation temperature. For comparison, the contact angles on wet chemically oxidized samples (H_2O_2 at 109°C) and non-oxidized, HF-cleaned samples are shown [79].

The contact angle increases from 5° directly after oxidation to stable 42° after a few days exposed to air (Fig. 6.2). This effect is attributed to contamination with carbon and carbon containing species [78].

6.1.2. Technology impact on the surface properties

Further studies on the impact of typical device processing steps (KOH, HCl, HF wet chemical etching, SF_6 and Cl plasma etching) on the surface properties of GaN based chemical sensors were investigated with emphasis on wetting behavior, chemical composition, biocompatibility and electrical performance of the sensor [78]. KOH free developer has been used since KOH is known to attack group III nitrides [76, 170, 171]. The influence of KOH was investigated by etching the sample in pure solutions with a concentration of 15% for 30 s at room temperature and 70°C. Exposure to HF and HCl solution is a standard cleaning procedure that produces the lowest coverage of oxygen and carbon on GaN. The influence of 10% HF or 15% HCl baths for 5 min at room temperature was studied. ICP mesa etching in Cl_2/Ar gas mixture [172, 173] was used to create 3D structures and to laterally confine the active area of the sensor (see chapter 4.1.2.2). For the fabrication of free standing microelectromechanical systems (MEMS) on silicon, usually an undercutting of the nitride heterostructure by electron cyclotron resonant (ECR) plasma etching in Ar / SF_6-CF_4-CHF_3 mixtures [174] is performed.
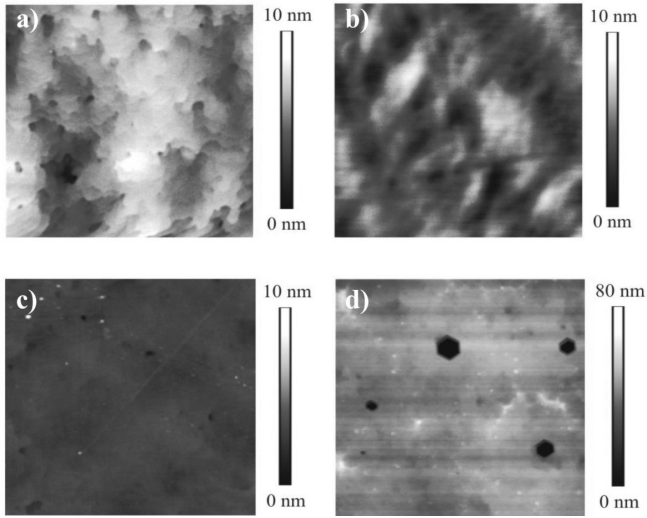
Fig. 6.3: Non-contact AFM images of AlGaN/GaN surfaces (5x5 µm²) a) after growth, b) chlorine and c) fluorine dry etching, and d) KOH etching.

Thus, in this study also the impact of the fluorine based plasma processes on planar AlGaN/GaN heterostructures grown on sapphire was investigated. For biocompatibility tests, first the surface of the nitride heterostructure must be sterilized. Two different sterilization methods are explored, one is the autoclaving procedure in water vapor for 20 min at 121°C and another one is a room temperature method of sterilization by washing in ethanol for 20 min and drying in nitrogen. This second method is used later on also for cell - transistor coupling experiments (chapter 7). As biological model systems the widely distributed mammalian cell lines HEK 293FT and CHO-K1 are used. Biocompatibility test are described in more detail in chapter 6.2. In this chapter only the influence of the treatments on the surface after such tests is discussed.

After MOCVD growth of AlGaN/GaN heterostructures the roughness measured by AFM is about rms ~0.9 nm (Fig. 6.3a). KOH based solutions are preferentially etching defects of the GaN and AlGaN layers leading to local etch pits at the surface (Fig. 6.3d). Such pits can short-cut the 2DEG to the active surface resulting in a drastic decay of the sensor performance (see electrical characterization below).

In the case of Cl$_2$ dry etching, the roughness increases to rms ~2.8 nm (Fig. 6.3b). A positive effect was observed in case of the SF$_6$ plasma etching process in which the GaN surface roughness decreased to rms of ~0.4 nm (Fig. 6.3c). All other technological processes or surface treatments including the cell adhesion are not changing the roughness and no additional treatment-induced features could be recognized.

The XPS analysis of the surface composition was strongly affected by the low conductivity of the sapphire substrate, which results in surface charging. Therefore all photoelectron spectra were shifted by setting the N$_{1s}$ main peak to 398.3 eV binding energy [175]. Due to the capping of the AlGaN/GaN heterostructure, the XPS measurements mainly consist of signals from the 2 nm thick GaN cap layer and only a weak Al signal is observed, because of the relatively low cross sections of the Al$_{2s}$ and Al$_{2p}$ core levels. The inelastic mean free path of the generated photoelectrons in GaN varies between 0.9 nm and 2.6 nm for the energy range of interest (kinetic energy 300-1500 eV), limiting the information depth for the performed XPS measurements to approximately 5 nm.

The impact of different etching treatments on surface composition can be deduced from the spectra in Fig. 6.4; all detected elements are indicated. After wet chemical etching with KOH, HCl and HF, trace amounts of residual material from the solutions were detected on the surface (K, Cl and F). No changes in the peak energy and shape of the Ga and N core level spectra were observed after acid treatment in KOH, HCl or HF solution. Only treatment with HF and HCl caused partial de-oxidation of the surface.

More drastic changes are observed after physical etching. Especially for SF$_6$ plasma treatment, fluorine is accumulated onto the sensor surface (Fig. 6.4f). Furthermore, a strong increase in the O$_{1s}$ signal is observed after the samples have been prepared by plasma etching and being transferred at ambient conditions, accompanied by a strong reduction in the N$_{1s}$ signal.

A more detailed analysis of the Ga$_{2p3/2}$, Ga$_{3d}$, N$_{1s}$ and O$_{1s}$ core levels related to the influence of the plasma processes is shown in Fig.. 6.5. The full width at half maximum (FWHM) of the Ga$_{2p3/2}$ and O$_{1s}$ levels increases drastically after the plasma step. The Ga$_{2p3/2}$ peak can be fitted using two components: Ga-N bonds at 1118.6 eV and Ga-O bonds at 1119.4 eV. On samples after plasma processing, the intensity of the latter one is strongly enhanced. The same behavior was observed for the Ga$_{3d}$ peak (not shown) where the two different chemical states are located at 21.1 eV and 21.9 eV.
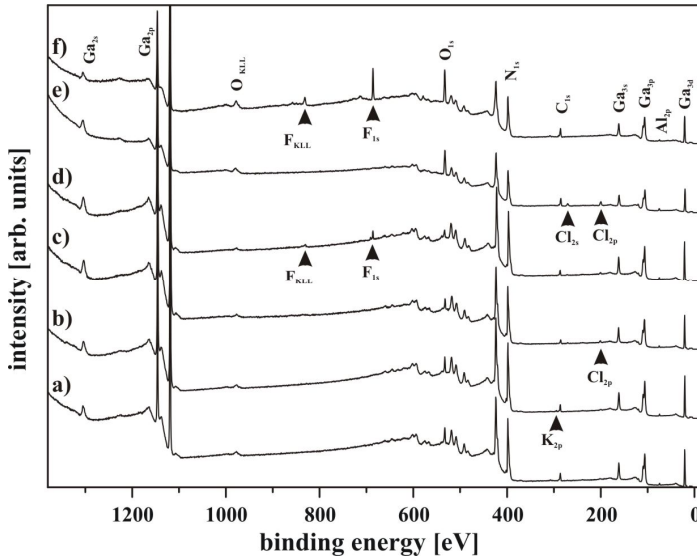
Fig. 6.4: XPS survey scans of the sensor surface: a) untreated, after wet chemical etching in b) KOH, c) HCl and d) HF and after processing in e) Cl_2 or f) SF_6 plasma.

Observed bond energies are in good agreement with reported values on n-type GaN [175-178]. An increased intensity at the high binding energy side of the O_{1s} peak is connected with the removal of emission at 401.3 eV in the N_{1s} signal (which is related to N-O type bonds) is observed.

It is known that plasma processes result in nitrogen deficiency and formation of metallic clusters on the surface [179]. The observed changes in the relative intensity of the core levels as well as their peak shape changes lead to the conclusion that during plasma etching a metallic phase is formed on the surface. When exposed to ambient conditions, these surfaces are directly oxidized due to the high reactivity of metallic Ga, resulting in the formation of gallium oxide on the surface. This has strong influence on the measured contact angle and the electrical properties as will be shown below. In comparison to untreated samples again no significant changes in the peak energy and shape of the Ga and N core level spectra were observed for samples which were sterilized by water vapor or which were cleaned after contact to the HEK 293FT or CHO-K1 cells in with their cell media.
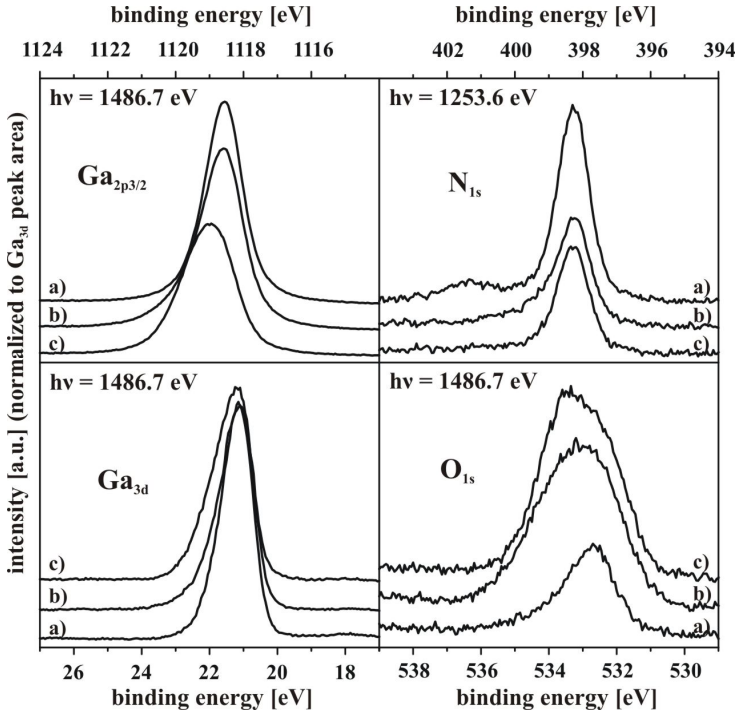
Fig. 6.5: XPS $Ga_{2p3/2}$, Ga_{3d}, N_{1s} and O_{1s} core level spectra a) of the untreated sensor surface and b) after surface treatment by Cl_2 plasma and c) SF_6 plasma. All peaks are normalized to the Ga_{3d} peak area.

These results are in agreement with the AFM measurements (Fig. 6.3). Nevertheless, biological treatments increase the amount of contaminations seen by the increase in the C_{1s} and O_{1s} intensities in Fig. 6.6. Especially autoclaving increases the amount of carbon. Furthermore, samples which had contact to cells and/or cell medium showed trace amounts of residual metal elements like Zn, Ca and K, originating from the nutrients in the cell medium itself (see Fig. 6.6). Therefore cleaning in polar and non-polar solvents is not effective to remove the organic material stemming from the cells as well as the various components of the cell media completely. It can be expected that this contaminating, especially the remaining alkali metals, will influence the sensor signal and its long term stability.
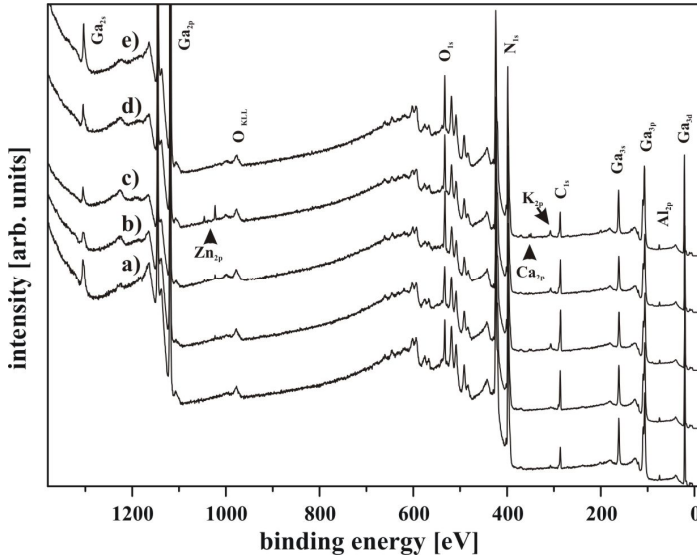
Fig. 6.6: XPS survey scans of the sensors: a) untreated, b) autoclaved, c) after storage in cell medium, after adhesion of d) of CHO-K1 e) HEK 293FT cells. Samples b)-e) were additionally cleaned in acetone and water.

The difference of the contact angle to water after different etching treatments with respect to the angle on the untreated surface is shown in Fig 6.7. Most of the investigated treatments change the wetting behavior of the surface; however, after a few hours at environmental conditions the starting value of about 50° is recovered. The strongest influence had the HF and the SF_6 plasma etching process. In the case of SF_6 plasma etching, the contact angle decreased strongly due to the formation of a thin surface oxide as described before. In contrast, HF etching appeared to be more stable on air.

Fig. 6.8 shows changes in the sheet carrier concentration Δn_S of the 2DEG after the exposure to different media. Except for the fluorine plasma treatment, the carrier concentration decreases after first exposure. A similar trend was observed for the electron mobility, i.e., the electrical performance of the sensor device degrades after initial use. Cl plasma homogeneously etches group III-nitrides (Fig. 6.3b) and consequently, destroys the AlGaN barrier and prevents the formation of a 2DEG. Similarly, KOH etching locally destroys the AlGaN barrier by the formation of etch pits (Fig. 6.3d).
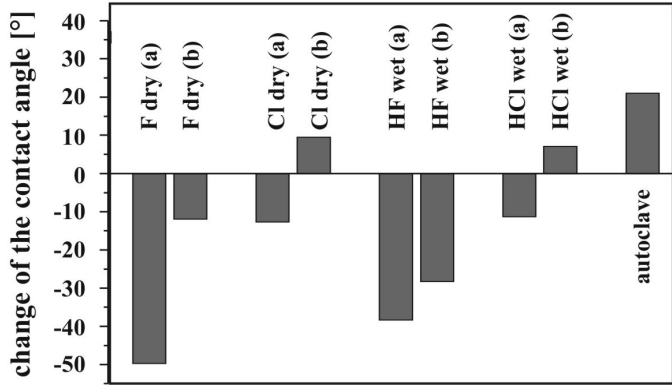
Fig. 6.7: Difference of the contact angle to water before and after different treatments: a) and b) represent measurements immediately after treatment and after one day, respectively (F dry: SF_6 plasma, Cl dry: Cl_2 plasma treatment. Autoclave was performed after cell adhesion experiments.).
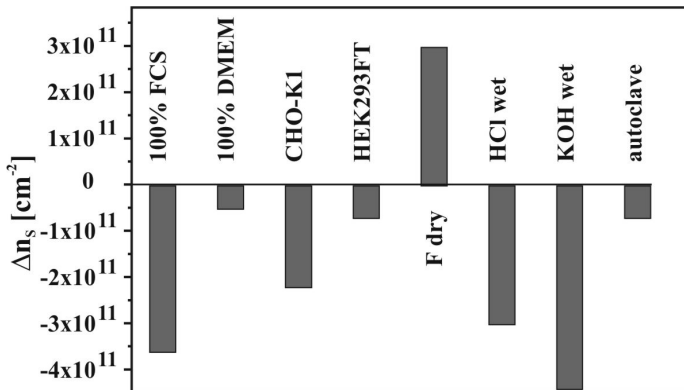

Fig. 6.8: Difference in the sheet carrier concentration Δn_s before and after the exposure to different media.

By wet chemical etching, the sheet carrier concentration of the 2DEG decreases due to the removal of the thin oxide layer (Fig. 6.4c,d), which passivated the sensor surface. After the contact to cells or cell media, the high contamination level on the surface is responsible for the reduction of the carrier concentration.

Only in the case of fluorine plasma treatment an improvement of the electrical performance was observed. XPS revealed a strong increase of the surface oxygen concentration due to preferential nitrogen removal and the subsequent oxidation of the remaining group III elements on the surface. This homogenous oxide layer is responsible for a passivation of the sensor surface resulting in the observed electrical improvement. A summary of the observed positive or negative effects of the treatments on the surface properties is given in table 6.2.

Finally it should be noted that the modification of the wetting behavior (Fig. 6.9) of the gate area of AlGaN/GaN ISFETs and the surrounding parts enable the confinement of liquids to the active area (Fig. 6.9c), which becomes important for the measurements in droplets [160, 180, 181-183]. As described before, the oxidized gate surface is hydrophilic, while hydrophobic behavior with a contact angle about 100° can be achieved by the deposition of fluorocarbon layers in an inductively coupled RF plasma etching system (ICP) (Fig. 6.9b).

Tab. 6.2: Summary of the impact of different surface treatments on the surface roughness (rms), the contamination with carbon, oxygen and other elements (ions are Zn, Ca, K), the contact angle Φ, and the sheet carrier concentration in the 2DEG. Arrows up and down mean increasing and decreasing value, respectively, circle: no change, in the case of rms and 2DEG + and – displays improving or degrading effect, respectively [78].

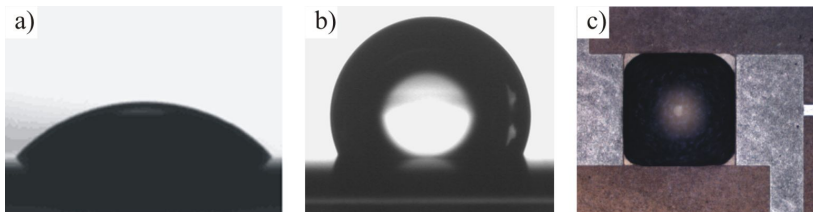|	rms	C	O	cont.	φ	2DEG
F, dry etch	↘ (+)	○	↗↗	F	↘↘	↗↗ (++)
Cl, dry etch	↗ (-)	○	↗	(Cl)	↘	
HF, wet etch		○	↘	(F)	↘↘	
HCl, wet etch		○	↘	(Cl)	↘	
KOH, wet etch	↗↗ (--)	○	○	K	↘↘	↘↘ (--)
autoclave		↗↗	↗		↗↗	
CHO-K1		↗	↗	ions	↗	
HEK293 FT		↗	↗	ions	↗	
DMEM		↗	↗	ions	○	
FCS		↗	↗	ions	○	↘ (-)

Fig. 6.9: (a) Hydrophilic and (b) hydrophobic AlGaN surface obtained by oxidation and CF_x coating, respectively, (c) nanodroplet confined on the hydrophilic active area of an AlGaN/GaN sensor with hydrophobic surrounding [180].

6.1.3. Ion selective membranes

The sensitivity of GaN films and AlGaN/GaN ISFETs to ions was demonstrated for a number of different anions in aqueous solutions (Cl^-, HPO_4^{-2}, ClO_4^-, Br^-, NO_3^-, SCN^-) [114-116].

However, for practical applications as ion sensors, selectivity towards specific ions has to be achieved. For Si-based ISFETs selective detection of K^+ [184] and Na^+ [185] was demonstrated using polymeric ion selective membranes.

For AlGaN/GaN ISFETs the simplest functionalization to enhance selectivity was accomplished depositing a thin (~ 20 nm) Au film on the open gate [98], which resulted in a increased of sensor response on halide ions (F^- and Cl^-) (Fig. 6.10).
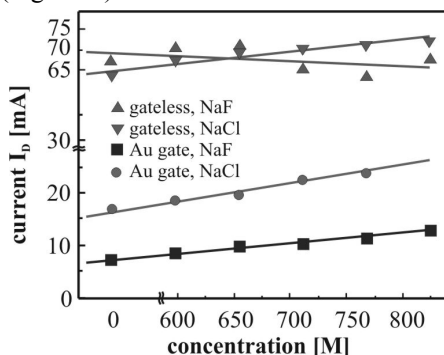
Fig. 6.10: Dependence of the drain current on different concentrations of Cl^- and F^- using a bare and an Au gated AlGaN/GaN ISFET [98].

While no discernable increase in the sensitivity towards F^- is observed, the sensitivity towards Cl^- is considerably higher using Au gated ISFETs. This effect was attributed to the more rapid and stronger adsorption of Cl^- on Au surfaces compared to the adsorption of F^-. The Au film was also the basis for the functionalization with thiol-groups (SH-C_{18}), which formed a self-assembled monolayer and can be used to immobilize biomolecules such as DNA fragments (chapter 6.3).

Higher selectivity to ions can be achieved by covering the AlGaN/GaN ISFET gate with polyvinylchloride (PVC) membranes doped with ion-selective ionophores. This technique was successfully employed by Alifragis *et al.* [113] for the selective sensing of K^+, NH_4^+, Na^+, and NO_3^- (Tab. 6.3). In the case of K^+, the sensor showed a high selectivity and a good stability and reproducibility. The selectivity coefficient $\log(S_K/S_i)$ of K^+ to another ion i is in the range of -3 to -4 against Na^+, Li^+, Mg^{2+} and Ca^{2+} and -1.2 against NH_4^+.

Tab. 6.3: Sensitivity to specific ions using AlGaN/GaN ISFETs coated with polymeric ion-selective membranes [113, 186, 187].

ion	detection limit	linear range	Sensitivity
K^+	$3.1 \cdot 10^{-6}$ M	10^{-5} -10^{-2} M	-52.4 mV/pK^+
NH_4^+	$5.4 \cdot 10^{-6}$ M	10^{-5} -10^{-2} M	-55.5 mV/pNH_4^+
Na^+	$\sim 10^{-6}$ M	10^{-6} -10^{-2} M	-45.6 mV/pNa^+
NO_3^-	$9.4 \cdot 10^{-6}$ M	10^{-5} -10^{-2} M	61.1 mV/pNO_3^+

The modification of ISFETs using specific ion channels of lipid membranes represents a special kind of ion selective membranes (Fig. 6.11, [40, 79, 188]. In a first step, Steinhoff *et al.* showed that it is possible to deposit a homogeneous, void-free lipid membrane on an oxidized AlGaN surface. The lateral diffusion constants of the membrane were measured using constant photobleaching analysis. According to the authors these constants did not depend on the chemical surface composition and the electrochemical surface charge, contrary to previous results on different metal/semiconductor electrodes. In a further step the membrane could be doped with ionophores to achieve ion selectivity.
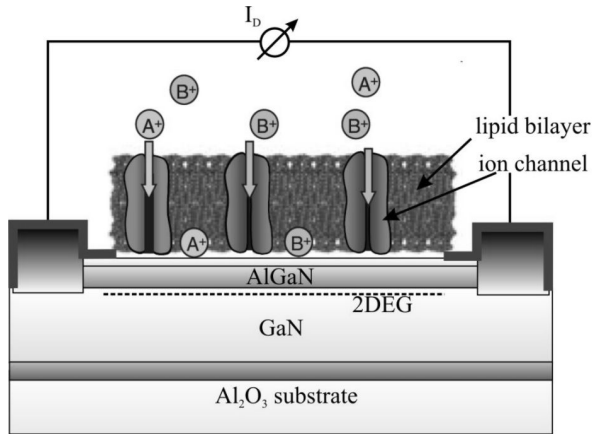
Fig. 6.11: Schematic design of a biosensor on an AlGaN/GaN heterostructure as read-out device for selective ion transport across a lipid membrane via trans-membrane ion channels [79].

6.1.4. Biomolecules

For the functionalization of group III-nitrides with biomolecules, the following approaches of covalent immobilization were applied:

➢ direct chemisorption of biomolecules via amine chemistry [150, 151, 155, 156],

➢ deposition on organosilanes e.g. aminopropyltriethoxysilane (APTES) followed by immobilization of biomolecules via amine chemistry [120, 158, 122, 152], and

➢ using the high affinity of thiols to an Au-coated gate [98] directly via thiol-modified DNA [121] or indirectly binding biomolecules through ester groups [159].

(1) *Direct chemisorption of biomolecules:* The functionalization of GaN surfaces with organic molecules was first performed by Bermudez [150, 151], who analyzed the absorption and bonding of organic molecules, such as aniline ($C_6H_5NH_2$) and 3-pyrroline (C_4H_6NH) on GaN (0001)-(1x1). The analysis was performed by different electron spectroscopic methods in a conventional ultra high vacuum chamber with a base pressure of $\approx 5x10^{-11}$ torr. These fundamental investigations demonstrate that organic amines are easily adsorbed on GaN and they can be used to attach functional groups.

Fig. 6.12: a) Fluorescent image of randomly biotinylated probes on a chemically treated GaN surface and b) of a non-biotinylated surface for comparison [120]. c) Fluorescent image of Alexa Fluor 488 penicillinase conjugates selectively immobilized on a patterned (pattern size 4*4 μm²) functionalized GaN [158].

(2) *Silanization of group III-nitride surfaces:* The silanization of GaN with APTES was reported by Kang *et al*. [120]. They treated as-deposited GaN thin films as well as the AlGaN layer of an ISFET with 1% APTES in water for 24 h to achieve a functionalization with amine groups. APTES serves as a binding layer to the GaN surface for the attachment of biomolecules (Fig. 6.1 up). Sulfo-NHS-biotin was then added to the primary amine-containing self-assembled monolayer of APTES to immobilize biotin. This enables the binding of streptavidin proteins with high affinity. The successful functionalization was confirmed using fluorescent nano particles labeled with streptavidin and bovine serum albumin (BSA). BSA is a protein that has no affinity for biotin or biotinylated surfaces and was used for a control test. The fluorescence image shows strong signals from the streptavidin-nanoparticle-treated sample and only weak diffuse emission from the BSA-nanoparticle-treated control sample (Fig. 6.12a, b). SEM showed a significantly different concentration of nanoparticles with few immobilized streptavidin-coated nanoparticles and large number of BSA-coated nanoparticles. The latter was claimed to be only minimally attached to the surface. The covalent nature of the immobilization was not proven.

A thorough investigation on the covalent functionalization of GaN and AlN surfaces with octadecyltrimethoxylane (ODTMS) and APTES was performed by Baur *et al.* [158]. In order to facilitate the silanization of the GaN surface, a cleaning procedure using 3:1 H_2SO_4 :H_2O_2 (Piranha solution) was employed to achieve hydroxylized GaN and AlN surfaces. In the case of the GaN surface, the cleaning procedure activates not only the surface hydroxyl groups; it leads also to the formation of thin oxide layer.

122

This is not the case for AlN surfaces where a native oxide layer is already present before treatment, and is not significantly enhanced as shown by XPS and X-ray reflectivity (XRR) measurements. ODTMS and APTES layers were deposited in 5% ODTMS/toluene solution with 0.5% butylamine and in 20 mM APTES/toluene solution, respectively. After deposition, GaN and AlN surfaces are hydrophobic. ODTMS monolayer thickness on GaN and AlN was found to be ~1.7 nm determined by XPS, while XRR measurements revealed a monolayer thickness of 2.5 nm. Immobilization of DNA molecules on APTES-functionalized AlN and GaN was used to demonstrate covalent binding of biomolecules. Surface micro pattering of the functionalized surfaces was achieved by illumination with a Hg lamp through a photo mask with 4 µm squares. 20-mer oligonucleotides were subsequently immobilized by Schiff-base formation. Fluorescence microscopy analysis showed that immobilization of DNA had occurred on non-illuminated areas (Fig. 6.12c) and no significant decrease of signal intensity was observed over several days. This emphasizes that the covalent immobilization of biomolecules benefits from a wet chemical hydroxylation of the surface. With respect to the construction of enzyme-modified FETs, the impact of the immobilization process on enzyme functionality was investigated by a comparison of covalent immobilization and physisorption of penicillinase on the gate area of a GaN-capped ISFET [122]. In the first case, the covalent immobilization was carried out by Schiff-base formation on the GaN gate areas modified with an APTES monolayer. The water-sensitive Schiff-base bonds were transformed by sodium cyanoborohydride (NaCNBH$_3$) into stable tertiary amines. For physisorption of penicillinase, multilayers were prepared by depositing the enzymes immediately after cleaning the GaN surface in Piranha solution and incubating until the enzyme solution was dried. The covalent immobilization of the enzyme lead to a superior stability of the device compared to physisorption.

Recently, a comparison of the surface functionalization of wide band gap semiconductors SiC, ZnO and GaN, using different organosilanes was reported [152, 154]. The deposition of mercapto-propyl-trimethoxy-silane (MPTMS) was carried out evaporating 200 µl of pure solution on the surface in vacuum at 150°C. The involved measurements techniques XPS and AFM confirmed the formation of self-assembled monolayers on the surfaces. For the GaN surfaces a clear S$_{2s}$ peak is observable in XPS after the deposition, demonstrating the successful attachment of MPTMS.

The surface (AFM) was found to be very rough on functionalized ZnO, with compressed flat domains of MPTMS molecules (diameter 50-100 nm) for SiC and smaller domains (diameter 10-50 nm) on functionalized GaN. In the case of SiC, XPS measurements revealed that the MPTMS molecules form well ordered layers with thiol head groups uniformly distributed on the uppermost surface while for GaN and ZnO it indicated that the thiol groups predominate on the outermost part of surface. The authors also used GaN MPTMS-functionalized surfaces to immobilize a model biomolecule, i.e., an amino acid derivative pTyr-PT. The linkage was proved by XPS, too.

The deposition of a functional aminopropyltrimethoxysilane (APTMS) layer on GaN films and nanowires were achieved by Simpkins *et. al.* [153] for the immobilization of single stranded DNA (ssDNA). A hydroxylation step with Piranha solution preceded the overnight incubation in a 1% APTMS/ethanol solution. XPS and fluorescence microscopy were used to confirm the deposition of APTMS on planar GaN and on nanowires. The measurements results demonstrate the presence of ssDNA on the GaN surface and also establish that the deposition requires the coupling chemistry, i.e. the DNA is covalently immobilized with minimal nonspecific adsorption. This means that future patterning of GaN in order to detect selective biomolecules immobilization can be successfully achieved. The group studied also the robustness of the bio-functionalization needed for the potential incorporation of DNA functionalized GaN nanowires into a practical fabrication process. Clear fluorescence of individual nanowires observed after sonication used to release them from the growth substrate and dielectrophoretic alignment (DEP) forces to align them across the electrodes revealed that the ssDNA is bound sufficiently strong to the GaN surface. The analysis of the layer morphology and the thickness (AFM and SEM techniques) revealed an rms roughness of 3 nm and an organic layer thickness of about 20 nm. According to the expected maximum monolayer thickness of < 9 nm, the authors suppose a multilayer deposition.

(3) *Au-thiol chemistry:* The application of thiol chemistry in conjunction with Au-coated AlGaN/GaN ISFET was reported by Kang *et al.* for the label-free detection of DNA hybridization [121]. They covered the open gate of the transistor with a 5 nm thin layer of Au and exposed the structure a buffered solution of 3'–thiol–modified ssDNA for 12 h at room temperature. XPS was used to confirm the surface modification via the S_{2p3} and S_{2s} peaks which were present after the modification.

After deposition of thioglycolic acid (HSCH$_2$COOH) molecules by exposing the Au- gated ISFET to a 1 mM aqueous solution for 24 h and the formation of succinimidyl ester groups a buffered solution of monoclonal prostate specific antigen (PSA) antibody were immobilized by incubation for 18 h [159]. XPS was used to confirm the presence of thioglycolic acid on the Au surface, respective the Au-S bond formation on the GaN surface.

It can be concluded that the efforts to functionalize group III-nitrides resulted in various possible modifications (Tab. 6.1) with clear emphasis on silanization due to the possible tailoring of organosilanes to fit a multitude of biomolecules. Owing to the chemical stability of the material system, the modifications have proven to be stable over several days without further optimization. The adsorption of biomolecules directly on the surface via amine chemistry has not yet be applied to actual sensor applications but offers an interesting approach to exploit the advantages of the III-nitrides.

6.2. Cells and biocompatibility

A critical issue to realize cell-on-chip concepts is the survival of living cells on the sensor surface. As shown before, group III nitride based ISFETs are chemically stable under physiological conditions and exhibit promising properties for sensor applications in liquids and electrolytes. Note that silicon is known to be attacked by many biological important agents; however, an appropriate cell growth can be achieved on an oxidized surface. Other semiconductors require high efforts for passivation (e.g. GaAs [189]). In contrast, AlGaN based alloys are chemically inert. First studies with rat-fibroblasts (3T3 cells) demonstrated good adhesion independent of the Al concentration in Al$_x$Ga$_{1-x}$N alloys (x = 0, 0.22, 1), and slightly improved behavior after a pre-treatment by oxidation [79]. Recent investigations using lactate dehydrogenase (LDH) on cerebellar granule neurons prepared from 7-day-old Wistar rats [155] clearly demonstrated that adhesion and growth of living cells on GaN is superior to silicon.

The biological model systems for the present work are the widely distributed mammalian cell lines HEK 293FT, which adhere only poorly and can be removed simply by cell medium flow, and CHO-K1, which are adherent fibroblastoid cells that can only be removed by gentle enzymatic treatment with trypsin. As a third cell line, neuroblastoma-glioma hybrid NG 108-15 nerve cells were used, which are the subject of the transistor-cell coupling experiments in chapter 7.
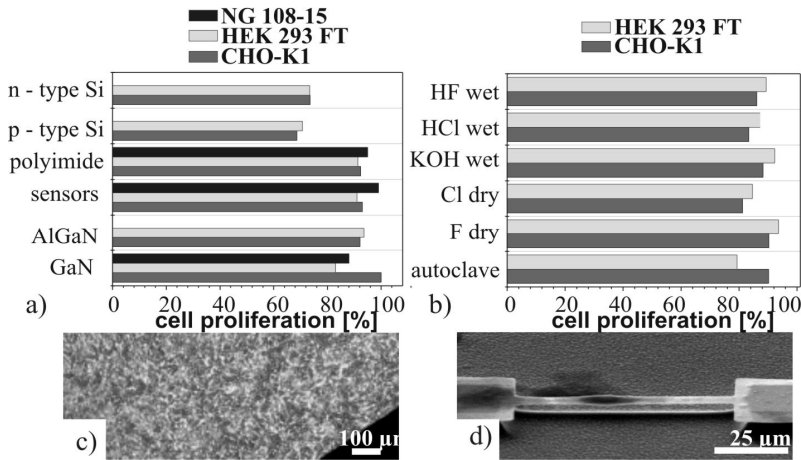
Fig. 6.13: Cell population for three cell lines (HEK 293 FT, NG 108-15 and CHO-K1) after two days cultivation (a) on different substrates and (b) differently treated AlGaN/GaN (c) HEK 293FT on the active area of an AlGaN/GaN sensor, and (d) CHO-K1 on a 3D MEMS sensor [23, 77].

Cells were cultivated in Dulbecco's modified Eagle's medium-high glucose (DMEM) supplemented with 10% fetal calf serum (FCS) and 1% penicillin/streptomycin according to standards set by the American tissue-type culture collection (ATCC). The sterilized sample (1 cm²) was placed in wells of 6-well-tissue-culture plates. One control well without sensor was used as a reference for growth normalization and cell morphology studies. 4 ml of prepared medium were added on every well and $\sim 1 \times 10^5$ cells were seeded uniformly. After two days incubation at 37°C in humidified 5% CO_2 atmosphere, the cells were analyzed by optical microscopy, removed from the well and the sample surface and counted with a Neubauer counter. In addition to the AlGaN/GaN heterostructures, n- and p-type Si substrates were used for comparison. The surface was not modified using fibronectin or other organic materials, which are commonly used in order to improve cell adhesion and biocompatibility. The biocompatibility tests revealed that all cell lines are growing well on the AlGaN/GaN material (Fig. 6.13a). Independent of processing steps the growth on the silicon surface was substantially lower. The surface contamination by carbon, hydrocarbons and metal ions [78] seem to decrease the cell proliferation slightly.

There is evidence that HEK 293FT cells are more sensitive since they show a reduced growth. The cell proliferation is also good on polyimide, which is used for contact passivation (see chapter 4) and thus, part of the final sensor device, which is exposed to the media. Most important for the present work is that the NG 108-15 nerve cell lines proliferates also very well on the sensor surface and the results are similar with the other two investigated cell lines. To further enhance the proliferation of cells on AlGaN a surface modification with fibronectin can be applied as reported by Yu *et al.* [157], however, in contrast to other semiconductors it is not an essential precondition.

Similar to the impact of different treatments on the electrical and surface properties was evaluated in chapter 6.1.2, the influence of these steps on the biocompatibility properties of the sensors was investigated (Fig. 6.13b)[78]. Obviously the treatment of the sensor surface has no substantial influence on the proliferation of the cell lines.

As a consequence, in contrast to silicon based ISFETs no complex modifications are needed to promote the adhesion and proliferation of cells on AlGaN/GaN-ISFETs, though fibronectin-modification might be beneficial. Thus, the superior properties of group III nitride surfaces pave the way for stable and sensitive cell-based biosensors.

6.3. Biosensors

The development of Si based biosensor technologies in the last 30 years was beneficial also for the recent progress of group III nitride based biosensing. In a review on Si based BioFETs in 2002, Schöning and Poghossian [35] classified them using the function of the biorecognition element for the detection as main criterion. In the present work, this classification is adapted for group III nitride based Bio-FETs (Fig. 6.14). The following chapter illustrates the progress that has been made in the development of AlGaN/GaN ISFET based biosensors with respect to these categories and the experimental results that have been achieved.
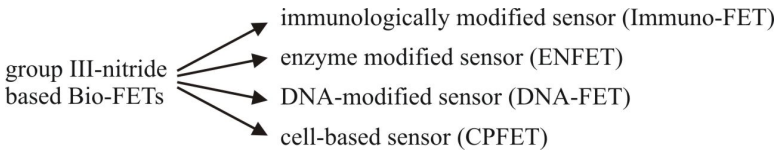
immunologically modified sensor (Immuno-FET)

group III-nitride based Bio-FETs → enzyme modified sensor (ENFET)

DNA-modified sensor (DNA-FET)

cell-based sensor (CPFET)

Fig. 6.14: Classification of AlGaN/GaN based Bio-FETs.

6.3.1. Immunologically modified sensor - ImmunoFET

The study of the molecular and cellular components of the immune system including their function and interaction is the central subject of immunology. The immune system is divided into humoral and cellular components. The humoral (antibody) response is defined as the interaction between antibodies and antigens. Antibodies are specific proteins released from a certain class of immune cells (B lymphocytes). The word antigen is derived from 'antibody generating' which means that it encompasses all substances which trigger an immune response. The recognition mechanism between antibodies and antigens is highly specific and therefore the most promising interaction mechanism for selective biosensing. Immunosensors with immobilized antibodies or antigens are useful for quantifying how well the human immune system is working. A widely applied biosensor in this field is the Enzyme-Linked ImmunoSorbent Assay (ELISA) [190], which is used as a diagnostic tool detecting the presence of antigens or antibodies. As reviewed by Schöning [35] the development towards Si-based ImmunoFETs still faces multiple theoretical and practical problems. Especially the static signal transduction from the antigen/antibody complex, which represents a modified charge, is termed impossible due to the fact that the distance of this charge to the sensitive surface is generally larger than the Debye length and consequently, the charges would by shielded by counter ions [191]. To circumvent this problem, several dynamic methods have been suggested including impedance spectroscopy. The interpretation of the experimental results however is more complex and difficult.

A first approach towards AlGaN/GaN ImmunoFETs was demonstrated using the binding between biotin and streptavidine proteins [120]. Biotinylated surfaces are also used in ELISAs to bind streptavidine or avidin. On the APTES functionalized AlGaN surface (see section 6.1.3) sulfo-NHS-biotin is covalently attached. Both, the immobilization of biotin and the attaching of streptavidine result in a change source-drain current (Fig. 6.15). The bonding between the amine group of APTES and biotin lead to a 5 μA (corresponding to a signal change of 0.3%) decrease of the sensor signal after a reaction time of about 65 s. A second signal drop of about 4 μA (0.2%) was observed after immersing the sensor in streptavidin solution. No current change of the sensor was observed on the sensor without the chemically modified gate. The reproducible measurement after cleaning procedures demonstrated the stability of the functionalization.
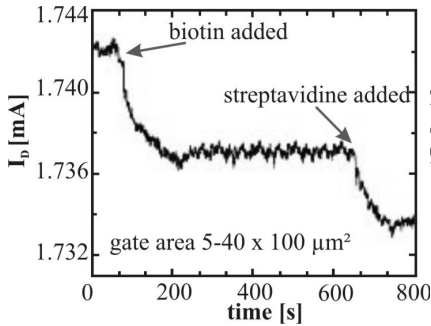
Fig. 6.15: Change of I_D due to binding of biotin to AlGaN and interaction of biotin and streptavidine [120].
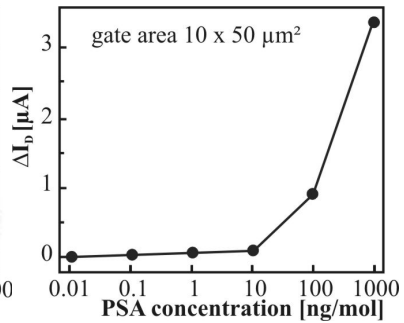
Fig. 6.16: The change of source and drain current as a function of PSA concentration [159].

The first label-free detection of an antigen with modified AlGaN/GaN ISFETs was shown recently by Kang *et al.* [159]. Using the thiol-Au chemistry, the gate was functionalized with PSA antibody (see section 6.1.3). The measured current decreases quickly after exposure to PSA and stabilizes after the PSA has diffused into the buffer solution. The sensor could also distinguish different concentrations of exposed target PSA in a buffer solution (Fig. 6.16). A PSA detection limit smaller 10 pg/ml was estimated with a response time of 5 s. The authors proof the specificity of the device using buffer solution and BSA and observed no current change. Reproducibility and long term stability of the sensor after cleaning procedures were not reported. In the light of the claimed impossibility to measure the binding of proteins statically with Si ISFETs, these results are most intriguing. Since the transducing mechanism on Si and AlGaN/GaN based ISFETs should be similar, more in-depth investigations have to be performed to solve this contradiction.

6.3.2. Enzyme modified sensor - EnFET

Enzymes play an important role in all metabolic processes of living organisms. They catalyze biochemical reactions and enable them to progress at significant rates. Enzymes are highly specific in the binding to educts, also called substrates, forming an enzyme-substrate complex and reducing the activation energy of a specific reaction, e.g. the hydrolysis of the substrate.

Their names are commonly derived from the biochemical reaction they catalyze, e.g. hydrolase. The first biosensor by Clark and Lyons [192] was based on immobilization of glucose oxidase to an amperometric oxygen electrode. It was used to determine glucose level in blood and was further developed into one of the most widespread biosensor devices commercially available. Common glucometers are excellent examples for the potential of biosensors as they are cheap, portable and easy to operate facilitating the treatment of diabetes for millions of people. Immobilization of enzymes on a non-metallized gate area was the first realized BioFET [193] and is still the most investigated BioFET variant. These EnFETs employ the generation of acids by reaction of immobilized enzymes with a specific substrate, and the resulting change of the pH-value of the electrolyte in the vicinity of the sensor surface is detected. Detection of penicillin G using a functionalized AlGaN/GaN EnFET (see section 6.1.3) was reported by Baur *et al.* [122]. The influence of the immobilization process on sensor performance was analyzed by comparing covalent immobilization (c-EnFETs) and physisorption (p-EnFET) of the enzymes. The comparison revealed that p-EnFETs exhibit strong degradation behavior after an increasing number of measurements cycles, while c-EnFETs are highly reproducible. Using the superior c-EnFETs, in 0.5 mM phosphate buffered saline (PBS) containing 25 mM NaCl at pH7, a continuous signal increase for 10 µM to 2 mM of penicillin G due to the acidification in the vicinity of the gate area was recorded. Below 300 µM, a reproducible linear response of the c-EnFETs with a sensitivity of 152 ± 8 µV/µM was observed. At higher concentrations (>3 mM) the signal saturated (Fig. 6.17a), the low detection limit was about 2 µM. Compared to Si-EnFETs, these values are in very good agreement and even slightly superior. It should also be noted that a sensitivity of 123 µV/µM and a detection limit of 5 µM for the Si based EnFET [35] was the result of about 20 years research and transistor optimization, while the AlGaN/GaN based EnFET represents a very recently developed device.

The applicability of c-EnFETs to determine penicillin concentration in µl-droplets was shown recently [194]. A small array of 2 EnFETs and an unmodified ISFET as a blind test with integrated LTCC microelectrodes was used to determine different dilutions of penicillin. The relative pH change calculated from the change of I_D in constant voltage mode is illustrated in Fig. 6.17b. A clear decrease for functionalized c-EnFETs was observed with accelerated kinetics for higher concentrations.
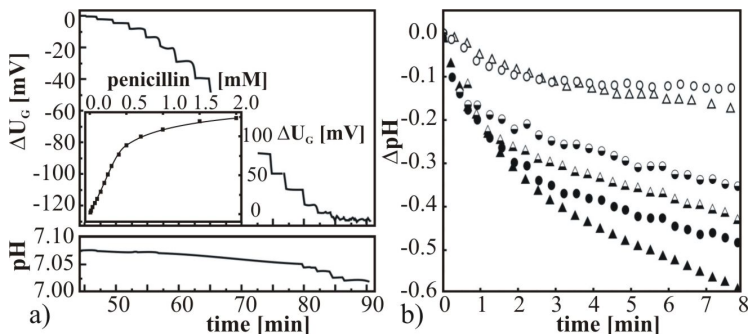
Fig. 6.17: (a) Transient response of an AlGaN/GaN c-EnFET with penicillinase to step-wise changes of the penicillin G concentration from 10 µM to 3 mM in buffer solution. The insert displays the potentiometric response as function of penicillin G concentration [122]. (b) Calculated relative pH-change in 3 µl sample volume upon addition of 2.5 (circles) and 5 mM (triangles) penicillin on a penicillinase-modified c-EnFET (filled) and an ISFET (blank). Half-filled points represent the corrected data [194].

The difference in transient behavior, which leads to ongoing decrease in pH compared to the step-like response as illustrated in Fig. 6.17a, can be explained by additional acidification due to CO_2 diffusion of the solution. Due to the small volume in the µl-range, the pH decreases not only in the vicinity of the surface but in the whole liquid and no steady-state conditions can be reached. Due to the high sensitivity of the small liquid volume to additional external influences, the measurement signal from the ISFET decreases only slightly. This phenomenon is independent of penicillin concentration. Using this array configuration the measurement results are corrected in Fig. 6.17b for those influences.

6.3.3. DNA – modified sensor – DNA-FET

Deoxyribonucleic acid (DNA) is the nucleic acid containing the genetic instructions used in the development and functioning of all known living organism. The DNA hybridization process is the most applied method for detecting DNA and therefore crucial in diagnostics of genetic diseases as well as sequencing the entire human genome. This process identifies unknown single stranded (ssDNA) by formation of a double stranded DNA (dsDNA) with a complementary counterpart.
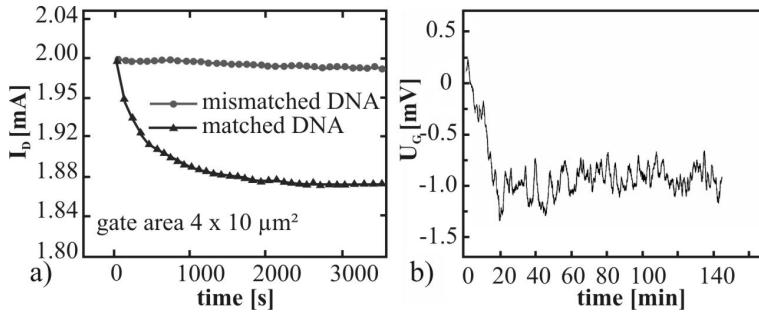
Fig. 6.18: a) I_D of an AlGaN/GaN-DNA-FET after hybridization of immobilized thiol-modified DNA and matched target DNA. No binding was observed for mismatched DNA [121]. b) Potentiometric response of SiO_2-gated DNA-FET to hybridization of matched ssDNA [195].

The common methods to detect hybridization involve labeling with fluorescence markers or radioisotopes and are complex, expensive and time consuming. Similar to ImmunoFETs, label-free detection schemes are desired. A DNA-FET consists of a layer of immobilized complementary ssDNA on the ISFET gate and detects the hybridization event through the additional charge that is introduced by the binding of the target ssDNA. Although this approach suffers from the limitation due to charge shielding from counter ions that was mentioned in section 5.1, direct detection was demonstrated. This is due to the short length of a nucleotide (~0.34 nm compared to a typical Debye length ~1 nm) and isfacilitated by a positively charged transducer surface, which attracts the negatively charged sugar-phosphate backbone of the immobilized ssDNA. By hybridization, this attraction changes leads to detectable change of the charge distribution [35].

Similar to the realized ImmunoFET, Kang *et al.* [121] used thiol-modified oligonucleotides to covalently bind ssDNA with 15 base pairs (bp) to the Au-coated surface of an AlGaN/GaN ISFET. When this DNA-FET is exposed to 1 µM solution containing matched target DNA, the source-drain current strongly decreases within 100 s and continues to decrease more slowly until hybridization is completed after 20 min (Fig. 6.18a). The total change of the current was about 115 µA (i.e. ~5.7%). A control sample containing mismatched DNA leads to no changes in the sensor signal. The authors state that the sensor signal is stable and reproducible even after denaturation of the immobilized DNA and subsequent regenerating process.

Compared to recent results of Si-based DNA-FETs with SiO_2 gate [195], a significantly larger and less noisy signal is obtained at similar conditions. The time response of the FET (gate of 1-2 x 8 {16} µm²) with ssDNA (20 bp) immobilized via an APTES functionalization to 3 µM of matching ssDNA is shown in Fig. 6.18b. It should be noted that the duration of the hybridization process agrees quite well as indicated by a stable signal after ~20 min in both cases. A slightly better response for the detection of increasing quantities of homo-oligomers (i.e. DNA strands containing only one type of base) of adenine (~1000 bp) was shown by Souteyrand *et al*. [196] for a DNA-FET (SiO_2 gate, APTES functionalized) with a larger gate area (20 x 500 µm²). Nevertheless, due to the poor dc response from the Si-DNAFET, dynamic impedance measurement schemes are usually applied [195, 196]. The clear response obtained with AlGaN/GaN DNA-FETs however might open up the way for a simpler dc detection setup.

6.3.4. Cell-based sensor – CPFET

Surely the most interesting, but also most complex biosensor is constructed by oupling whole cells as a bio recognition element with a transducer device. It offers the possibility to study the effect of drugs or environmental influences on cell metabolism directly by measuring e.g. extracellular acidification or intra- and extracellular potentials. Although these cell-sensor hybrids suffer from a short lifetime in the range of several days and a difficult and time-consuming preparation of the device, the direct recording of a living system's response enables to get unique information. Such cell-biosensors are suitable for various applications, such as drug screening in pharmacology, detection of toxins, and environmental monitoring. These applications require an analyzing system suitable for long-term measurements under physiological conditions, which can be achieved by the patch-clamp technique [197], microelectrode arrays [198] or FET arrays [199, 200]. The main drawbacks of these devices are that they are invasive and complicated in the case of patch-clamp or that they exhibits long-term drift in electrolytes due to the electrochemical instability and suffer from a high background noise.

Similar to the reports on Si based ISFETs [200], acidification as result of the cell metabolism was monitored using AlGaN/GaN ISFET [181]. An example is shown for P19 cells (embryonic mouse-teratocarcinom stem cell) adherent on an unmodified open transistor gate.
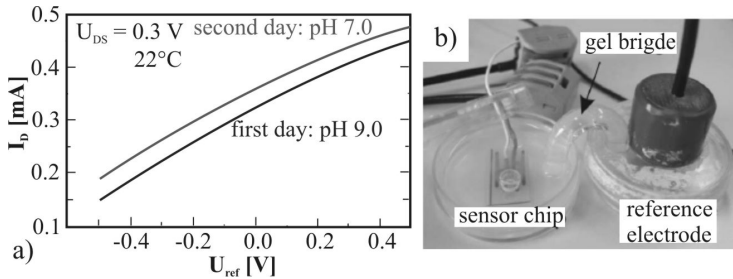
Fig. 6.19: (a) The shift of the transfer characteristics of AlGaN/GaN FET as result of P19 cells acidification. (b) The measurement setup.

After one day in incubator, the cell medium became acidic due to the cellular activity and a change from pH 9 to pH 7 was measured by analyzing the shift of transistor transfer characteristic (Fig. 6.19).

A further development of the concept was demonstrated with cardiac myocyte cells of embryonic Wistar rats on ISFET arrays (Fig. 6.20a) [19]. After 5 to 6 days in culture, a confluent monolayer of cells developed on the fibronectin-modified GaN surface with spontaneously contracting aggregates. The extracellular potential was recorded measuring the drain-source current in constant voltage mode and the corresponding gate voltage U_{ref} was calculated using the transconductance g_m. In Fig. 6.20b, the voltage ΔU_{ref} between cell and transistor gate is shown. Transistor signals were 100–150 ms in duration with amplitude of 70 µV, firing at a stable frequency for several minutes. The signal shape was assumed to be determined by the K^+ exchange; however, the exact reason for this signal shape remains to be clarified. Furthermore, the authors evaluated the gate-source voltage noise in dependence on the frequency and compared it with silicon based devices and concluded that noise in Si devices at the same conditions is one order of magnitude higher.

In a recent publication [157] a combined measurement setup using patch clamp and AlGaN/GaN ISFETs in order to detect the reaction of saos-2 human osteoblast-like cells to different concentrations of known ion channel inhibitors was shown. Quaternary ammonium ion (TEA) and tetrodotoxin (TTX), which block K^+ and Na^+ channels, respectively, are used to influence the ion currents through the cell membrane. The intracellular potential of the adherent cells on the fibronectin-modified open gate of the transistor was controlled using a patch pipette.
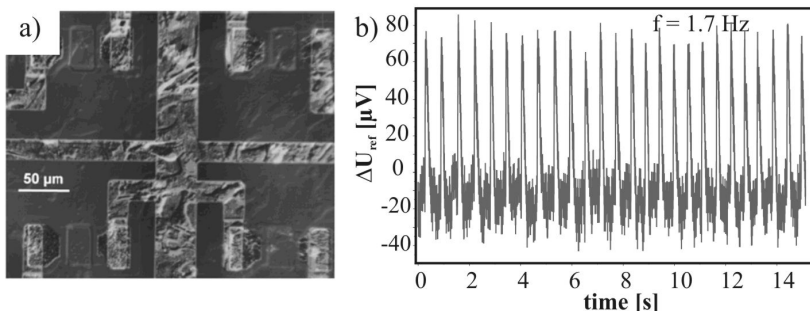
Fig. 6.20: a) Cardiac myocyte syncytium cultivated on an AlGaN/GaN ISFET array. b) Extracellular potential of spontaneously beating cardiac myocyte syncytium recorded with an AlGaN/GaN ISFET [19].

For the measurements a rectangular 90 mV pulse of 600 ms duration was applied to the cell and the extracellular voltage as a function of time was recorded, similar to Steinhoff *et al*. [19], using the AlGaN/GaN ISFET. With increasing inhibitor concentration the amplitude of extracellular voltage decreases and a complete blocking of the membrane channels was achieved with the addition of 20 mM TEA and 50 nM TTX. To study the effect of cell adhesion on the transistor signal, the protein kinase inhibitor H-7 was added to the cell medium. H-7 reduces the abundance of large fibers in the cell cytoskeletal organization and therefore modifies cell adhesion. Depending on the concentration of H-7 the amplitude of the measured signal is reduced continuously within 3 h indicating the loss of adhesion. After removing H-7 by replacing the cell medium the signal slowly recovers which suggests that the cells re-establish contact with the surface.

From the experimental details reviewed in this section it can be concluded that AlGaN/GaN ISFETs are well suited for the construction of CPFETs owing to the inherent properties of group III nitrides like chemical stability and low noise.

The biosensing capabilities of the AlGaN/GaN CPFET will be demonstrated in the next chapter on NG 108-15 (mouse neuroblastoma x rat glioma hybrid) nerve cells by adding different inhibitors that were introduced in chapter 2.

7. Cell-AlGaN/GaN ISFET coupling measurements

Already for a long time researchers have been interested in analysis of the function of the basic unit of biology - the cell. To be able to perform this without to damage the cell or the organism from where the cell is coming, it is necessary to keep the cells alive outside of the organism. This is a very important step to study the cellular functions and metabolisms as well as the cell reaction to different stimuli. The first step was the tissue culture as a biological method, where tissues and/or cells growth was performed separated from the organism. 1885 the first experiments were made by Roux who removed a portion of the medullar plate of an embryonic chicken and maintained it in a warm saline solution for several days, establishing the basic principle of tissue culture [43, 201]. The cell growth is typically facilitated by using of a liquid, semi-solid, or solid growth media, such as broth or agar. In 1907 the zoologist Harrison demonstrated for the first time the growth of frog nerve cells in a medium of clotted lymph [201].

Now, "tissue culture" refers to a three-dimensional culture of non-disaggregated tissues *in vitro*. It is often used interchangeably with cell culture to specifically describe the *in vitro* culturing of stem cells. When the cells are removed from the organ fragments prior to or during cultivation, thus disrupting their normal relationship with neighboring cells, it is called cell culture. Thus, "cell culture" refers to a culture derived from dispersed cells taken from original tissue, from a primary culture or from a cell line or cell strain by enzymatic, mechanical or chemical disaggregation [201, 202]. Such cell culture provides a good model system for:

➢ studying basic cell biology and biochemistry,
➢ the interactions between disease–causing agents and cells,
➢ the effects of drugs on cells,
➢ the process and triggers for aging,
➢ and for nutritional studies.

The present chapter will report on the cultivation of NG 108-15 nerve on a planar device, the AlGaN/GaN ISFET, and the application of this coupling to monitor the reactions of the cells on inhibitors (drugs). An important issue of the system is its ability to allow repeated measurements over long time periods on the same biological material without to damage the proliferated cell layer.

All the involved parts (cells, cell media, buffer solution, sensor interface, etc.) are complex systems, where a variety of different reactions and processes are possible. Not all of them can be analyzed separately by direct techniques. In order to understand the recorded signal in such a complex system, preliminary experiments in defined environment were performed in the following order.

AlGaN/GaN sensor
(4 and 5)

sensor reaction on buffered solutions   cell media
(5.3)   (7.2)
sensor sensitivity to ions in special buffers   pH in cell media
(7.4.2)   (7.2.3)
sensor reaction on inhibitors in special buffers   pH in buffered cell media
(7.4.3)   (7.2.3)

sensor reaction on cell media (pH)
(7.4.1)
sensor reaction on buffered cell media (pH)   cell line NG 108-15
(7.4.1)   (7.3)
sensor reaction on inhibitors   pH in cell media with cells
(7.4.3)   (7.2.3)

sensor reaction on cell media with cells (pH)
(7.4.1)
recording of cellular breathing
(7.4.1)
recording of extracellular potential
(7.5)
single inhibitor

in cell media   in SCZ buffer
(7.5.2)   (7.5.1)

complex reactions on two inhibitors
(in cell media)
(7.5.3)

The basic characterization of the sensor in MT buffer solutions was already described in chapter 5.3. This analysis was extended by studying the sensitivity to Na^+ and K^+ ions (chapter 7.4.2) as well as inhibitors (7.4.3), which are relevant for the cell-coupling experiments. Cell media for the cell growth were independently characterized (chapter 7.2). In contact to the sensor, its response in cell media, the buffering and the dosing of neuroinhibitors were analyzed (chapter 7.4), and the behavior of NG 108-15 cell line (chapter 7.3) as well as its cultivation on the AlGaN/GaN sensors (chapter 7.4) was studied. Finally, the response of the sensors on the cell activity was monitored including spontaneous action such as breathing (chapter 7.4.1) as well as the stimulated reaction on inhibitors (chapter 7.5). Monitoring in a buffer solution with low ion content (SCZ, chapter 7.5.1) supported the identification of relevant ions for the sensor response. As the most complex interaction scheme, the subsequent application of two different neuroinhibitors was studied (chapter 7.5.3). Before describing the experiments in more detail, the next chapter gives an introduction to the NG 108-15 cell line, which was used for the cell-transistor coupling.

7.1. NG 108-15 nerve cell line

Based on their morphology (shape and appearance), cultured cells can be described as [44]:

- ➤ **Epithelial-like** cells, which are attached to a substrate and appear flattened and polygonal in shape,
- ➤ **Lymphoblast-like** cells, which normally are not attached to a substrate but remain in suspension with a spherical shape, and
- ➤ **Fibroblast-like** cells, which are attached to a substrate and appear elongated and bipolar, frequently forming swirls in dense cultures.

The culture conditions play an important role in determining the shape and many cell cultures are capable of exhibiting multiple morphologies.

A cell culture is called Primary Culture if the cells, which are surgically removed from the organism and placed into a suitable culture environment, will attach, divide and grow. Once the cells cover all of the available culture substrate, they must be passaged to give them room for continued growth. Cells are removed as gentle as possible from the substrate using enzymes. The digesting (proteolytic) enzymes, such as trypsin or collagenase are used to break the protein bonds attaching the cells to the substrate.

Some cell lines do not need this enzymatic treatment; in their case it is sufficient to gently scraping the cells off the bottom of the culture recipient. The cell suspension can then be subdivided and placed into a new special recipient. The surplus of cells can be treated with suitable cryoprotective agents, such as dimethylsulfoxide (DMSO) or glycerol, frozen and stored at cryogenic temperatures (below -130°C) until they are needed.

The used NG 108-15 line from ATCC [203] is a fibroblast hybrid cell line derived by fusion of mouse neuroblastoma clone N18TG-2 with rat glioma clone C6BU-1. This cell line has become a widely used *in vitro* model system for studying neuronal functions [204, 205-226]. When cultured in serum containing medium, the cells proliferate well and exhibit significant motility. These cells can easily be differentiated [205-208] and it was observed that the cell properties after this process are greatly enhanced with respect to the following properties: the differentiated cells show increased activity of the membrane protein, which in case of NG 108-15 expresses at least four major families of voltage-sensitive channels (including Na^+, Ca^{2+}, and K^+) [209-220]. These voltage-sensitive channels respond to a variety of channel blockers including tetrodotoxin [213-220], bradykinin [221] and to the drugs, which can produce cell apoptosis (cell death) such as staurosporin [222] and buprenorphine hydrochloride [223]. These cells are electrically active and can be induced to produce action potentials via injection of current [224]. However, spontaneous action potential (as is the case of cardiac cells) does not occur. If the cells are cultured in serum-free media, the electrophysiological and morphological properties are changed. Proliferation ceases and the cells begin to produce neurites and other extensions, which are capable of forming synapses to other tissues and cells [224, 225]. These cells exhibit features characteristic of neurons and are more likely to produce action potentials than their counterparts cultured in serum-containing media. This electrical activity can even be spontaneous under some circumstances. However, as with most neurons, the strength of this spontaneously generated extracellular signal is low, since only a small percentage of cells are active. For these reasons, NG 108-15 cells were not used in action potential studies. Instead, they were used for studies of cellular impedance; examining both motility issues as well as channel conductance changes [204]. Recently, co-cultures of NG 108-15 cells and chick myotubes were reported, which grew together and formed functional neuromuscular synapses. This way, nerve cells induced

the up regulation of muscle AChE expression, which was persistent when the muscular activity was blocked by α-bungarotoxin [226]. Taking such studies into account, the counterpart of the co-culture to NG 108-15 should be replaceable by a sensor in order to monitor cell activity. The good biocompatibility (see chapter 6) of the AlGaN/GaN sensor favors its choice for a coupling with this nerve cell line for the recording of extracellular potential as response to inhibitors. For a proper proliferation of the nerve cells on the sensor surface it is necessary to create optimum conditions of cell cultivation that means good cell media and stable environmental conditions. Such necessary media are described in the following chapter.

7.2. Cell media

For the *in vitro* cell growth, it is important to use a special liquid, i.e. cell media, which contain well defined substances that make cell growth and reproduction possible. For different cell types cell media with quite different properties are required in order to prevent any change of the cell function and the differentiation from the cell stem. Several companies provide a rich palette of cell media. Moreover, researchers can use different components of cell media and compose media for specific cells or cell tissues. To be sure that the composition and the properties of cell media are not changed, it has to be sterile and kept in dark environment and at low temperature. Cell media are usually provided in concentrated form as liquid or powder. These kinds of cell media will be mixed with distillated water. The composition of cell media is described in the following paragraph.

7.2.1. Components of cell media

Basic components in cell media are:

➢ A **buffered salt solution** (PBS: phosphate buffered saline, EBSS: Earle's buffered saline, GBSS: Gey's buffered saline, HBSS: Hank's buffered saline, Puck's buffered saline), which can be chosen in dependence on the cell type.

➢ The presence of different **electrolyte** solutions in cell media is important for keeping equilibrium potential of the cell membrane constant (see chapter 2). Without such electrolytes, the cells cannot survive outside of an organism. Some cell media were analyzed by an electrolyte analyzer and the date are summarized in table 7.1.

Table 7.1: Electrolyte values for different cell media culture [202].

	Human Serum (Arterial)	Iscove's Modified Dulbecco's Medium	Medium 199	Basal Medium Eagle	William's Medium E	McCoy's 5A Medium	Dulbecco's Modified Eagle Medium
pH	7.4	7.4	7.4	7.4	7.4	7.4	7.4
Na^+ [mmol/l]	142	117	139	146	144	142	158
Cl^- [mmol/l]	103	81	125	111	117	106	116
K^+ [mmol/l]	4	3.9	5.1	4.8	4.8	4.8	4.8
Ca^{++} [mmol/l]	2.5	1.1	1.5	1.4	1.4	0.5	1.3
glucose [mg/dl]	100	418	99	94	186	270	382
osmolarity [mOsm]	290	250	270	286	288	289	323

➢ **Amino acids** are responsible for transport of proteins through cell membranes. L-glutamine, L-alanine, glycine, L-serine, L-valine [44, 201, 202] are some of these amino acids which are usually present in cell media.

➢ **Vitamins** (B_{group}, folic acid, biotin, riboflavin, choline) are further important components of cell media. For DNA and RNA synthesis, adenine, thymidine and glucose is necessary [44, 201, 202].

➢ **Antibiotics** and buffer substance such as $NaHCO_3$ or HEPES are significant parts of cell media which contribute to the good proliferation of cell lines [44, 201, 202], as discussed later on.

➢ To accelerate cell proliferation (mitosis) and attachment, further chemical substances are required such as **serum** containing growth and adhesion factors. Serum improves the buffer capacity of cell media and hormone activity and realizes a better cell nutrition and multiplication. Examples are fetal calf serum (FCS), Horse serum, Munchies serum, and Human serum.

An issue of serum to be considered is its provenience from animals. This kind of serum can be infected with different bacteria or diseases which will contaminate the cell culture and affects the research work [201, 202, 204, 227-230]. In addition, high complexity of the serum as heterogenic mixing of proteins, hormones, growth factors, electrolytes and other not well defined components can cause problems for systematic studies due to the limited reproducibility of the exact composition. Thus, the properties and concentration of species in serum can change significantly for different sources or even charges. For this reason it is very important to find cell media without modification of their components from one charge to another and to ensure the right environment for cell growth and proliferation without to modify their function. Recently, serum-free media were used due to their well defined components and stability over time. Problematic might be only the capacity of different types of cells to adapt to this new milieu. For this reason, the selection of a proper serum-free media for a specific cell type can be a quite long and complicated procedure [231].

Since the high amount of substances, which are present in cell media, can influence negatively the tests, more simple chemical solutions, which ensure also a good cell function, are investigated. This kind of solutions will be discussed later (see chapter 7.4.2). Nevertheless, for most of the cell media, a buffer solution for pH adjustment and stabilization is necessary to be added. Its composition and influence is discussed in the next chapter.

7.2.2. Introduction to pH value in cell media

For cell culturing, a stable pH value is a very important precondition [201, 202]. A pH value of cell media below 7 or exceeding 8 can negatively influence cell proliferation as well as their reaction to different stimuli. A pH value of about 7.5 for cell media represents an optimum environment for cell growth. To control the pH value of cell milieu, additional chemical substances are used, which balance it around the desired value (similar to buffer solutions, see chapter 5.1.3.). Sodium hydrogen carbonate is such a substance, which can be added in cell media and act not only as buffer but also as nutrition for plant cells culture. Increasing CO_2 content in milieu causes a decreased pH value. Because the cells need special conditions to proliferate (5% CO_2 and 37 °C), the acid-alkaline equilibrium is kept using sodium hydrogen carbonate in relatively large concentrations. The buffer system in the cell media has thus, two components: $NaHCO_3$ and CO_2.

$$NaHCO_3 + H_2O \Leftrightarrow Na^+ + HCO_3^- + H_2O$$
$$CO_2 + 2\,H_2O \Leftrightarrow H_3O^+ + HCO_3^-$$
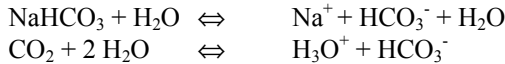
This reaction depends on the partial pressures in the environment. For this reason the cells are kept in special incubators with well defined atmospheric pressure, temperature and CO_2 concentration. If the CO_2 concentration is at a low level, the OH^- concentration in media is high and the pH is balanced in the alkaline region. Then the CO_2 concentration in the incubator must be increased. In this case, the buffer system reacts:

High H$^+$ level: $H_3O^+ + HCO_3^- \Leftrightarrow H_2CO_3 + H_2O \Leftrightarrow CO_2 + 2\,H_2O$,
High OH$^-$ level: $OH^- + CO_2 \Leftrightarrow HCO_3^-$
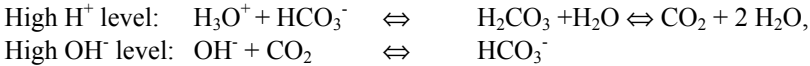
Due to high CO_2 concentration and the presence of sodium hydrogen carbonate in the milieu, the pH is kept constant as long as the cell cultures are in the incubator. Once the vessel with cells is removed and exposed to normal atmosphere with only 0.3% CO_2, the milieu becomes alkaline (i.e. pH about 8.5) and changes its color to violet indicated by Phenol red in the media. Thus, additional buffer solutions such as HEPES or Buffer All have to be added to the cell media. Cell media, which contain already the buffer solution, are also commercially available (i.e. Leibowitz L15) and are especially designed for the work with cell cultures in normal atmosphere.

Prior to any application, such a buffer system has to be tested to proof its biocompatibility with the cell line, for which it will be used. These kinds of tests are presented in the following.

7.2.3. Monitoring of pH value evolution in cell media

As already explained in the previous chapters, cell media are very complex solutions, which regulate their pH value in dependence on the environmental conditions. The experiments with cells in the present work were performed in a glove box at room temperature (22°C), humidity of about 45% and a CO_2 concentration about 0.3%. The NG 108-15 nerve cells were cultured in DMEM supplemented with 10 % FCS and L-glutamine from Sigma-Aldrich (see annex 5), [204]. As can be seen from the components list in annex 5, D5280, the used cell media type of DMEM, contains no buffer solution for a pH regulation in normal atmosphere. However, since the measurements were performed in normal environment, it was necessary to add an additional buffer solution to the milieu.

In literature, most indicated buffer solutions are HEPES and Buffer All [201, 202]. In this work both variants as well as commercial cell media, which contain already a buffer solution (i.e. Leibowitz L15), were tested. However, in those commercial buffered media, the cells did not survive for a sufficiently long time, and these experiments were not further considered. For the measurements, the NG 108-15 cell line was seeded in several vessels in parallel. In the first stage, DMEM supplemented with 10 % FCS and 1% penicillin / streptomycin without buffer solution was used for the cell culture. After three days in incubator at 37°C and 5% CO_2, the cells proliferated well and covered the entire vessel ground. Than the buffer solution was added in different concentrations to the cell media.

The first vessel was stored in an incubator at 37°C with a reduced CO_2 concentration of 0.3%. The second one was returned to the incubator at the standard conditions with 5% CO_2 and the third one was stored in normal atmosphere inside the glove box. A forth vessel was kept as reference in the incubator (5% CO_2) without the buffer solution in the cell media. In addition, four more vessels with cell media but without cells were handled similarly. The pH value of the cell media was checked from time to time using a MT glass pH electrode. The results of these experiments are summarized in Fig. 7.1 and 7.2. In the case of the first experiment (Fig. 7.1) when the vessels with cell media without NG 108-15 cells, containing different concentration of HEPES were stored at 37°C in normal atmosphere (0.3% CO_2), a stabilization of the pH value over a long time and independent of the buffer solution concentration was observed.
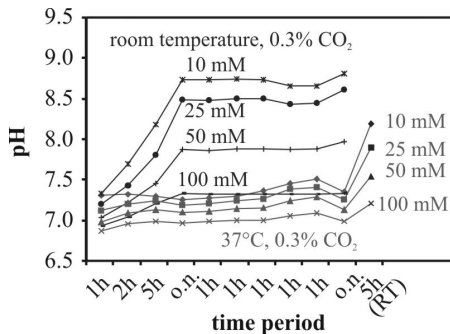
Fig. 7.1: Evolution of pH values as function of the concentration of HEPES solution in cell media without NG 108-15 nerve cells at room temperature (RT) and at 37°C in normal atmosphere (0.3% CO_2), (o.n.: over night).
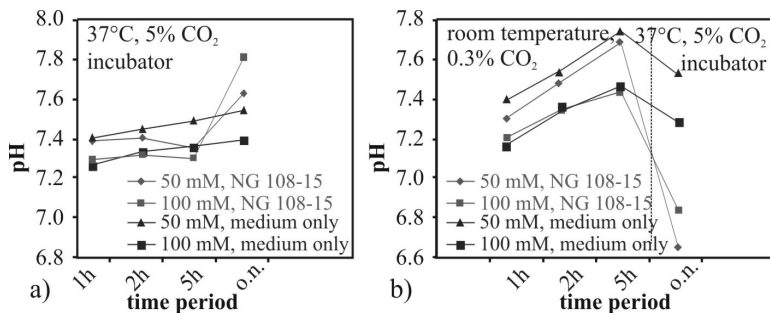
Fig. 7.2: Evolution of pH values as function of the concentration of HEPES buffer solution in cell media with and without NG 108-15 nerve cells: a) at 37°C, 5% CO_2 and b) at room temperature, 0.3% CO_2, (o.n.: over night).

Once the vessel was brought back to room temperature (last 5 h cycle), alkalization of the cell media appeared in dependence on the concentration of HEPES. The same alkalization process was observed if vessels were kept from the beginning at room temperature. After one day at this condition a relative stabilization of the pH value took place. Obviously the ability of the buffer solution to stabilize the pH value is dependent on temperature and at room temperature;a high HEPES concentration of 100 mM is favorable.

The evolution of pH value in time was not significantly different for buffered cell media with or without cells (Fig. 7.2). Thus, NG 108-15 cells and their activity has only minor influence on the pH of cell media, at least within the first 2 hours. At 37°C, 5% CO_2, the pH was effectively stabilized by HEPES. Only after storage in incubator over night, the pH of media containing cells had changed. At room temperature and normal atmosphere (Fig. 7.2a), the pH increased as expected from Fig. 7.1. The process was fully reproducible as the decreasing of the pH after over night storing in incubator ("o.n.") demonstrates. Againbuffered media containing cells behave different after incubator storage; however, this effect was not further evaluated. Within the first two hours, maximal increasing of ~0.3 pH was observed for strongly buffered cell media, independent of the atmosphere where the vessel was kept before. It is important to mention that in the experiment described later in this chapter, recording of the extracellular signal generated by NG 108-15 cell as reaction to inhibitors was performed within maximal 1.5 hours. After this time the cells were returned into fresh cell media and into the incubator for recovering.

146

Summary NG108-15 with 50 and 100 mM HEPES in 10% DMEM+Glut+P/S

medium adaptation: 1 h / 37°C
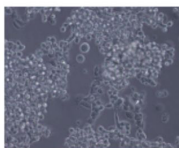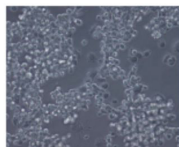
100 mM   50 mM

1 h, RT or 37°C
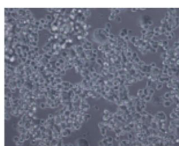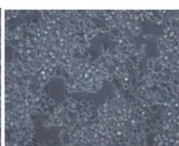
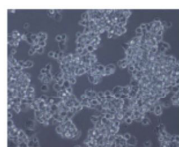1 h RT, 100 mM   1 h 37°C, 100 mM   1 h RT, 50 mM   1 h 37°C, 50 mM
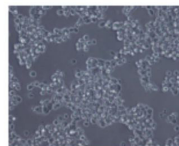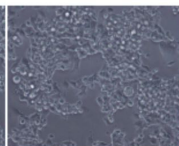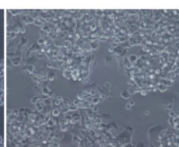
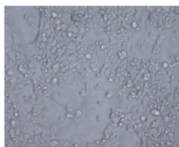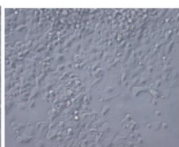5 h, RT or 37°C
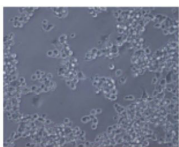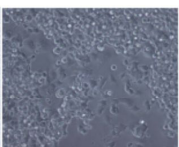
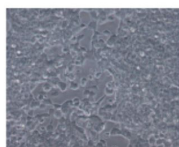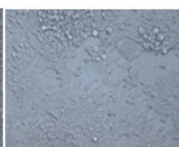5 h RT, 100 mM   5 h 37°C, 100 mM   5 h RT, 50 mM   5 h 37°C, 50 mM
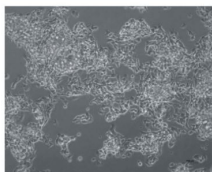
over night, 37°C
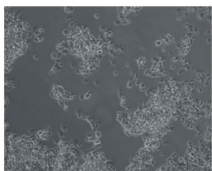

o.n. 37°C, 100 mM o.n. 37°C, 100 mM   o.n. 37°C, 50 mM o.n. 37°C, 50 mM

Fig. 7.3: Optical microscopy of the proliferation of NG 108-15 nerve cells in 10% DMEM with L-glutamine and different concentrations of HEPES buffer solution in different atmosphere.

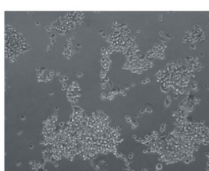starting point (10% DMEM, 48 h)

10% DMEM, 1 h, 37°C, 5% CO$_2$
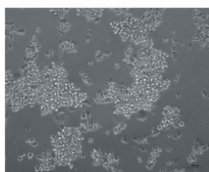

10% DMEMBA, 1 h, 37°C, 5% CO$_2$

10% DMEM, 1 h, 37°C

10% DMEMBA, 1 h, 37°C

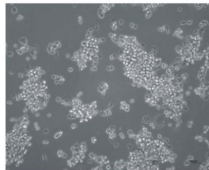10% DMEM, 1 h, RT

10% DMEMBA, 1 h, RT

Fig. 7.4: Optical microscopy of the proliferation of NG 108-15 cells in 10% DMEM with L-glutamine (left) and added Buffer All solution (right).

From Fig. 7.2 it can be concluded that within the first two hours the pH value changed only slightly even for the cells, which are stored at normal atmosphere. Thus, from the point of pH stability, a medium containing 100 mM HEPES buffer solution shows the optimum behavior (Fig 7.1, 7.2). However, a visual inspection of the cell morphology (Fig. 7.3) contradicted this conclusion. Optical microscopy revealed slightly better proliferation for cells that were deposited in cell media with only 50 mM HEPES (Fig. 7.3).
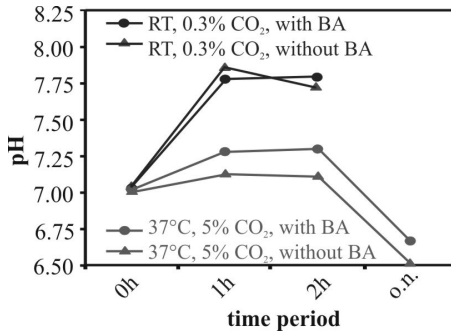
Fig. 7.5: Comparison of the evolution of pH values in cell media with and without Buffer All solution with adherent NG 108-15 nerve cells at 37°C, 5% CO_2 and at room temperature (RT), 0.3% CO_2, (o.n.: over night).

At room temperature, cell proliferation degenerated and cells started to detach from the vessel surface and took a spherical shape already within the first hour. After 5 hours less than half of the cell population was attached to the surface and the remaining swam in the cell media (Fig. 7.3; 5h RT 100 mM). At 37°C with 0.3% CO_2, this described process was much slower. Within the first 5 hours, proliferation seemed to stop; however, the cells were still attached to the surface. After over night storing of the vessel in incubator, the cells recovered. This process was more successful in the case of cells seeded in cell media containing 50 mM HEPES buffer solution. In contrast to the use of HEPES, the NG 108-15 cells were not proliferating well in cell media with Buffer All solution (Fig. 7.4). The cells were shaped spherically and swam in the cell media without being adherently attached to the vessel ground. The pH behavior was not as satisfactory as in case of HEPES buffer solution (Fig. 7.5). The cells started to detach from the vessel ground surface and this appeared to be independent of the atmosphere above the vessel. Only a small difference in pH is observed between the buffered and not buffered cell media. At normal atmosphere, the alkalization process was very strong within the first hour (almost 1 pH unit) and stabilized during the next hour. In incubator conditions, the alkalization process took place only for buffered cell media while normal cell media kept its pH relatively constant over two hours. This proved the inefficiency of Buffer All solution in cell media as well as its toxicity for NG 108-15 nerve cells. Thus, Buffer All solution was not used for further experiments.

To conclude, for pH stability, highly buffered cell media would beneficial; while for cell proliferation a concentration below 25 mM HEPES is preferable. Reported HEPES concentrations to stabilize 7.5 pH are as low as ~10-20 mM [201, 202, 204, 210, 231]. As a compromise, 25 mM HEPES was chosen for the further coupling experiments of NG 108-15 nerve cells with the AlGaN/GaN sensor. To improve the stability of the cell media pH, and to avoid increased Na^+ ions concentrations in cell media, finally a HEPES TRIS 25 mM buffer solution was used. The recorded sensor signals and the experimental characteristics will be discussed in the next chapter.

7.3. Sensor preparation

The used AlGaN/GaN ISFETs were PIMBE grown sensor chips with a large active area of 2400 x 500 µm². They were chosen because of the good sensor characteristics as shown in the preliminary characterization (see chapter 5). Similar to the experiments described in the previous chapter, a sensor chip encapsulated on PBC as described in chapter 4.1.2 (Fig. 4.3b). The corresponding measurement system was the first setup (chapter 5.2, Fig. 5.1a) with the agarose gel encapsulated reference electrode (see chapter 5.2, Fig. 5.2) and the current I_D versus time was recorded using LabView program (see chapter 5.3.4.). This system is utilized for sensor calibration in ionic solution and cell media and also for recording of extracellular potential changes as response to different added neuroinhibitors.

To be able to record extracellular potential of the nerve cell using the AlGaN/GaN ISFET, it is first necessary to create a stable cell-sensor hybrid. This means that the sensor must be biocompatible, well cleaned and sterilized. As shown in chapter 4, AlGaN/GaN is highly biocompatible, which enables direct spreading of the cells on the sensor surface without to use thin films of organic material for improving of the cellular adhesion and biocompatibility. Prior to their spreading on the sensor, the surface must be cleaned and sterilized in order to avoid the infection of cells with bacteria. This is realized by cleaning the sensor and measurement setup with acetone, isopropanol and deionized water followed by sterilization in 75 % ethanol solution for at least 20 min. Finally, the sensors were dried in N_2 flux and after that mounted in the measurement setup. After that, the cells can be spread on the sensor surface. Cell spreading is an essential function of cells, which are adherent to a surface and precedes the function of cell proliferation until the cells completely cover the sensor surface.

The attachment phase of cell adhesion occurs rapidly and involves physicochemical linkages between cells and the sensor surface including ionic forces. Diminished cell adhesion is used as a measure of toxicity, if first the initial attachment of cells is investigated [29, 201].

The NG 108-15 cells were subcultured in Dulbecco's modified Eagle's medium–high glucose (DMEM) supplemented with 10% FCS and 1% penicillin/streptomycin (see cell protocol in annex 6) [203]. When cells showed best characteristics they are picked up without enzymatic treatment and were spread on the sensor surface, which was encapsulated in the measurement setup (chapter 4.1.2). In the initial step of attachment, cells seeded on the sensor showed normal morphology. After 6 hours, attached cells had spherical morphology with rough texture and were more wide-spread as in the beginning. After one day, some of the attached cells spread radial from the centre and developed filopodia (Fig. 7.6a)., Not all cells, however, were attached to the surface. Some of them in spherical form swam in the medium. Moreover, the cells were not uniformly distributed; they were proliferating in groups on the sensor surface (Fig. 7.6a). After three days in incubator at 37°C, a very good proliferation was observed and the sensor surface was completely covered by the cells (Fig. 7.6b).

For the measurements it is very important to have a compact layer of cells covering the whole active area of the sensor. Between cells and a solid surface such as the sensor surface, an ion accumulation channel (the cleft, see chapter 2.3) is formed with a thickness of about 30-70 nm [232]. For continuous proliferation, the cells need to exchange nutrients with the media (see chapter 2), particularly ions. The ion concentration in the cell media is changing depending on the processes, which take place in the cells. For short times, the ion concentration in the channel can increase substantially compared to the media, before equilibrium is reached again by diffusion processes. Because of this short-time non-equilibrium, it is possible to monitor the cell activity by probing the concentration or potential changes in the cleft using different sensors (MEA, ISFET, electrodes). For reliable measurements, this channel should be confined between the active sensor area and a continuous cell culture. Thus, a complete covering of the sensor surface with cells is beneficial for high signal-to-noise ratios. With the procedure described above, about 10^5 NG 108-15 cells were seeded on the sensor. After two days, NG 108-15 nerve cells showed good proliferation and vitality and the active area of sensor was covered with a compact layer.
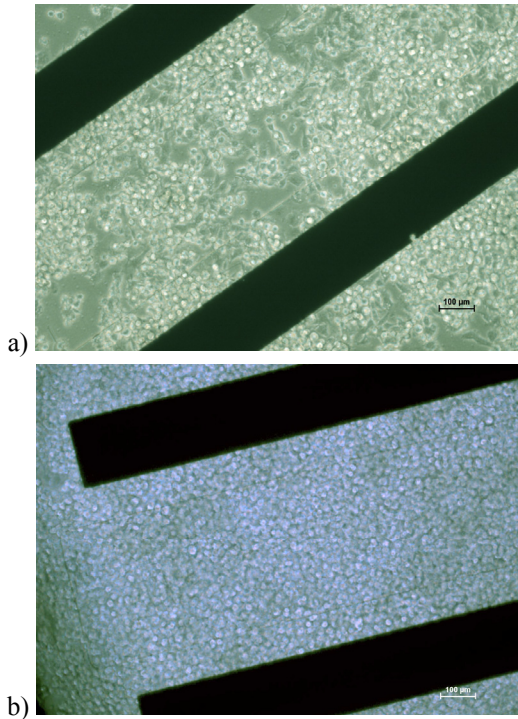
a)

b)

Fig. 7.6: The NG 108-15 cells attached on the active area of the sensor a) after one day, b) after three days immediately before starting the experiments for recording of sensor signals.

Considering a mean cell diameter of 20 µm, about 3500 cells were grown on the active sensor surface. A higher seeding of cells in the beginning can reduce the time for full sensor covering about few hours. However, such a fast proliferation procedure is not recommended because not all the cells have place to attach to the sensor surface and form strong oscillating membrane above the adherent surface. However, even if the cells in the culture are appearing similar, they might show different function and characteristics, and two different cell cultures from the same cell type can be quite different, even if the same growth protocol is used [201, 202]. This might happen also in the case of the extracellular signal recording with the AlGaN/GaN ISFETs in this work.

In biochemical research, this disadvantage of cell culturing can be overcome by highly parallel screening systems. Such measurement methods enable to collect statistic data and determine the error limits; however, they give not the possibility to repeat the experiments on the same biological material over long period. Consequently, for biologists it is important to have an instrument, which uses the same cell culture over several days in order to be sure that cells have the same characteristics. The measurement system with incorporated AlGaN/GaN ISFET in this work permits such kind of measurements, as will be shown in the next chapters.

7.4. Sensor characterization in cell media

To ensure that the sensor records changes of ion concentration in the extracellular media, it is necessary to proof the sensitivity to different ions and to ensure the constant pH value in the media during the measurements.

7.4.1. Sensor response to pH changes in cell media with / without cells

To test the effect of pH changes in the cell media with and without NG 108-15 nerve cells on the AlGaN/GaN sensor sensitivity, the following experiments were performed. First, DMEM cell media, not buffered as well as buffered, was brought on the surface of an encapsulated sensor. In the first run represented by the dark curves in Fig. 7.7a, the measurement setup filled with cell media was not covered. After that the setup was covered with a Plexiglas lid and the measurements are repeated (bright curves).

The sensor signal exhibits a drift (continuous decreasing of I_D) corresponding to an increasing of the pH value of the cell media similar to the previous experiments (see chapter 7.2.). Since the measurements were performed without interruption, the final signal of the measurements without lid is equal to the starting value of the second run with lid, which explains the shift of the curves. Except this, the signal behavior in cell media was not influenced from the cover. In contrast, the presence of 25 mM HEPES-TRIS buffer solution in DMEM cell media resulted in a clearly reduced sensor drift, which demonstrates its function to stabilize the pH value in the media (Fig. 7.7a). The drift did not disappear completely and the reasons can be the continued alkalization of the cell media (chapter 7.2.) cumulated with the noise, which can appear in the system (chapter 5.3.4.)
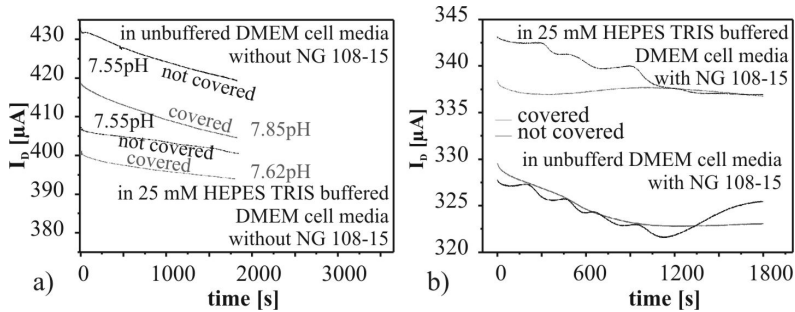
Fig. 7.7: Influence of the measurement setup (covered: bright curves and not covered: dark curves) and the buffer solution on the recorded sensor signal for cell media (a) without and (b) with cells (given pH values are measured at beginning and end of the experiments by MT glass electrode).

The presence of NG 108-15 nerve cells on the sensor surface caused different phenomena (Fig. 7.7b). Comparing the curve recorded in covered measurement setup (bright curves), the sensor drift within the first 1000 s was similar for media with (Fig. 7.7b) and without cells (Fig. 7.7a). The stabilization after 1000 s in the case of present cells might be the result of their activity. In contrast, in buffered cell media and covered setup, the sensor signal was quite stable from the beginning, which again illustrates very well the stabilizing effect of the 25 mM HEPES-TRIS buffer solution to keep the pH in the cell media with adherent cell relatively constant.

A substantial difference can be seen in signal shapes from covered and not covered measurement setup. For covered measurement setup (Fig. 7.7b, bright curve), the recorded sensor signal was relatively constant in time, while for not covered measurement setup (Fig. 7.7b, dark curves), the signal decreased in steps before stabilization. This phenomenon is the result of alkalization [201, 202] of cell media due to changes of CO_2 concentration in the cell milieu (chapter 7.2.). Note that the experiments were performed in normal environment (room temperature, 0.3% CO_2, see chapter 7.2.) after incubation of the setup with NG 108-15 cells and refreshing of cell media. Thus, the recorded signal oscillation is not a sensor drift. It is rather the monitoring of the spontaneous cell activity ("breathing") using the AlGaN/GaN sensor. The faster stabilization of the sensor signal in the case of buffered cell media is due to the homogenizing function of the 25 mM HEPES-TRIS solution added to the DMEM cell milieu.

154

A similar behavior was observed by Silveira [118], using other AlGaN/GaN sensors and the LTCC based setup (Fig. 5.1b). These measurements clearly demonstrate the ability of the AlGaN/GaN sensors to monitor cell activities.

As result of these experiments it can be concluded that in order to ensure stable environmental conditions for NG 108-15 nerve cells cultured on the sensor surface at normal conditions, it is necessary to use a buffered cell media and a covered measurement setup to prevent gas exchange with the environment.

7.4.2. Ion sensitivity of AlGaN/GaN ISFETs

In chapter 2, PMSF, DFP and amiloride and their effect on nerve cells and membrane potential was presented. These neurotoxins were used in this work for cell transmembrane protein inhibition, since they cause a change of the initial ionic concentration in the extracellular solution. In the case of PMSF, DFP and amiloride, Na^+, K^+ and Ca^{2+} ions have the major influence on the sensor signal. As discussed later, it can be assumed that Na^+ ions play the most important role in the initiation of the AlGaN/GaN sensor signal. To be sure that the AlGaN/GaN ISFET is sensitive to concentration changes for at least two different ion types, Na^+ and K^+, a special buffer solution is prepared and new calibration curves are recorded. This buffer solution must ensure a constant pH value and a minimum nutritive factor for culturing NG 108-15 nerve cells for a short period of time (i.e. during the experiments with the cells) without changing the cell characteristics.

The AlGaN/GaN sensitivity to Na^+ and K^+ ions was evaluated in SCZ buffer solution. The choline is used in order to maintain a constant ionic strength in the solution. The buffer solution was added in the setup and after a stabilization time of 10 minutes, the measurements were started. This stabilization time was introduced to reduce the noise from the device (see 5.3.4). The Na^+ and K^+ concentration was subsequently increased by titration of NaCl and KCl, respectively. In Fig. 7.8, the sensor response to changes in ionic concentration is presented. First of all, drift can be seen as decreasing sensor signal in time. This drift is not caused by reactions of the solution, which has a constant pH value of 7.5-7.6. This drift is mainly caused by the used instable agarose reference electrode (see chapter 5.3.4). In the case of Na^+ ions (Fig. 7.8a), the sensor started to react at a concentration of 5 mM with a signal increase of about 2.5 µA.
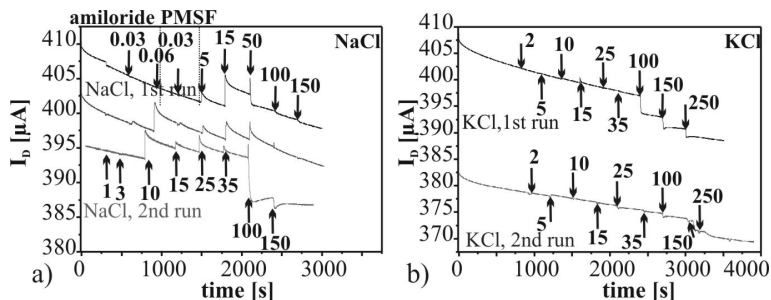
Fig. 7.8: Sensor response upon dosing of (a) Na^+ and (b) K^+ ions in SCZ solution. In the case of Na^+ ions (a) additionally amiloride and PMSF is supplied prior to the Na^+ dosing experiments (dosing by titration, numbers correspond to end concentrations in the solution in units of mM).

After every titration the sensor signal is decreasing again with a lower rate due to diffusion processes, which equalize the ion concentration in the solution and stabilizes the pH value.

Table 7.2: Concentrations of four different solutions used in this work. All solutions stabilize a pH-value of 7.5. The basic buffer solution serves as starting basis for the other three one.

basic buffer	C [mM]	SCR	C [mM]
MgSO$_4$	1	basic buffer +	
HEPES-TRIS	20	KCl	5
glycine	5	NaCl	10
L-glutamine	1	CaCl$_2$	0.15
glucose	10		

SCZ		SCI	
basic buffer +	C [mM]	basic buffer +	C [mM]
choline	135	K acetate	150
		NaCl	10
		CaCl$_2$	0.015

➢ SCZ: - substituted cell media with zero ions
➢ SCR: - substituted cell media with reduced concentration of ions
➢ SCI: - substituted cell media with the same concentration of ions as in the cell.

The fast increase of the sensor signal after titration requires positive ions on the sensor surface, thus, it proves that the sensor is sensitive to Na$^+$ ions. At high concentrations about 100 mM, the positive sensors response decreased, and changed to a negative response, which requires negative ions. Their origin might be recombination processes in the solution, e.g. with choline. This effect was not further investigated since the Na$^+$ concentrations are already irrelevant high for cell-transistor coupling experiments. Similar behavior was observed also in the case of K$^+$ ions (Fig. 7.8b). However, the sensor response was weaker and clear signals could be recorded only at higher concentrations than in the Na$^+$ case. Thus, the AlGaN/GaN sensor is sensitive in the same time to ion concentrations as well as to temporary changes in the solution close to the sensor surface due to chemical reactions.

7.4.3. Sensitivity of AlGaN/GaN ISFETs to inhibitors

This phenomenon is important if the sensor response upon changes of inhibitor concentrations in different solutions is studied. First of all, no sensor response is noted if amiloride or PMSF inhibitors added with concentrations to SCZ solution (Fig. 7.8, upper curve). The same result was obtained in the case of inhibitors added to buffer (25 mM HEPES-TRIS buffer solution) and not buffered DMEM cell media (Fig. 7.9).
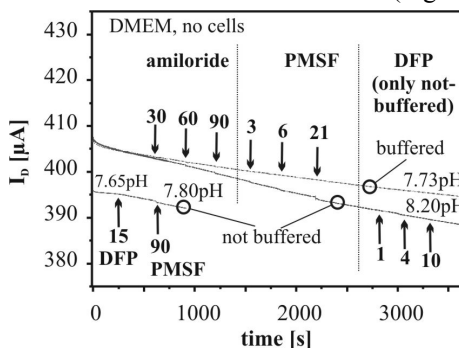

Fig. 7.9: Sensor response to different inhibitors added to cell medium DMEM, with and without 25 mM HEPES TRIS buffer. DFP was only dosed to not buffered media. (dosing by titration, numbers correspond to end concentrations in the solution in units of µM; given pH values are measured at beginning and end of the experiments by MT glass electrode).
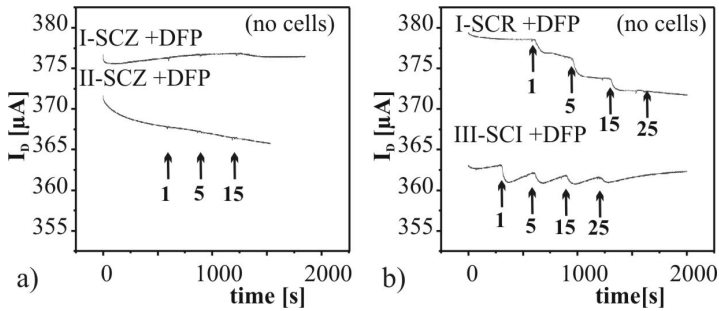
Fig. 7.10: Sensor response to DFP added to a) SCZ, b) SCR and SCI. (dosing by titration, numbers correspond to added concentrations in the solution in units of μM).

Also, no influence was observed in the case of mixed inhibitors in the same basic buffer (see table 7.2). The difference in the slope of the recorded curves is a result of the cell media alkalization in case of the not buffered and buffered cell media as explained in chapter 7.4.2. Furthermore, the sensor response to DFP inhibitor added in SCZ, SCR, SCI and cell media was studied (Fig. 7.10). When the neurotoxin was added to SCZ buffer solution, no sensor signal was recorded (Fig. 7.10a). The situation changed in the case of SCI and SCR buffer solutions (Fig. 7.10b). These staircase like AlGaN/GaN sensor signals can be explained as a result of the chemical reactions between Na^+, K^+ and Ca^{2+} ions from SCR and SCI solutions with the inhibitor DFP. Since in SCZ buffer solutions these ions are not present, such chemical reactions cannot proceed. On the other side, no sensor signal was detected for neurotoxins added to cell media, which contain different type of ions in different concentration (see Fig. 7.9). This can be explained by the fact that the proceeding chemical reactions generate not sufficient ions to produce changes in the sensor signal, or by the complexity of the cell media, which neutralize the resulting components before coming close to the sensor surface. It is to note that the presence of Na^+ and K^+ ions in sufficiently high concentrations in the buffer solution generates a sensor signal when the inhibitor DFP is added. Thus, when the cells are adherent on the sensor surface, the same chemical reactions may not take place in the cleft. The response of the sensor on the specific reactions of the NG 108-15 cells is discussed in more detail in the next chapter.

158

7.5. Recording of extracellular signal

As explained in chapter 2, diisopropylfluorophosphate (DFP) as member of the organophosphates is a very strong inhibitor of AChE. The normal function of Acetylcholine (ACh) starts with its release, the diffusion controlled movement and the following binding to the receptor. The ligand-gated channel opened after binding of ACh for about 10 ms. In the case of differences in the Na^+ concentration inside and outside the cell, influx of Na^+ decreases the membrane potential [20, 44, 48, 233]. The cleavage of ACh by AChE proceeds rapidly and the channel will be closed. Inhibition of AChE leads to a longer holding time of ACh at the receptors and a prolonged opening time of the channel. Repeated use of AChE inhibitors can force the channels to stay open for longer time period and an equilibration of the ion concentration outside and inside the cell will become possible. If it is considered that a homogenous layer of cells was grown on the surface, than between the cells and the surface a cleft is formed (chapter 2.3). Due to the exchange processes of the cells and reduced diffusion (long diffusion path) to the major part of the buffered media, on a short timescale the cleft can exhibit non-equilibrium ion concentrations. This non-equilibrium creates a temporary potential, which can be measured with the AlGaN/GaN ISFET sensor as will be shown in the next chapter.

Before starting the recording of extracellular signal, the measurement setup was taken from the incubator to normal atmosphere, the reference electrode was mounted, the used cell medium was removed and the cells were washed gently with the new cell medium. U_{DS} = 0.5 V and U_{ref} = -0.35 V were kept constant and I_D was recorded versus time. All the experiments were performed in the glove box at a humidity of 45% and a temperature of 22°C. During the recording of the sensor signal, the setup was covered with the lid.

7.5.1 Response on single inhibitors in SCZ buffer

First experiments for cell reaction studies were performed in SCZ since the defined composition enables to conclude, which ions contribute to a sensor response. The cell media was replaced with 5 ml SCZ buffer solution and the cell reaction on the neurotoxin DFP in different concentrations was studied. As presented before, the SCZ is a buffer solution which contains no Na^+, K^+ and Ca^{2+} ions.

Thus, even if neurotoxins block the AChE cleavage and Na^+ channels are kept open for longer time; changes in ion concentration are very small since cells contain only 7 mM Na^+. An ion concentration change of $\leq$ 7 mM by the Na^+ out-flow is too small to be detected by the sensor (Fig. 7.11a). However, when 50 mM NaCl was added to SCZ buffer solution, a fast increasing of the sensor signal (about 15 µA) was recorded. Then, Na^+ ions flow through still open channels into cells. Since the accumulation layer is assumed to be still Na^+ free, this in-flow occurs mainly through channels at the top side of the cells. To establish membrane equilibrium potential, simultaneous K^+ ions are pumped outwards, which occurs at all channels of the cells simultaneously, thus, increases the positive ion (K^+) concentration in the accumulation layer between cell and sensor surface. Note (Fig. 7.11a) that the global pH value of the buffer solution measured using a conventional glass pH electrode was constant during the measurement, ~7.6. Consequently mainly these K^+ ions contributed to the sensor signal.

Using patch clamp technique, Hille [48] measured an equilibrium concentration of 140 mM Na^+ outside of the mammalian neuron. In the present experiment, only 50 mM Na^+ was added to the SCZ buffer solution, thus, full equilibrium could be achieved after the first reactions on DFP, and subsequent adding of the neurotoxin cannot generate a new cell reaction. Indeed, no further extracellular response on new inhibitor dosing could be recorded by the AlGaN/GaN ISFET (Fig. 7.11a, last dosing of 10 mM).

In a second experiment, Na^+ ions were added from start (Fig. 7.11b). The same sensor and measurement setup were used; only new nerve cells were cultivated on the sensor. Optical microscopy revealed the same good proliferation and vitality properties of the cell bed as in the previous experiment. The presence of only Na^+ ions in SCZ buffer creates non-equilibrium of the cell membrane potential. In this case, according to Bernstein theory [43], K^+ ions flow out from the cell through the selectively permeable cell membrane to offset the potential difference. This mechanism can explain the gradual signal increase within the first 900 s. The very first dosing of 5 µM DFP to the SCZ buffer with 100 mM NaCl had no substantial effect on the sensor signal, thus, was too small in this experiment to cause a measurable ion flux. Further dosing resulted in a quickly decreased sensor signal due to Na^+ flux into the cells, seen basically after the dosing of 10 µM and the second dosing of 20 µM DFP. However, this effect was not fully reproducible during the experiment.
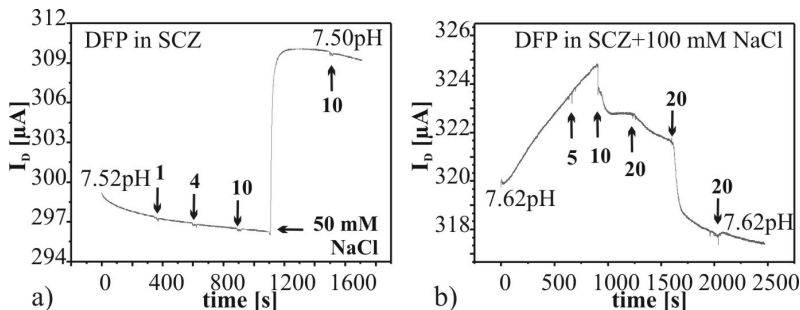
Fig. 7.11: Extracellular signal from NG 108-15 nerve cells as reaction to the neurotoxin DFP in a) SCZ buffer solution and b) SCZ buffer solution with 100 mM NaCl. (dosing by titration, numbers correspond to added concentrations in the solution in units of µM; given pH values are measured at beginning and end of the experiments by MT glass electrode).

The small sensor response on the first dosing of 20 µm DFP might be the result of complex reactions in the medium including the ongoing hydrolysis of the DFP solution and the temporary depletion of ions in the cleft. This effect was not further investigated. In any case, taking into account that the pH value of the SCZ buffer solution was constant at 7.62 during the measurements, the sensor signal can be only the result of ion fluxes across the cell membrane from the accumulation channel close to the sensor surface. Further dosing (third 20 µM DFP and beyond) did not cause sensor responses anymore. Thus, once the Na^+ concentration is in equilibrium between the NG 108-15 nerve cells and the medium as result of the reaction to the DFP neuroinhibitor, no sensor signal is recorded.

Previous investigations on ion sensitivity (chapter 7.3) have shown, that the sensor responds both on K^+ and Na^+ ion fluxes. In this chapter it has been demonstrated that for the monitoring of the cell reactions to DFP neuroinhibitors in SCZ buffer solution, the Na^+ flux is of major importance for the sensor signal generation. However, due to the small ion content in SCZ solutions, the cell reaction to neuroinhibitors can denature. As a consequence, further experiments were performed in a more "natural" cell medium as described in the next chapter.

7.5.2 Response on single inhibitors in DMEM

Instead of SCZ buffer, the complex classical cell medium (DMEM supplemented with 10 % FCS and L-glutamine) was used in the following experiments and 25 mM HEPES-TRIS buffer was added (Fig. 7.12a). Also in this case, the sensor and the measurement setup were not exchanged; only the cell layer was refreshed. Due to the complexity of cell media, it was difficult to keep its pH value constant in normal atmosphere, and for this reason, during the measurement a increasing of ~0.13 pH was observed.

First, the reaction of the NG 108-15 nerve cells on added neuroinhibitor DFP was recorded (Fig. 7.12a). In contrast to the previous experiments, a sensor reaction by decreasing of the recorded current appeared already when the inhibitor DFP with concentrations as small as 1 µM DFP was added to 5 ml cell medium that covered the proliferated nerve cells. A decreasing in the recorded sensor signal appeared also if further 4 µM and 10 µM of the inhibitor DFP were added. After reaching a concentration of about 15 µM DFP, saturation was reached, where no cell reaction could be recorded anymore even if a new dose of neuroinhibitors is added (Fig. 7.12a). Also in this case, the different ions present in the accumulation channel contribute to the generation of the sensor signal; however, because of the complexity of cell media it is hard to determine exactly which kind of ions and in which percentage they contribute to these effects. It can be assumed that Na^+ and K^+ ions have the major influence on the sensor signal. To give an assessment of this hypothesis, an analytical estimation of the sensor signal was performed which is presented at the end of the chapter.

To study the ISFET reaction on the answer of NG 108-15 cells to other kinds of inhibitors, fresh adherent nerve cells were prepared on the sensor with new buffered cell culture medium. This time, amiloride, a reversible blocker of epithelial Na^+ channels, was used as neuroinhibitor (Fig. 7.12b). A remarkable instability of buffered cell media was observed, which became alkaline in time (pH increased by 0.31). First, amiloride with concentration of 10 µM was added to 5 ml cell medium. The sensor signal increased quickly followed by a slower decreasing to the level prior to dosing (taking alkalization into account). Further doses of amiloride caused no sensor reaction anymore. Considering that amiloride closes Na^+ channels, i.e. no Na^+ ions can flow into cells, its dosing lead to increased concentration of positive ions (especially K^+ and Na^+) in the accumulation channel, which finally resulted in the increased sensor signal (Fig. 7.12b).
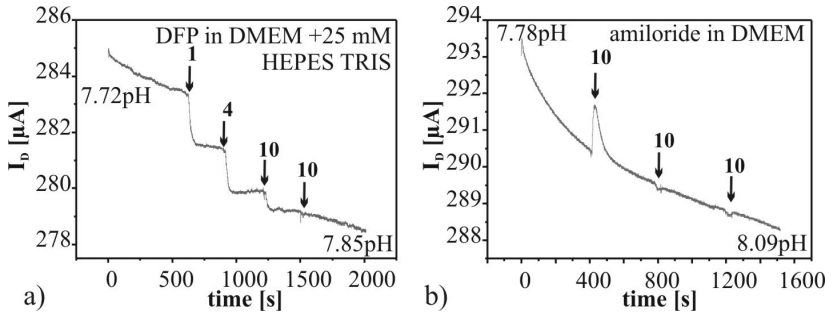
Fig. 7.12: Recorded NG 108-15 cell reaction to different neuroinhibitors a) DFP in DMEM with 25 mM HEPES-TRIS buffer solution as cell medium and b) amiloride. (dosing by titration, numbers correspond to added concentrations in the solution in units of μM; given pH values are measured at beginning and end of the experiments by MT glass electrode).

In time, equilibrium was reached by diffusion processes: (i) laterally out of the cleft into buffer solution, or, (ii) especially for K^+ ions, through ion channels into cells. Thus, equilibrium state of the membrane potential was established and the sensor signal approached its equilibrium value. Due to the alkalization, this equilibrium was smaller than the initial value as a result of the increased pH value. Obviously, the dosing of 10 μM amiloride was already sufficient to block all the channels since further dosing had no influence on the nerve cells and on the sensor signal anymore (Fig. 7.12b).

Further experiments with the second experimental setup (chapter 5.2) and Amani reference electrode (Fig. 7.13) were performed by Silveira [118], which yielded similar results. The sensor preparation and NG 108-15 nerve cell proliferation were realized as described in chapter 7.3. In addition, the sensor response upon dosing of the inhibitor PMSF was investigated. As described in chapter 2, PMSF is a weak inhibitor of AChE [233], i.e., ion channels are opened for a longer time upon dosing, which enables equilibrium of ion concentration outside and inside a cell.

Fig. 7.14 summarizes the results of PMSF titration experiments in 5 ml cell media using two sensors from the same wafer having different active areas. Similar to the above described experiments, the sensor signal showed a continuous decreasing as the result of increased pH due to alkalization. Obviously, upon dosing of PMSF there was a temporary decreasing of the sensor signal as an immediate reaction of the nerve cells.
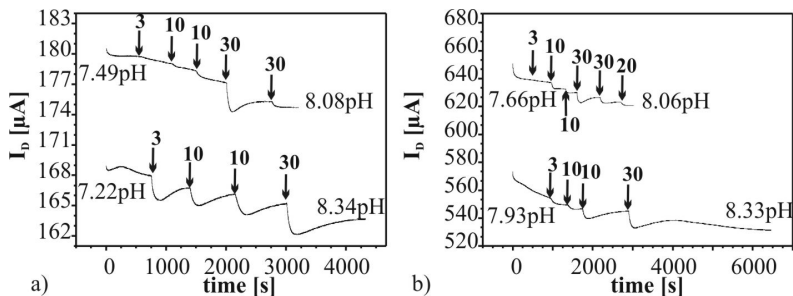
163

Fig. 7.13: The recorded NG 108-15 cell reaction to different concentration of the PMSF neuroinhibitors in DMEM with 25 mM HEPES TRIS, using two different PIMBE grown sensors a) 400x100 µm², b) 2400x100 µm² (dosing by titration, numbers correspond to added concentrations in the solution in units of µM; given pH values are measured at beginning and end of the experiments by MT glass electrode) [118].
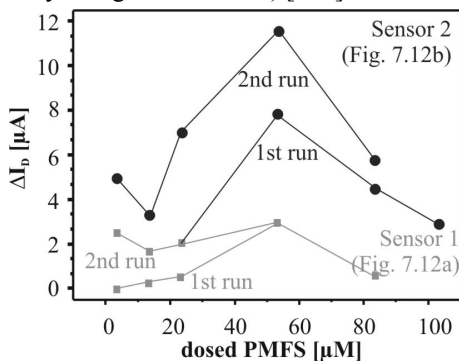

Fig. 7.14: Summary of the recorded changes of the sensor signal in dependence on the titrated PMSF concentration [118].

Because of the open ion channels, the accumulation was experienced to a strong local ion flux across the open channels, which yields to a different ion concentration than in the remaining cell medium and, thus, a measurable sensor signal. The reaching of equilibrium with the cell medium is responsible for the slower recovery of the sensor signal. The analysis of sensor signal changes in dependence on the dosed PMSF concentration revealed a maximum response at about 50 µM PMSF (Fig. 7.14), after which the signal is decreasing as a result of saturation.

These experiments clearly demonstrate that the AlGaN/GaN sensor is sensitive to cell actions, both as result of the "normal" activity (breathing) as well as reaction on external stimulation by neurotoxins. The sensor response and the causing cell reactions are summarized in table 7.3. In the next chapter it will be demonstrated that even complex reaction on different stimulation can be analyzed with those sensors.

Table 7.3: Summary of the observed sensor response on the cell reaction on different treatments.

experiment	cell reaction	sensor response	underlying effect
alkalization	consumption of H_3O^+ and diffusion of CO_2 into the atmosphere	I_D decreases $(\downarrow)$	increasing of OH^- ions
breathing	decreasing CO_2 concentration in the cell medium, creating non-equilibrium of membrane potential	I_D oscillates $(\updownarrow)$	alternating HCO_3^- concentration in the cell medium
dosing of DFP	inhibiting of AChE, thus, keeping the Na^+ channels open	I_D decreases $(\downarrow)$	depletion of positive ions in the cleft (Na^+) due to equilibration of the concentration
dosing of PMSF			
dosing of amiloride	blocking of Na^+ channels	I_D increases $(\uparrow)$	accumulation of positive ions in the cleft (Na^+, K^+)

7.5.3 Response on dosing different neurotoxins

Finally, the reaction of the NG 108-15 nerve cells on the dosing of more than one inhibitor into the cell media was investigated. The used neuroinhibitors for this study were PMSF and amiloride, i.e., subsequently first a neurotoxin that opens ion channels was used followed by dosing amiloride that blocks specifically Na^+ (and Ca^{2+}) channels (see chapter 2).
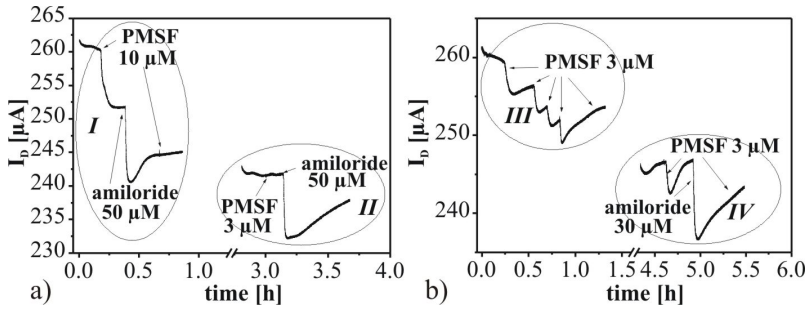
Fig. 7.15: I_{DS} versus time as reaction of the cells in medium to different inhibitors in DMEM without buffer (I- IV) at (a) the first day with a break of two hours and (b) at the second day with a break of three hours.

The electrical measurements were done continuously over several days without removing the cells from the sensor. The sensor signal was recorded in cycles, each of them lasting about one hour. After the measurement cycles the cells were placed in the incubator with replaced fresh medium for recovering. Fig. 7.15 shows the recorded I_D during 4 measurement cycles (I-IV) as a reaction of the dosing of different neuroinhibitors, while the reaction of the pure ISFET without cultivated cells was shown in Fig. 7.9. Obviously a drop of I_D as reaction of the cells on the dosed neuroinhibitors was monitored in contrast to the absence of significant reactions in the case of the uncultivated sensors on the neuroinhibitors added in DMEM cell media (Fig. 7.9). The noise in the signals was about 100 nA, which is more than an order of magnitude lower than the evaluation signal.

Considering PMSF, after dosing of 10 μM PMSF (I), a strong response of the sensor was observed, while a second dosing after about 30 min and additional dosing of amiloride did not cause any variation. A break of 2 h did not change the situation: the sensor signal was on the same level and no response on PMSF dosing could be observed. In contrast, reaction on another neuroinhibitor, amiloride, is apparent in both cycles (I) and (II). Either, 10 μM PMSF was sufficient to inhibit completely the AChE fission and opened all involved ion channels or the amiloride action (blocking of Na^+ channel) limited the response of nerve cell to PMSF inhibitor. The cell media was refreshed and the measurement setup placed in incubator. After 18 h, the cells recovered completely (III). The sensor signal was on the initial level and apparently the cells reacted on a new dosing of PMSF.

166

In cycle (III), smaller amounts of 3 µM PMSF were fed resulting in a gradual decreasing of the drain current. Similar to the first measurement cycle (I), after a forth titration, i.e. after dosing of 12 µM PMSF, no sensor response was observed (III). A break of three hours in incubator resulted in partial recovery of the cells (IV): The sensor signal did not reach the initial value; however, the cells responded again on a single titration of PMSF and showed no reaction on the second dosing. In both cases there was still response on the other used neuroinhibitors, amiloride.

The temporal behavior of the sensor response was fitted by an exponential law

$$I_D = I_{D,e} + \left(I_{D,0} - I_{D,e}\right) * \exp\left(-\frac{t}{\tau}\right), \tag{7.1}$$

where $I_{D,0}$ and $I_{D,e}$ are the drain current at the time $t = 0$ (titration event) and $t \rightarrow \infty$ (equilibrium value), respectively, and τ is a time constant. Similarly, the recovery (sensor signal increase) was examined. The fitted parameters signal change $\Delta I_D = I_{D,0} - I_{D,e}$ and τ for the PMSF titration experiments are shown in Fig. 7.16. The sensor response on every dosing of 3 µM PMSF is approximately constant about 2.5 µA and drops to zero after saturation (Fig. 7.16a, "signal per step"). Accordingly, the sum of the response signals is increasing. The sensor response for the single dosing of 10 µM PMSF in cycle (I) fits very well the sum signal after subsequent titration experiments in cycle (III), which displays the reproducibility of the used sensor.

For an interpretation of the results it is assumed that the sensor signal drop after titration is caused by a decreased concentration of positive ions. Usually, the Na^+ concentration in the electrolyte is high while inside the cell the K^+ concentration is high. Thus, the possible mechanism could be that after PMSF dosing, ion channels are opened and Na^+ ions are transported into the cell. The time constants for the sensor response and the recovery (reproduction of AChE) after every titration event are decreasing with increased dosed concentration c of PMSF (Fig. 7.16b). The lines represent an inverse proportionality between τ and the dosed amount of PMSF: $\tau \sim 1/V$. Consequently, the ion transport to and from the sensor surface is not purely diffusion controlled. Since a direct reaction of PMSF on the ion cannels is assumed via inhibiting the fission of AChE, a higher dosed volume leads to more opened ion channels and thus, in a faster sensor response.
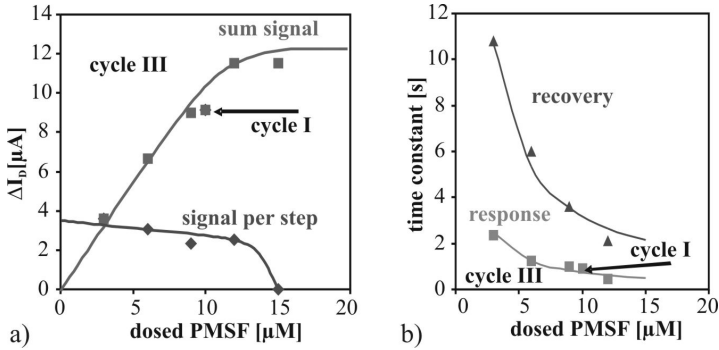
Fig. 7.16: Recorded (a) changes of I_D as reaction on the titration of PMSF during the measurement cycles (I) and (III), and (b) the time constants for the sensor response and recovery after dosing of PMSF.

The recorded data indicate that there is indeed a linear dependence between PMSF concentration and the number of opened ion channels and saturation sets in when all channels are opened. The good agreement of the time constant for dosing of 10 µM PMSF in cycle (I) with the fit for cycle (III) supports this assumption. Remarkably, the sensor signal upon dosing amiloride after PMSF was reversed compared to the dosing of amiloride only as shown in chapter 7.5.2. The response on amiloride and, thus, most probably the direction of the ion flux depends on ionic concentration in the cleft, which is the result of the previous treatment. Obviously the sensor clearly can distinguish between these different cases, however, a conclusive model to explain the observed behavior is not available yet.

7.6. Sensor signal simulation and calculation

To understand the generated sensor signal and the contribution of ions to the recorded signal, a calculation of ion concentrations in the cleft and a simulation of electron sheet density in the sensor channel was performed.

7.6.1 Self consistent simulation of the heterostructure

For the simulation of AlGaN/GaN-based sensors in aqueous solutions a theoretical model was used that implies self-consistent solving the Poisson and Poisson-Boltzmann equations in semiconductor and electrolyte regions, respectively. Details about the model are found elsewhere [107, 138, 235].
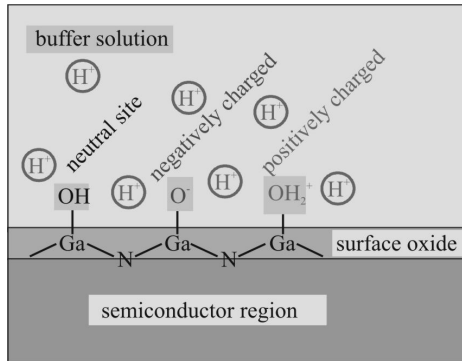
Fig. 7.17: Site binding model for the interaction of the AlGaN/GaN-transistor with the electrolyte assuming a GaO_x interlayer [107].

These simulations provide depth profiles of free carriers in the semiconductor and of different ions in the electrolyte. In the semiconductor, where carrier quantization effects play an essential role, the carrier density depth distribution can be optionally calculated quantum-mechanically through the solution of the Schrödinger equation. The adsorption/desorption of different ion species onto/from the electrolyte-semiconductor interface is described by a site-binding model (chapter 3.2 and Fig. 7.17). It requires the knowledge of the ion concentrations in the vicinity to the electrolyte-semiconductor interface and, accordingly, the site-binding model is self-consistently coupled to the Poisson and Poisson-Boltzmann equations.

AlGaN/GaN sensors provide readout of electrical signals dependent on the particular ion composition in the electrolyte and specific chemisorption of different ions at the electrolyte-semiconductor interface. As an example, Fig. 7.18 presents the calculated carrier concentrations and the potentials for the AlGaN/GaN-based pH sensor exposed to an electrolyte with pH 4.

These calculations consider only one kind of ions; while in the cleft different ions with changing concentrations can be expected. Each of them can contribute differently to the sensor signal. The ion concentrations in the cleft, thus, the sensor response is strongly dependent on the nerve cell activity and its reaction to different stimuli. Nevertheless, the experiments described in the previous chapters revealed a maximum current change of about 5% (table 7.4). With the following simulations, this maximum value will be related to the possible ion concentration changes in the cell media.
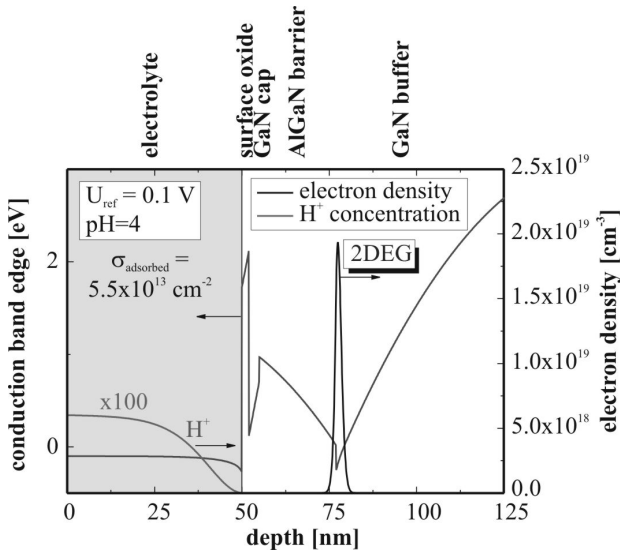
Fig. 7.18: Self-consistent calculation of electron (right) and proton H^+ (left) concentrations versus depth. The site-binding model for H^+ adsorption onto the electrolyte-semiconductor interface predicts a total positive interface charge of 5.5×10^{13} cm^{-2}. The electrolyte region (representing the cleft) is shown in yellow. The conduction band edge in the semiconductor region and the electrostatic potential in electrolyte are depicted by the blue line.

The simulation of the electron sheet density versus ion concentration was realized using a self made program [236]. Fig. 7.19 demonstrates the small changes in the electron sheet density in dependence on the concentration of positive ions in the cleft for different pH values and a fixed cell-sensor surface distance as well as for a fixed pH value but different cell-sensor surface distance. The highest simulated concentration of 10^{20} positive ions corresponds to the maximum concentration of Na^+, K^+ and Ca^+ about 170 mM in the cleft or inside the cells (table 2.1 / 7.1). For this highest ion concentration a change of the electron sheet density of about 4% is achieved, which in a first approximation (neglecting the small changes in the 2DEG mobility) corresponds to a maximum current change of about 4% in a reasonable good agreement with the saturation values obtained experimentally.

This agreement supports the assumption that the sensor signal is indeed generated by the potential changes caused by the positive ion fluxes, and is not a pure pH response.
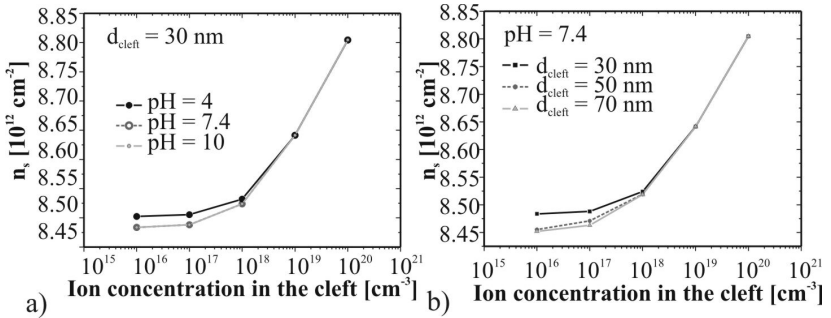

Fig. 7.19: Simulation of changes in electron sheet density in dependence on the concentration of positive ions for (a) different pH values and fixed cleft dimension and for (b) different cleft dimensions and a constant pH value.

Table 7.4: Summary of monitored current changes $\Delta I_{D,sum}$ for the described experiments. ($I_{D,0}$ is the starting value at the beginning of experiments, $\Delta I_{D,sum}$ and $\Delta I_{D,rel}$ are absolute and relative changes of I_D. For subsequent dosing experiments it corresponds to the sum changes over all dosings).

Media	experiment	$I_{D,0}$	$\Delta I_{D,sum}$	$\Delta I_{D,rel}$	Fig.
DMEM	breathing	330 µA	4 µA	1.2 %	7.7b
SCZ	DFP	296 µA	15 µA	5.1 %	7.11a
SCZ + 100 mM NaCl	DFP	325 µA	8 µA	2.5 %	7.11b
DMEM	DFP	285 µA	6 µA	2.1 %	7.12a
DMEM	amiloride	290 µA	1.5 µA	0.5 %	7.12b
DMEM	PMSF	168 µA	9 µA	5.4 %	7.13a
DMEM	PMSF	640 µA	10 µA	1.6 %	7.13b
DMEM	PMSF	260 µA	9 µA	3.5 %	7.15aI
DMEM	amiloride	242 µA	13 µA	5.4 %	7.15aII
DMEM	PMSF	260 µA	12 µA	4.6 %	7.15bIII
DMEM	amiloride	245 µA	12 µA	4.9 %	7.15bIV

7.6.2 Estimation of the ion flux in cleft

Next, the total ion flux is calculated from the available data. The distance d_{cleft} of the cell to the sensor surface is assumed to be 50 nm according to the reported values of 35-70 nm, which have been determined by fluorescence interference contrast microscopy [232].

Table 7.5: Cleft dimensions and total number of Na^+ and K^+ ions in the cleft for the cell-transistor coupling experiments.

	Contact area of single cells		Sensor area	
Area	$A = \dfrac{\pi d^2}{4}$	314 μm²	$A = W*L$	1.25 mm²
Cleft volume (d_{cleft} = 50 nm)	$V_{cleft} = A* d_{cleft}$	0.031 pl		125 pl
K^+ concentration in cell media	c_{K+} = 5 mM			
K^+ total number of ions in cleft		$9.5*10^7$		$3.8*10^{11}$
Na^+ concentration in cell media	c_{Na+} = 160 mM			
Na^+ total number of ions in cleft		$3.0*10^9$		$1.2*10^{13}$

The contact area of a single cell to the transistor was approximated by a circle with the mean cell diameter of 20 μm, while the whole active area of the sensor was 2500 x 500 μm² and a covering of 100% is assumed. The calculated total number of ions in the cleft is summarized in table 7.5.

For estimation of the flux, which is responsible for signal generation, the data from the subsequent dosing experiments in Fig 7.15 were used. According to the simulation results in Fig. 7.19, high ion concentration in cell media causes a nearly linear dependence of the sensor current response with changing charge concentration, i.e., $\Delta I_D \sim dQ/dt$. The saturation current, where no sensor response was measured upon further dosing of PMSF, was $\Delta I_D = 12$ μA. Since I_D is changing in time, its temporary behavior needs to be considered, either by an linear approach $I_D(t) = I_{D,0} \pm \Delta I_D*t$, thus, $Q = \frac{1}{2}\Delta I_D*t$, or by integrating eq. (7.1).

Table 7.6: Cleft dimensions and total number of Na^+ and K^+ ions in the cleft for the cell-transistor coupling experiments.

		Linear approach	Integration of eq. (7.1)
Time period:	300 s		
Current change:	12 μA		
Flowing charges in the cleft [C]		$1.8*10^{-3}$	$1.2*10^{-4}$
Average ion flux	[ions/s]	$3.7*10^{13}$	$2.5*10^{12}$
Maximum ion flux for passive ion channels: 10^8 ions/s			
Ion channels per sensor		$3.7*10^5$	$2.5*10^4$
Ion channels per cell		94	6.2
Ion channels per area	[channel/μm²]	0.3	0.02
Minimum ion flux for passive ion channels: 10^6 ions/s			
Ion channels per sensor		$3.7*10^7$	$2.5*10^6$
Ion channels per cell		9400	620
Ion channels per area	[channel/μm²]	30	2
Flux for active ion channels: 100 ions/s			
Ion channels per sensor		$3.7*10^{11}$	$2.5*10^{10}$
Ion channels per cell		$9.4*10^7$	$6.2*10^6$
Ion channels per area	[channel/μm²]	$3*10^6$	$2*10^5$

Table 7.7: Na^+ channel gating charge densities of nerve and muscles [48].

Tissue	Gate charge [charges / μm²]	Na channel density [channels / μm²]
Squid giant axon	1500-1900	300
Myxicola giant axon	630	105
Crayfish giant axon	2200	367
Frog node of Ranvier	17600	3000
Rat node of Ranvier	12700	2100
Frog twitch muscle	3900	650
Rat ventricle	260	43
Dog Purkinje fiber	1200	200

The charges calculated in both ways are summarized in table 7.6. Taking the uncertainties of these calculations into account, a reasonable good agreement could be achieved between the available Na^+ ions reservoir (see table 7.5) and the saturation value of the ions, which were transported from or into the cleft (see table 7.6) (about 10^{13} ions for the whole sensor). In contrast, the concentration of K^+ ions appears to be too small to explain the recorded sensor signals.

In chapter 2.2, the values for a possible ion flux across the ion channels were given. For the three possible cases, maximum and minimum flux across a passive ion channel, as well as average flux pumped through an active channel, a corresponding number of ion channels are calculated, which would be necessary to cause the calculated ion fluxes (Table 7.6). Obviously, the sensor signal is not generated by a flux across active ion channels, which would require an unrealistic high number of channels. A comparison of the calculated passive channel density of $2-30$ channels /μm^2 with values reported in the literature (Table 7.7) shows that the estimated densities seem to be underestimated. However, it needs to be mentioned that the assumption of $\Delta I_D \sim \Delta Q$ necessarily overestimates the number of flowing charges Q by a factor of 3-5, which in turn underestimates the number of ion channels. Being far away from an exact analysis, the so estimated number of about 100 ion channels per μm^2 shows a fairy good agreement to the measured values for axons in table 7.7.

The major outcome of these calculations is a strong evidence that in the monitoring of cell activity upon neurotoxin dosing, Na^+ flux plays the major role for signal generation. A fairy good agreement between experimental observations and the model could be found, however, the uncertainties in the used methods are still too large to perform a reliable quantitative analysis of the sensor behavior. Nevertheless, the last chapter has demonstrated that such modeling appears to be possible if the measurement conditions as well as used simulation models will be improved further.

8. Summary

In this thesis, AlGaN/GaN heterostructures, which have shown to be reliable pH sensors, were characterized and further developed for the *in vitro* monitoring of cell reactions. It was tested for the reaction of NG108-15 nerve cells on different neuroinhibitors – a reaction, where neither cell action potential experiments have been performed before, nor the proceeding mechanisms are clearly characterized and identified. Nevertheless, it has been shown that these sensors are able to monitor such complex cell reactions. In particular the different sensor reaction on dosing on amiloride depending on the pretreatment demonstrates that biological processes can be distinguished unambiguously, even though they are not understood in full detail. To achieve this goal, the following five major goals have been addressed in this work:

➢ a further improvement of the measurement set-up for extracellular recording in connection with improved chip design and technology,

➢ an accurate characterization of 2DEG heterostructures and sensors grown by different methods (MOCVD and PIMBE) in order to interpret their response in electrolytes.

➢ the effect of device processing steps on the surface properties and the biocompatibility for reproducible culturing of nerve cells on the sensor,

➢ a deeper understanding of the mechanisms in cell-transistor coupling, and finally,

➢ the applicability of the nerve cell-transistor hybrid system in drug screening.

Technical Improvements:

The previously developed sensors and the extracellular recording systems [41, 42] as well as the stability of the setup were improved with respect to the following points.

A novel polyimide contact passivation realizes a good mechanical and chemical stability, high biocompatibility, good transparency in visible light and enables the fabrication of small sensor structures (see chapter 4.1.2.4.). This passivation allows the use of the sensor in both acidic and alkaline solutions ensures a good cell proliferation.

Furthermore, it gives the possibility of nerve cell monitoring using classical inverse microscopy. To improve the sensor stability, a new LTCC based encapsulation was developed (see chapter 4.1.2.5.) and characterized in addition to the existing PBC holder [42]. It showed reduced noise and allowed the continuous use of the sensor for prolonged times without the need to renew the encapsulation.

The set-up for extracellular recording was further improved by using an electrolyte chamber realized from PEEK, a transparent lid of Plexiglas and a special construction which allows the cell monitoring (see chapter 5.2). The PEEK chamber is biocompatible and permits a proper cell growth over long periods. In particular, the lid prevents evaporation and alkalization of cell medium as the result of CO_2 consumption from the environment. The noise was further reduced by the implementation of an aluminum holder for electrical screening as well as mechanically stable contacts.

As a consequence of these improvements, the encapsulated sensor and the measurement setup has improved long-term stability as well as decreased leaking currents (I_{ref} in pA region) and noise (≤ 100 nA). Moreover, this concept makes the measurement system much easier to handle. A good cell proliferation and successful nerve cell-transistor coupling were the direct result of these improvements.

Heterostructure and sensor characterization:

To select optimal sensors for the cell-transistor coupling, heterostructures grown by PIMBE and MOCVD were characterized. MOCVD grown samples have shown to be more homogeneous and exhibit superior electronic transport properties. The poorer electrical performance in PIMBE grown samples is mainly caused by the higher dislocation density. This effect has important consequences for the application as chemical or biosensor, since such defects are etched preferentially and can be the origin of early breakdown in such sensing devices. On the other side, smaller negative potentials were necessary to deplete the 2DEG in PIMBE grown heterostructures. For biosensors, it is very important to work with small potentials close to the cells in order not to influence the metabolism of the cells. Moreover, PIMBE grown heterostructures were less affected by ambient light [42, 140]. For this reasons, PIMBE grown samples were selected for the cell-transistor coupling experiments. However, these properties reflected the state of the development rather than a physical limit for the epitaxial techniques.

It is expected that the further improvement of MOCVD will result in superior heterostructures. For example, the barrier thickness and composition was not varied to adjust the depletion voltage. Moreover, recently Si doped interlayer have shown to improve the light stability in MOCVD grown samples [42]. Also this effect was not further investigated in this work.

Before any quantitative measurement, the sensors have been calibrated, which was accomplished using a known and well defined pH buffer. The transistor characteristics were analyzed in more detail in dependence on the W/L ratio, which is an important value that determines parameters such as the transconductance and, thus, also the sensor sensitivity. It was shown that with increasing of W/L ratio the resistance is increasing due to higher serial resistors on the chip (see chapter 4.2.2.). As a consequence, also the transconductance and sensitivity is affected by these serial resistors. However, for high W/L ratios, the most stable sensor characteristics were obtained in constant current mode with sensitivities $S > 50$ mV/pH.

Noise originating from the heterostructure and its interaction with the electrolyte had a level of about 100 nA. The possible sources of noise are considered to be the reference electrode, contact passivation and the interaction of the sensor surface with alkaline and acidic solution. A potential shift of about 30 mV between Amani and the two different concentrated agarose gel reference electrodes as well as the changing behavior in dependence on the environment clearly demonstrate that the miniaturized self made agarose gel electrode of this work is not usable for quantitative determination of the pH value in an unknown solution. However, these large differences affect not critically the sensor signal on a short time scale. Other drift effects such as the moisture uptake of the polyimide passivation are also rather long-term effects and partial stabilization occurred already during the long preparation periods necessary for the proliferation of cells. As a consequence, most of the drift can be neglected due to the fast response of cells. Thus, even if quantitative pH sensing cannot be assured, the cell-transistor coupling can be studied and the cell reactions can be monitored.

Surface properties and biocompatibility:

Biocompatibility and stability are two major preconditions for the application of AlGaN/GaN heterostructures as biosensors. Generally, good proliferation of different cell lines was observed on AlGaN and GaN surfaces. Importantly, it was realized without using any kind of thin films of organic material such as fibroblasts for improving of the cellular adhesion and biocompatibility.

Furthermore, the impact of several technology- and sensing-relevant treatments on the surface properties of AlGaN/GaN sensors was studied as well as their contaminating effect (see chapter 6):

➢ Most of the investigated treatments change the contact angle. However, after a few hours the starting value of about 50° is recovered.

➢ The investigated cell lines are growing well on AlGaN/GaN and are only little affected by the different processing steps.

➢ Good proliferation was also observed on polyimide, which confirms its suitability for passivation on sensor devices.

➢ Enhanced contamination of the surfaces with carbon, hydrocarbons and metal ions slightly decreases the cell proliferation. Such contamination was removed by the established cleaning procedure with HCl and HF. The remaining traces of chlorine and fluorine have no measurable effect on the sensor.

➢ The sterilization by autoclaving, which is very commonly used in working with cell cultures, contaminates the surface with carbon-containing species. Consequently, a modified sterilization method has been developed for the AlGaN/GaN sensor surface (see chapter 7).

➢ Fluorine etching improves the electrical performance of the sensor in connection with the formation of a surface oxide. Thus, a short fluorine plasma treatment might be beneficial for stabilizing the sensor surface.

➢ Cells and cell media contaminates the surface with metal ions, which cannot be removed by non-destructive treatments, however, no influence on the sensing behavior could be observed.

With these investigations a technological cleaning procedures were established, which maintain the good biocompatibility of the GaN surface to living cells and enables to study the effect of drugs or environmental influences on the cell metabolism directly by measuring extracellular acidification or intra- and extracellular potentials.

Sensitivity and stability in the media for cell-transistor coupling

The present work on cell-AlGaN/GaN FET coupling for biosensing emphasized on the extracellular potential detection, where all involved components (cells, cell media, buffer solution, sensor interface, etc.) are complex systems with a variety of different possible reactions and processes. To ensure reliable cell-transistor coupling measurements, first the pH stability of cell media and the sensor sensitivity to different ions and neuroinhibitors in cell media or special buffer solutions is investigated.

The study of pH stability reveals that a highly buffered cell media would beneficial; while for cell proliferation a concentration below 25 mM HEPES is preferable. As a compromise, a HEPES TRIS 25 mM buffer solution was used to improve the pH stability of the cell media and to avoid an increased Na^+ ions concentration in cell media. The pH stability in cell media and the AlGaN/GaN sensor sensitivity is strongly influenced by the measurement conditions. At normal conditions, a covered measurement setup is necessary to prevent gas exchange with the environment. In an open setup with contact to normal atmosphere, the monitoring of the spontaneous cell activity ("breathing") was recorded.

Primary, the AlGaN/GaN heterostructure is a pH sensitive device; nevertheless it reacts on changing ionic concentrations in electrolyte through the formation of temporary potentials (action potentials in the case of cells). These effects were studied in electrolytes with strongly differing ionic species such as SCZ, SCR, SCI and cell media (see chapter 7.4). The different response of the sensor on the dosing of neurotoxins (no change in SCZ, staircase like signal in SCI or SCR) verified the existence of chemical reactions between neurotoxins and ions in the electrolyte as well as the possibility of their monitoring with AlGaN/GaN sensors. It could be shown that in the cell media, which are used for the cell-transistor coupling experiments such reactions are highly suppressed or compensated and thus, have no influence on the sensor signal.

Nerve cell-transistor hybrid system in drug screening

For the nerve cell-transistor coupling a reliable seeding procedure was established, which could be used for iterative measurements over periods of several days. In the calibration experiments in Na^+ free SCZ buffer, a sensors response on DFP neuroinhibitors was monitored despite the constant pH value of 7.62 in the electrolyte.

It confirms the major importance of Na^+ flux in the signal generation, here as an ion flux across the cell membrane to the accumulation channel close to the sensor surface. Further experiments performed in a more "natural" cell medium showed different cell reaction to different inhibitors. Also in this case, the different ions present in the accumulation channel contribute to the generation of the sensor signal; however, because of the complexity of cell media it is hard to determine exactly which kind of ions and in which percentage they contribute to these effects.

In summary, the following cell media reactions and cell activity could be monitored by the AlGaN/GaN sensors:

➢ Alkalization due diffusion of CO_2 to the environment and to consumption of H_3O^+ (I_D decreases),
➢ Cell breathing, which results in decreased CO_2 concentration in the cell media (I_D oscillates),
➢ Cell reaction on DFP, which keeps Na^+ channels in an open state and depletes positive ions in the cleft (I_D decreases),
➢ Cell reaction on PMSF with similar results, and
➢ Cell reaction on amiloride, which blocks of Na^+. Here the reaction depends on the preliminary treatment. Dosing of amiloride only results in a accumulation of positive ions in the cleft (I_D increases), while a dosing after previous PMSF dosing has opposite result (I_D decreases).

These experiments clearly demonstrate the ability of the AlGaN/GaN-ISFETs for quantitative analysis of cell reactions on different neuroinhibitors. However, with the described structure the kind of participating ions can not be identified definitively. The calculations using simulation of the heterostructure as well as a simplified expressions for the ion flux give a strong evidence that the signal in the cell-transistor coupling experiments is primarily generated by the Na^+ flux. For reliable quantitative analysis, however, the models have to be further developed and various sources of error have to be identified and eliminated. Nevertheless, the AlGaN/GaN-ISFETs show stable operation under physiological conditions, exhibit a very good signal resolution and are suitable for long-time measurements. They enable easy measurement procedures, which can be used in every laboratory using small quantities of biological material, for pharmaceutical screening, drugs detection or tumors analyzing.

These sensors can be cleaned and sterilized even with hazardous procedures such as autoclaving or etching in hot alkali based solutions and are reusable without further conditioning procedures for in vivo measurements.

Outlook

This thesis can be considered as the first step for the coupling of AlGaN/GaN transistors with nerve cells. However, for a reliable operation of this coupling in further basic research or in applications such as drug screening, the following further steps are proposed.

A further improvement of the sensor chip is necessary to enhance its stability. Especially the passivation needs to be further developed. For example, the high moisture uptake of the polyimide passivation causes a signal drift, which should be reduced by replacement of polyimide or combination with other thin films.

Miniaturization and arrangement in arrays will enable higher resolved measurements.

For a better understanding of the chemical processes, which take place close to the sensor surface, and a deeper chemical analysis of the sensor active area before and after every measurement, further calibration experiments in defined electrolytes are necessary. By functionalization (for example ionophores) the ionic species, which contribute to the signal generation should be identified unambiguously.

Simulation of the sensor behavior in electrolytes can help to optimize the design (for example by proposing a transconductance or electron density in the 2DEG, see Fig. 7.19) and to define "critical" control experiments, where small changes of ionic concentration will cause a large effect in the sensor response.

Further experiments to analyze the proceeding biochemical reactions with other techniques are necessary (i.e. patch-clamp) to understand the underlying mechanisms.

The cell-transistor coupling experiments should be repeated to collect statistic data and performed in media with different ionic concentrations.

With the help of these improvements and further experiments, reliable models for the proceeding reactions can be developed, which finally opens the opportunity for the AlGaN/GaN biosensors to become a powerful tool in biological research of cell response and for drug screening.

Annexes

Annex 1: Processing steps for reported AlGaN/GaN structures
Annex 2: Technological steps
Annex 3: Polyimide passivation technology
Annex 4: Distribution of sensor structure on the wafer
Annex 5: DMEM cell media components
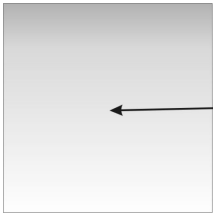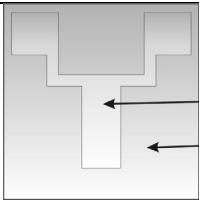Annex 6: NG 108-15 nerve cell protocol

Annex 1: Epitaxy and processing steps for reported AlGaN/GaN structures

	Detection	Structure	2DEG characteristic
1	anions (F⁻, Cl⁻) proteins	Al_2O_3 or (111) Si 3 µm GaN buffer 3 nm $Al_{0.3}Ga_{0.7}N$ 220 nm $Al_{0.3}Ga_{0.7}N$:Si cap layer	not specified
2	DNA		
3	PSA		
4	anions (Cl⁻, Br⁻, NO$_3^-$, SCN⁻)	Al_2O_3 substrate 2-3 µm GaN buffer AlGaN barrier	$N_s = 1.2 \times 10^{13}$ cm^{-2} $\mu = 900$ cm^2/Vs
5	cations (K⁺)		$N_s = 1.24 \times 10^{13}$ cm^{-2} $\mu = 1490$ cm^2/Vs
6	action potential	Al_2O_3 substrate 1.5 µm GaN buffer 24–26 nm AlGaN 3 nm GaN cap layer	$N_s = 1.2 \times 10^{13}$ cm^{-2} $\mu = 1240$ cm^2/Vs
7	penicillin	Al_2O_3 substrate 3.8 µm GaN buffer 20 nm $Al_{0.23}Ga_{0.77}N$ 3 nm GaN cap layer	$N_s = 1.1 \times 10^{13}$ cm^{-2} $\mu = 1400$ cm^2/Vs
8	extra-cellular potential	Al_2O_3 substrate 250 nm GaN buffer 13 nm AlGaN 2 nm GaN cap layer	$N_s = 6.4 \times 10^{12}$ cm^{-2} $\mu = 800$ cm^2/Vs
9	extra-cellular potential	Al_2O_3 substrate 2 µm GaN buffer 20 nm $Al_{0.3}Ga_{0.7}N$ 5 nm GaN cap layer	$N_s = 5 \times 10^{12}$ cm^{-2} $\mu = 580$ cm^2/Vs

	Growth	Ohm contacts	Passivation	Gate area	Ref.
1	MOCVD + MBE	Ti/Al/Pt/Ti 850°C anneal, 45 s in N_2 area 100 x 100 μm^2	Si_3N_4	100 x (5-40) μm^2	[98, 113]
2	MOCVD		500 nm PMMA	10 x 4 μm^2	[121]
3			400 nm PMMA	50 x 5 μm^2	[158]
4	MBE	Ti/Al/Ni/Au 800 °C anneal	polyimide	76 x 100 μm^2	[116]
5				100 x (10-100) μm^2	[113]
6	MOCVD	not specified	epoxy	35 x 35 μm^2	[19]
7	MOCVD	not specified	not specified	1.2 x 0.5 mm^2	[122]
8	MBE	Ti/Al/Ti/Au 750°C anneal, 60 s in N_2	polyimide	2400 x 500 μm^2	[147, 163]
9	MBE	Ti/Al 800°C anneal, 40 s	ceramic package	not specified	[164]

Annex 2: Technological steps

	technological process	
1	cleaning	
2	removing of Ti / Mo backside metallization from MBE sample	
3	lithography of adjusting marks	
4	Metallization adjusting marks	
5	lift off process	
6	Lithography mesa etching	
7	chlorine etching using ICP	
8	cleaning	

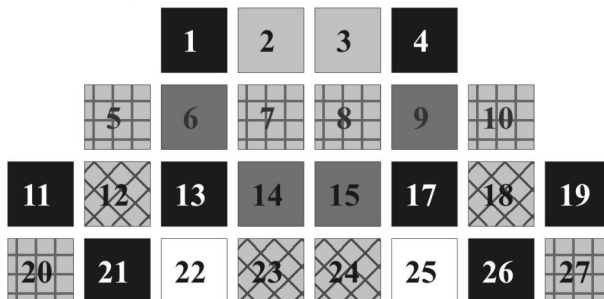|		details
1		in acetone, isopropanol and dry in Nitrogen flux
2		HNO$_3$ / 50% HF
3		spin coating standard photo resist AR-P3510, 4 s light exposure, developing with MIF (TMAH) AR 300-44
4		30 nm Ti /100 nm Al
5		in acetone, isopropanol and dry in Nitrogen flux
6		spin coating standard photo resist AR-P3510, 4 s light exposure, developing with MIF (TMAH) AR 300-44
7		130 nm GaN removed
8		in acetone, isopropanol and dry in Nitrogen flux

	technological process	
9	Lithography contact metallization	
10	contact metallization	
11	lift off process	
12	contact annealing	
13	Lithography contact pads	
14	Metallization contact pads	
15	Lithography contact passivation	
16	passivation deposition and curing	
17	Sawing into singles chips	
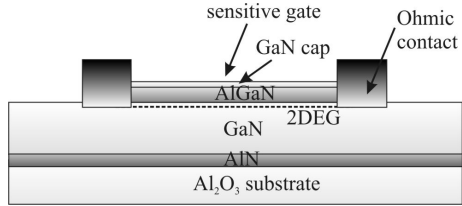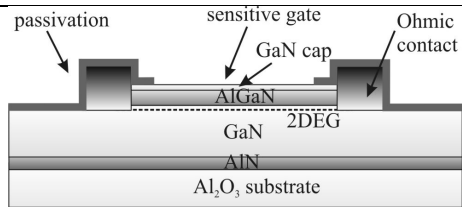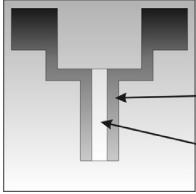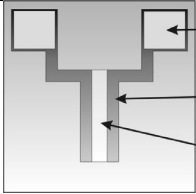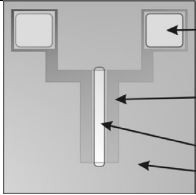
Figure (steps 9–10):
sensitive gate — GaN cap — Ohmic contact — AlGaN — 2DEG — GaN — AlN — Al$_2$O$_3$ substrate

Figure (steps 15–16):
passivation — sensitive gate — GaN cap — Ohmic contact — AlGaN — 2DEG — GaN — AlN — Al$_2$O$_3$ substrate

		details
9	Ohmic contact / sensitive gate	spin coating standard photo resist AR-P3510, 4 s light exposure, developing with MIF (TMAH) AR 300-44
10		20 nm Ti / 80 nm Al / 30 nm Ti / 100 nm Au
11		in acetone, isopropanol and dry in Nitrogen flux
12		40s at 800°C for MOCVD 60s at 750°C for MBE
13	contact pad / Ohmic contact / sensitive gate	spin coating standard photo resist AR-P3510, 4 s light exposure, developing with MIF (TMAH) AR 300-44
14		20 nm Ti / 300 nm Au
15	contact pad / Ohmic contact / sensitive gate passivation	spin coating standard photo resist AR-P3510, 4 s light exposure, developing with MIF (TMAH) AR 300-44
16		see annex 3
17		see annex 4

Annex 3: Polyimide passivation technology

1. Cleaning of the wafer using acetone, isopropanol and drying in nitrogen flux

2. Spin coating of primer VM651 (1000 ml deionized water + 1 ml VM651)
   a. 20 s hold
   b. 30 s spinning with 2800 rpm
   c. soft bake at 120°C on the hot blade for 60 s

3. Spin coating of polyimide PI 2610
   a. spinning 800 rpm for 10 s
   b. ramp to final spin speed 2800 rpm for 90 s
   c. soft bake at 130°C on the hot blade for 90 s

4. Spin coating of standard photo resist AR-P3510 and 4 s light exposure

5. 60 s developing with MIF (TMAH) AR 300-44 prepared 1:1.7 deionized water (= AR 300-49)

6. Cleaning with acetone, isopropanol and drying in nitrogen flux. The photo resist must be complet removed.

7. Curing base process
   a. loading of the wafer in programmable oven in air
   b. ramp to 200°C at a ramp rate of 4 K/min
   c. cure for 30 min at 200°C in normal atmosphere
   d. change to nitrogen atmosphere
   e. ramp to 350°C at a ramp rate of 2.5 K/min
   f. cure for 2 h at 350°C in nitrogen
   g. cool down at ambient

Annex 4: Distribution of sensor structure on wafer

MBE Waferlayout

MOCVD Waferlayout

■ 2400 x 400 µm²	■ (4x) 600 x 200 µm²
▦ 2400 x 100 µm²	▦ (4x) 40 x 35 µm²
▨ 500 x 400 µm²	▦ (4x) 250 x 35 µm²
▨ 400 x 100 µm²	□ Hall contacts (van der Pauw)

Annex 5: DMEM cell media components

(taken from Sigma-Aldrich protocol [234])

Component	D5280 [g/L]	
inorganic salts		
$CaCl_2 \cdot 2\ H_2O$	0.265	
$Fe(NO_3)_3 \cdot 9\ H_2O$	0.0001	
$MgSO_4$	0.09767	
KCl	0.4	
$NaHCO_3$		added 3.7[*)]
NaCl	6.4	
NaH_2PO_4	0.109	
succinic acid	0.075	
sodium succinate	0.1	
amino acids		
L-arginine $\cdot$ HCl	0.084	
L-cystine $\cdot$ 2 HCl	0.0626	
L-glutamine		added 0.584[*)]
glycine	0.030	
L-histidine $\cdot$ HCl $\cdot H_2O$	0.042	
L-isoleucine	0.105	
L-leucine	0.105	
L-lysine $\cdot$ HCl	0.146	
L-methionine	0.030	
L-phenylalanine	0.066	
L-serine	0.042	
L-threonine	0.095	
L-tryptophan	0.016	
L-tyrosine	0.072	
L-tyrosine $\cdot$ 2 Na $\cdot$ 2 H_2O	—	
L-valine	0.094	

[*)] $NaHCO_3$ and L-glutamine were added to DMEM immediately prior to the application

Component	D5280 [g/L]
vitamins	
choline bitartrate	0.072
choline chloride	—
folic acid	0.004
myo-inositol	0.0072
niacinamide	0.004
d-pantothenic acid • ½ Ca	0.004
pyridoxal • HCl	0.004
pyridoxine • HCl	—
riboflavin	0.0004
thiamine • HCl	0.004
other	
glucose	1.0
HEPES	—
Phenol Red • Na	0.0093
pyruvic acid • Na	0.11

Annex 6: NG 108-15 nerve cell protocol

Proliferation

ATCC advised growth medium: The base medium for this cell line is Dulbecco's Modified Eagle's Medium without sodium pyruvate but with 4 mM L-glutamine, 4.5 g/L glucose. To make the complete growth medium, it is necessary to add the following components to the base medium: 4.0 mg/L pyridoxine-HCl; 0.1 mM hypoxanthine; 400 nM aminopterin, and 0.016 mM thymidine; fetal calf serum to a final concentration of 10% and 1% penicillin / streptomicin.

Temperature: 37°C

Subculturing

Remove medium, and rinse with 0.25% trypsin, 0.03% EDTA solution.
Remove the solution and add an additional 1 to 2 ml of trypsin-EDTA solution.
Allow the flask to sit at room temperature (or at 37°C) until the cells detach.
Add fresh culture medium DMEM–high glucose supplemented with 10% FCS and 1% penicillin / streptomycin, aspirate and dispense into new culture flasks.

Subcultivation ratio: A subcultivation ratio of 1:6 to 1:10 is recommended.

Medium renewal: Every 2 to 3 days

Freeze medium: Complete growth medium, 92.5%; DMSO, 7.5%

Storage temperature: liquid nitrogen vapor phase

Recording medium

DMEM-high glucose supplemented with 10 % fetal calf serum and L-glutamine and 25 mM HEPES-TRIS add as buffer solution.

Acknowledgements

> ➤ Liele Costa Silveira and Andreea Dumitrescu for their assistance to perform selected measurements for this work.

I thank my parents to support our little family with love and patience to give me the possibility to continue this research after the birth of our children.

Last but not least I thank my husband Dr. Volker Cimalla for interesting and stimulating controversy, fine scientific ideas and permanent optimistic encouragement that made my little contribution to the big research field of biosensors possible. I'd like to thank him also for his help in English polishing and formatting this thesis.

References

[1]   Rogers, K.R., 1995, Biosens. Bioelectron., 10, 533.

[2]   Paddle, B.M., 1996, Biosens. Bioelectron., 11, 1079.

[3]   Ohlstein, E.H., Ruffolo, R.R., et al., 2000, Toxicology, 40, 177.

[4]   Heck, D.E., Roy, A., et al., 2001, Biolog. React. Intermed. 500, 709.

[5]   Croston, G.E., 2002, Trends in Biotech., 20, 110.

[6]   Fattinger, Ch., 2002, Carl Zeiss, Innovation 12.

[7]   Jorkasky, D.K., 1998, Toxicolog. Lett., 102–103, 539.

[8]   Kinter, L.B., Valentin, J.P., 2002, Fundam. Clin. Pharmacol., 16, 175.

[9]   Bousse, L., 1996, Sens. Actuat. B: Chem., 34, 270.

[10]   Bentleya, A., Atkinsona, A., et al., 2001, Toxicology: In Vitro, 15, 469.

[11]   Baeumner, A.J., 2003, Anal. Bioanal. Chem., 377, 434.

[12]   Fromherz, P., Offenhäusser, A., Vetter, T., Weiss, J., 1991, Science, 252, 1290.

[13]   Gross, G.W., Harsch, A., et al., 1997, Biosens. Bioelectron. 12, 373.

[14]   Denyer, M.C.T., Riehle, M., et al., 1998, Med. Biol. Eng. Comput., 36,638.

[15]   Jung, D.R., Cuttino, D.S., et al., 1998. J. Vac. Sci. Technol. A, 16, 1183.

[16]   Offenhäusser, A., Knoll, W., 2001, Trends in Biotech., 19, 62.

[17]   Krause, M., Ingebrandt, S., et al., 2000, Sens. Actuat. B: Chem., 70, 101.

[18]   Stett, A., Egert, U., et al., 2003, Anal. Bioanal. Chem., 377, 486.

[19]   Steinhoff G., Baur B., Wrobel G., Ingebrandt S., Offenhäusser A., Dadgar A., Krost A., Stutzmann M., and Eickhoff M., 2005, Appl. Phys. Lett., 86, 33901.

[20]   Hodgkin, A.L., Huxley, A. F., 1952, J. Physiol., 117, 500.

[21]   Neher, E., Sakmann, B., 1976, Nature, 260, 799.

[22]   Hamill, O.P., Marty, A., Neher, E., Sackman, B., Sigworth, F.J., 1981, Pflügers Archiv-European J. Physiol., 391, 2, 85.

[23]   Thomas, C.A., Springer, P.A., Loeb, G.E., Berwald-Netter, Y., Okun, L.M., 1972, Exp. Cell Res., 74, 61.

[24]   Gross, G.W., Rieske, E., Kreutzberg, G.W., Meyer, A., 1977, Neurosci. Lett., 6, 101-105.

[25] Pine, J., 1980. J. Neurosci. Meth., 2, 19.

[26] Novak, J.L. and Wheeler, B.C., 1986, IEEE Trans. Biomed. Eng., BME, 33, 196.

[27] Drodge, M.H., Gross, G.W., Hightower, M.H. and Czisny, L.E., 1986, J. Neurosci. Meth., 6, 1583.

[28] Eggers, M.D., Astolfi, D.K., Liu, S., Zeuli, H.E., Doeleman, S.S., McKay, R., Khuon, T.S. and Ehrlich, D.J., 1990, J. Vac. Sci. Technol. B, 8, 1392.

[29] Martinoia, S., Bove, M., Carlini, G., Ciccarelli, C., Grattarola, M., Storment, C. and Kovacs, G., 1993, J. Neurosci. Meth., 48, 115.

[30] Maeda, E., Robinson, H.P.C. and Kawana, A., 1995, J. Neurosci., 15, 6834.

[31] Fromherz, P., Müller, C.O., and Weis, R., 1993, Phys. Rev. Lett., 71, 4079.

[32] Fromherz, P., and Stett, A., 1995, Phys. Rev. Lett., 75, 1670.

[33] Bergveld, P., 1970, IEEE Trans. Biomed. Eng., 17, 70.

[34] Bergveld, P., 2003, Sens. and Actuat. B, 88, 1.

[35] Schöning, M. J., and Poghossian, A., 2002, Analyst, 127, 1137.

[36] Schöning, M. J., and Poghossian, A., 2006, Electroanal., 18, 1893.

[37] Madou, M. J., 1989, Academic Press, Boston.

[38] Neuberger, R., Müller, G., Ambacher, O., and Stutzmann, M., 2001, phys. stat. sol. (a), 183, R10.

[39] Eickhoff, M., Schalwig, J., Steinhoff, G., Weidemann, O., Görgens, L., Neuberger, R., Hermann, M., Baur, B., Müller, G., Ambacher, O., and Stutzmann, M., 2003, phys. stat. sol. (c), 0, 1908.

[40] Pearton, S. J., Kang, B. S., Kim, S., Ren, F., Gila, B. P., Abernathy, C. R., Lin, J., and Chu S. N. G., 2004, J. Phys.: Cond. Matter, 16, R961.

[41] Steinhoff, G., Hermann, M., Schaff, W. J., Eastman, L. F., Stutzmann, M., and Eickhoff, M., 2003, Appl. Phys. Lett., 83, 177.

[42] Kittler G., 2008, PhD Thesis, Technical University Ilmenau.

[43] Becker, W., Deamer, D., 1991, The world of the cell, The Benjamin/Cummings Publishing Company, Inc.

[44] Kandel, E. R., Schwartz J. H., Jessel T. M., 2000, Principles of neural science, McGraw – Hill Companies, Inc.

[45] Raven, P., and Johnson, G., Biology of the cell, 2001, McGraw-Hill, 6th edition.

[46] Faller, A., Schünke, M., Schünke, G., 2004, Stuttgart: Thieme.

[47] Brown, A.G., Nerve cells and nervous systems: an introduction to neuroscience, 2001, Springer – Verlag London Limited.

[48] Hille, B., Ionic channels of excitable membranes, 1991, Sinauer Associates, Inc.

[49] Hammond, C., Cellular and molecular neurobiology, 2001, Academic Press.

[50] Vogel, G., Angermann H., 2002, Munich: Dt. Taschenbuch- Verl.

[51] Webster, R. A., Neurotransmitters, drugs and brain function, 2001, John Wiley & Sons Ltd., Baffins Lane, Chichester, West Sussex PO19 1UD, UK.

[52] Han, B.S., Hong , H-S., Choi Won – Seok., Markelonis, G. J., Oh Tae, H., Oh Young, J., 2003, J. Neurosci., 23, 5069.

[53] Olivera-Bravo, S., Ivorra, I., Morales, A., 2005, Brit. J. Pharmacol., 144, 88.

[54] Du, D., Huang X., Cai J., Zhang A., 2007, Biosens. Bioelectron., 23, 285.

[55] Brenner, G. M., 2000, Pharmacology. Philadelphia, PA: W.B. Saunders Company.

[56] Juza, R. and Hahn, H., 1938, Z. Anorg. Allgem. Chem., 239, 234.

[57] Grimmeiss, H. G., and Koelmans, H., 1959, Z. Naturfor., 14a, 264.

[58] Maruska, H. P., Tietjen, J. J., 1969, Appl. Phys. Lett., 15, 327.

[59] Lorenz, M. R., and Binkowski, B.B., 1962, J. Electrochem. Soc., 109, 24.

[60] Kosicki B. B. and Kahng D., 1969, J. Vac. Sci. Technol., 6, 593.

[61] Khan, M.A., Skogman, R. A., Schulze, R. G., Gershenzon, M., 1983, Appl. Phys. Lett., 42, 430.

[62] Yoshida, S., Miswa, S., Gonda, S., 1983, J. Vac. Sci. Technol. B, 1, 250.

[63] Yoshida, S., Miswa, S., Gonda, S., 1983, Appl. Phys. Lett., 42, 427.

[64] Maruska, H. P., Rhines, W. C., and Stevenson, D.A., 1972, Mater. Res. Bull., 7, 777.

[65] Amano, H., Kitoh, M., Hiramatsu, K., Akasaki, I., 1990, J. Electrochem. Soc., 137, 1639.

[66] Nakamura, S., Iwasa, N., Senoh, M., and Mukai, T., 1992, Jap. J. Appl. Phys., 31, 1258.

[67] Ambacher, O., 1998, J. Phys. D: Appl. Phys., 31, 2653.

[68] Pearton, S. J., Zolper, J. C., Shul, R. J., and Ren, F., 1999, J. Appl. Phys., 86, 1.

[69] Cimalla, V., Förster, Ch., Kittler, G., Cimalla, I., Kosiba, R., Ecke, G., Ambacher, O., Goldhahn, R., Shokhovets, S., Georgakilas, A., Lu, H., and Schaff, W., 2003, phys. stat. sol. (c) 0, 2818.

[70] Piprek, J., Nitride semiconductor devices, 2007, WILEY-VCH, GmbH & Co. KGaA.

[71] Lebedev, V., Cimalla, I., Cimalla, V., Wagner, R., Kaiser, U., and Ambacher, O., 2005, phys. stat. sol. (c) 2, 1360.

[72] Lebedev, V., Cimalla, I., Kaiser, U., and Ambacher, O., 2004, phys. stat. sol. (c) 1, 233.

[73] Cherkashinin, G., Lebedev, V., Wagner, R., Cimalla, I., and Ambacher, O., 2006, phys. stat. sol. (c), 243, 1713.

[74] Lebedev, V., Cherkashinin, G., Ecke, G., Cimalla, I., and Ambacher, O., 2007, J. Appl. Phys., 101, 033705.

[75] Bindra, A., and Valentine, M., 2007, RFDESIGN, 18.

[76] Cimalla, I., Foerster, Ch., Cimalla, V., Lebedev, V., Cengher, D., and Ambacher, O., 2003, phys. stat. sol (c) 0, 3767.

[77] Young, T.-H., and Chen, C.-R., 2006, Biomater., 27, 3361.

[78] Cimalla, I., Will, F., Tonisch, K., Niebelschütz, M., Cimalla, V., Lebedev, V., Kittler, G., Himmerlich, M., Krischok, S., and Schaefer, J. A., Gebinoga, M., Schober, A., and Ambacher, O., 2007, Sensors and Actuators B, 123, 740.

[79] Steinhoff, G., Purrucker, O., Tanaka, M., Stutzmann, M., and Eickhoff, M., 2003, Adv. Funct. Mater., 13, 841.

[80] Wong, K.-Y., Tang, W., Lau, K. M., and Chen, K. J., 2007, Appl. Phys. Lett., 90, 213506.

[81] Morkoç, H., 1999, Springer-Verlag, Berlin, Heidelberg, New York.

[82] Bernardini, F., and Fiorentini, V., 1997, Phys. Rev. B., 56, R10 024.

[83] Ambacher, O., Majewski, J., Miskys, C., Link, A., Hermann, M., Eickhoff, M., Stutzmann, M., Bernardini, F., Fiorentini, V., Tilak, V., Schaff, B., and Eastman, L. F., 2002, J. Phys.: Condens. Mat., 14, 3399.

[84] Ambacher, O., Smart, J., Shealy, J. R., Weimann, N. G., Chu, K., Murphy, M., Schaff, W. J., Eastman, L. F., Dimitrov, R., Wittmer, L., Stutzmann, M., Riegwer, W., and Hilsenbeck, J., 1999, J. Appl. Phys., 85, 3222.

[85] Lee, S. R., Wright, A. F., Crawford, M. H., Petersen, G. A., Han J., Bielfeld, R. M., 1999, Appl. Phys. Lett., 74, 3344.

[86] Hellman, E. S., 1998, Mater. Res. Soc. Int. J. Nitride Semicond. Res., 3, 11.

[87] Visconti, P., Huang, D., Reshchikov, M. A., Yun, F., King, T., Baski, A. A., Cingolani, R., Litton, C. W., Jasinski, J., Liliental-Weber, Z., and Morkoc, H., 2001, phys. stat. sol. (b), 228, 513

[88] Yang, W.-C., Rodriguez, B. J., Park, M., Nemanich, R. J., Ambacher, O., and Cimalla, V., 2003, J. Appl. Phys., 94, 5720.

[89] Niebelschütz, M., Ecke, G., Cimalla, V., Tonisch, K., and Ambacher, O., 2006, J. Appl. Phys., 100, 074909.

[90] Weyher, J. L., Müller, S., Grzegory, I., and Porowski, S., 1997, J. Cryst. Growth 182, 17.

[91] Kazimirov, A., Scherb, G., Zegenhagen, J., Lee, T-L., Bedzyk, M. J., Kelly, M. K., Angerer, H., and Ambacher, O., 1998, J. Appl. Phys., 84, 1703.

[92] Brunner, D., Angerer, H., Bustarret, E., Freudenberg, F., Hopler, R., Dimitrov, R., Ambacher, O., Stutzmann, M., 1997, J. Appl. Phys., 82, 5090.

[93] Bernardini F. and Fiorentini V, 2001, Phys. Rev. B., 64, 85207.

[94] Lebedev, V., Tonisch, K., Niebelschütz, F., Cimalla, V., Cengher, D., Cimalla, I., Mauder, Ch., Hauguth, S., Morales, F. M., Lozano, J. G., and González, D. and Ambacher, O., 2007, J. Appl. Phys., 101, 054906.

[95] Ibbetson, J. P., Fini, P. T., Ness, K. D., DenBaars, S. P., Speck, J. S., Mishra, U. K., 2000, Appl. Phys. Lett., 77, 250.

[96] Jogai, B., 2003, J. Appl. Phys., 93, 1631.

[97] Madou, M. J., 1989, Academic Press, Boston.

[98] Kang, B. S., Ren, F., Kang, M. C., Lofton, C., Tan, W., Pearton, S. J., Dabiran, A., Osinsky, A., and Chow, P. P., 2005, Appl Phys. Lett., 86, 173502.

[99] Neuberger, R., Müller, G., Ambacher, O., and Stutzmann, M., 2001, phys. stat. sol. (a), 185, 85.

[100] Mehandru, R., Luo, B., Kang, B. S., Kim, J., Ren, F., Pearton, S. J., Pan, C.-C., Chen, G.-T., and Chyi, J.-I., 2004, Sol. State Electron., 48, 351.

[101] Kokawa, T., Sato, T., Hasegawa, H., and Hashizume, T., 2006, J. Vac. Sci. Technol. B, 24, 1972.

[102] Kang, B. S., Louche, G., Duran, R. S., Gnanou, Y., Pearton, S. J., and Ren, F., 2004, Sol. State Electron., 48, 851.

[103] Lide, D. R., 2003, CRC handbook of chemistry and physics, 84th ed., CRC Press, Boca Raton.

[104] Bergveld, P., 2003, IEEE Sens. Conf., Toronto

[105] Bousse, L., Rooij, N. F. de, and Bergveld, P., 1983, IEEE Trans. Electron. Dev., 30, 1263.

[106] Yates, D. E., Levine, S., and Healy, T. W., 1974, J. Chem. Soc., Faraday Trans. 1, 70, 1807.

[107] Bayer, M., Uhl, C., and Vogl, P., 2005, J. Appl. Phys., 97, 33703.

[108] Kocan, M., Rizzi, A., Lüth, H., Keller, S., and Mishra, U. K., 2002, phys. stat. sol. (b), 234, 733.

[109] Siu W. M., and Cobbold R. S. C., 1979, IEEE Trans. Electron. Dev., 26, 1805.

[110] Fung C. D., Cheung P. W., and Ko W. H., 1986, IEEE Trans. Electron. Dev., 33, 8.

[111] Ambacher, O., and Cimalla, V., Springer, New York, 2008, 27.2008, in: "Polarization Effects in Semiconductors: From Ab Initio to Device Application" (eds. C. Wood and D. Jena), Springer, New York, 2008, p. 27.

[112] Spitznas, A., 2005, Diploma Thesis, Technical University Ilmenau.

[113] Alifragis, Y., Volosirakis, A., Chaniotakis, N. A., Konstantinidis, G., Adikimenakis, A., and Georgakilas, A., 2007, Biosens. Bioelectron., 22, 2796.

[114] Chaniotakis, N. A., Alifragis, Y., Konstantinidis, G., and Georgakilas, A., 2004, Analytical Chemistry, 76, 5552.

[115] Alifragis, Y., Konstantinidis, G., Georgakilas, A., and Chaniotakis, N. A., 2005, Electroanal., 17, 527.

[116] Alifragis, Y., Georgakilas, A., Konstantinidis, G., Iliopoulos, E., Kostopoulos, A., and Chaniotakis, N. A., 2005, Appl. Phys. Lett., 87, 253507.

[117] Linkohr, Sth., 2008, Diploma Thesis, Technical University Ilmenau.

[118] Costa Silveira, L., 2008, Diploma Thesis, Technical University Ilmenau.

[119] Jain S., Willander M., Narayan J., and van Overstraeten R., 2000, J. Appl. Phys., 87, 965.

[120] Kang, B. S., Ren, F., Wang, L., Lofton, C., Tan, W. W., Pearton, S. J., Dabiran, A., Osinsky, A., and Chow, P. P., 2005, Appl. Phys. Lett., 87, 23508.

[121] Kang, B. S., Pearton, S. J., Chen, J. J., Ren, F., Johnson, J. W., Therrien, R. J., Rajagopal, P., Roberts, J. C., Piner, E. L., and Linthicum, K. J. et al., 2006, Appl. Phys. Lett., 89, 122102.

[122] Baur, B., Howgate, J., Ribbeck, H.-G. von, Gawlina, Y., Bandalo, V., Steinhoff, G., Stutzmann, M., and Eickhoff, M., 2006, Appl. Phys. Lett., 89, 183901.

[123] Binari S., Dietrich H., Kelner G., Rowland L., Doverspike K., and Wickenden D., 1995, J. Appl. Phys., 78, 3008.

[124] Tilak, V., 2002, PhD Thesis, Cornell University.

[125] Tonisch, K., 2005, Diploma Thesis, Technical University Ilmenau.

[126] Motayed, A., Bathe, R., Wood, M. C., Diouf, O. S., Vispute, R. D., and Mohammad, S. N., 2003, J. Appl. Phys., 93, 1087.

[127] Bardwell, J. A., Ying, Liu, Rauhala, S., Bouwhuis, P., Marshall, P., Tang, H., and Webb, J. B., 2001, phys. stat. sol. (a), 188, 389.

[128] Fay, M. W., Moldovan, G., Brown, P. D., Harrison, I., Birbeck, J. C., Hughes, B. T., Uren, M. J., and Martin, T., 2002, J. Appl. Phys., 92, 94.

[129] Maroldt, St., 2006, work project, Technical University Ilmenau.

[130] Bright, A.N., Thomas, P. J., Weyland, D. M., Tricker, C. J., Humphreys, and Davies, R., 2001, J. Appl. Phys., 89, 3143.

[131] Khan, M. A., Shur, M. S., and Chen, Q., 1996, Appl. Phys. Lett., 68, 3022.

[132] Microelectrode array (MEA) user manual, 2005, Reutlingen, Germany.

[133] Lee Kee-Keun, He J., Singh A., Massia St., Ehteshami Gh., Kim B., and Raupp Gr., 2004, J. Micromech. Microeng., 14, 32.

[134] "Pyralin LX-Series",1996-2005, Produktinformation DuPont United Kingdom, Ltd.

[135] Hintz, M., 2007, PhD Thesis, Technical University Ilmenau.

[136] "Green Tape® material system", 1996 - 2005, Produktinformation DuPont United Kingdom, Ltd.

[137] L. J. van der Pauw, 1958, Philips Res. Repts, 13, 1-9.

[138] Polyakov, V. M. and Schwierz, F., 2007, J. Appl. Phys., 101, 033703.

[139] Price, P.J. and Stern, F., 1983, Surf. Sci. 132, 577.

[140] Geitz, C., 2007, Diploma Thesis, Technical University Ilmenau.

[141] Nic, M., Jirat, J., and Kosata, B., IUPAC Compendium of Chemical Terminology, http://goldbook.iupac.org/index.html (accessed Nov 02, 2007).

[142] Olmsted, J. III, and Williams, G. M., 1997, Wm. C. Brown Publishers, USA.

[143] Minuth, W.W., Strehl, R., Schumacher, K., 2002, Pabst Science Publishers.

[144] http://www.fermentas.com/catalog/electrophoresis/topvisionagarle.htm

[145] Maroldt, St., 2007, Diploma Thesis, Technical University Ilmenau.

[146] Kerekes, T., 2005, work project, Technical University Ilmenau.

[147] Cimalla, V., Lebedev, V., Linkohr, S., Cimalla, I., Lübbers, B., Tonisch, K., Brückner, K., Niebelschütz, F., and Ambacher, O., 2008, 17th European Workshop on Heterostructure. Technology, Venice, Italy, November 3-5, 2008, p. 33.

[148] Cimalla, I., Lübbers, B., Cimalla, V., Gebinoga, M, Schober, A., and Ambacher, O., "Advanced Semiconductor Materials and Devices Research: III-Nitrides and SiC", (ed. Ho-Young Cha), Research Signpost Publishers, Trivandrum, India, in press.

[149] Wang, Hung-Ta, Kang, B. S., Chancellor, T. F., Jr., Lele, T. P., Tseng, Y., Rena F., Pearton S. J., Johnson, W. J., Rajagopal, P. J., Roberts, C., Piner, E. L.,and Linthicum K. J., 2007, Appl. Phys. Lett., 91, 042114.

[150] Bermudez, V., 2002, Surface Science, 499, 109.

[151] Bermudez, V., 2002, Surface Science, 499, 124.

[152] Petoral, R., JR., Yazdi, G., Spetz, A., Yakimova, R., and Uvdal, K. 2007, Appl. Phys. Lett., 90, 223904.

[153] Simpkins, B., McCoy, K., Whitman, L., and Pehrsson, P. 2007, Nanotechnol., 18, 355301.

[154] Yakimova, R., Steinhoff, G., Petoral, R. M., Jr., Vahlberg, C., Khranovskyy, V., Yazdi, G. R., Uvdal, K., and Lloyd Spetz, A. 2007, Biosens. Bioelectron., 22, 2780.

[155] Kim, H., Colavita, P. E., Metz, K. M. Nichols, B. M., Bin Sun, Uhlrich, J., Wang, X., Kuech, Th. F., and Hamers R. J., 2006, Langmuir, 22, 8121.

[156] Linkohr, S., Lübbers, B., Nebel, Ch., Lebedev, V., Raynor, B., Leuther, A., Cimalla, V., and Ambacher, O., International Congress

Nanotechnolgy in medicine and biology, 26-27. January, 2009, Krems, Austria.2009.

[157] Wang, Yu-Lin., Chu, B. H., Chen, K. H., Chang, C. Y., Lele, T. P., Tseng, Y., Pearton, S. J., Ramage, J., Hooten, D., Dabiran, A., Chow, P. P., and Ren F., 2008, Appl Phys. Lett., 93, 262101.

[158] Baur, B., Steinhoff, G., Hernando, J., Purrucker, O., Tanaka, M., Nickel, B., Stutzmann, M., and Eickhoff, M. 2005, Appl. Phys. Lett., 87, 263901.

[159] Kang, B., Wang, H., Lele, T., Tseng, Y., Ren, F., Pearton, S., Johnson, J., Rajagopal, P., Roberts, J., and Piner, E, and Linthicum, K. J. et al. 2007, Appl. Phys. Lett., 91, 112106.

[160] Kang, B. S., Wang, H. T., Ren, R F., Pearton, S.J., Morey, T.E., Dennis, D. M., Johnson, P.J., Rajagopal, P., Roberts, J., Piner, E, and Linthicum, K. J., 2007, Appl. Phys. Lett., 91, 252103.

[161] Chu, B. H., Kang, B. E., Ren, F., Chang, C. Y., Wang, Y. L., Pearton, S. J., Glushakov, A. V., Dennis, D. M., Johnson, J. W., Rajagopal, P., Roberts, J. C., Piner, E. L., and Linthicum, K. J. 2008, Appl. Phys. Lett., 93, 042114 2008.

[162] Young, T.-H., and Chen, C.-R. 2006, Biomater., 27, 3361.

[163] Gebinoga, M., Cimalla, I., Silveira, L., Klett, M., Lebedev, V., Tonisch, K., Will, F., Ambacher, O., and Schober, A. 2008, Sensors for Environment, Health and Security - Advanced Materials and Technologies" (ed. M.-I. Baraton), Springer, Dordrecht, Netherlands, 2008, pp 311-316.

[164] Yu, J., Jha, S. K., Xiao, L., Liu, Q., Wang, P., Surya, C., and Yang, M. 2007, Biosens. Bioelectron., 23, 513.

[165] Prabhakaran, K., Andersson, T., and Nozawa, K. 1996, Appl. Phys. Lett., 69, 3212.

[166] Eickhoff, M., Neuberger, R., Steinhoff, G., Ambacher, O., Müller, G., and Stutzmann, M. 2001, phys. stat. sol. (b), 228, 519.

[167] Buchheim, C., Kittler, G., Cimalla, V., Lebedev, V., Fischer, M., Krischok, S., Yanev, V., Himmerlich, M., Ecke, G., Schaefer, J. A., 2006, IEEE Sens. J., 6, 881.

[168] Kokawa, T., Sato, T., Hasegawa, H., and Hashizume, T., 2006, J. Vac. Sci. Technol. B, 24, 1972.

[169] Lide, D. R., 2003, CRC Press, Boca Raton.

[170] Stocker, D.A., Schubert, E.F., Redwing, J.M., 1998, Appl. Phys. Lett., 73, 2654.

[171] Zhuang, D., Edgar, J.H., 2005, Mater. Sci. Eng. R48, 1-46.

[172] Zhu, K., Kuryatkov, V., Borisov, B., Kipshidze, G., 2002, Appl. Phys. Lett., 81, 4688.

[173] Cho, H., Hahn, Y.-B., Hays, D.C., Abernathy, C.R., 1999, J. Vac. Sci. Technol., A 17, 2202.

[174] Foerster, Ch., Cimalla, V., Brueckner, K., Lebedev, V., Stephan, R., Hein, M., and Ambacher, O., 2005, phys. stat. sol. (a) 202, 671.

[175] Tracy, K.M., Mecouch, W.J., Davis, R.F., Nemanich, R.J., 2003, J. Appl. Phys. 94, 3163.

[176] Widstrand, S.M., Magnusson, K.O., Johansson, L.S.O., Moons, E., Gurnett, M., Oshima, M., 2005, MRS Internet J. Nitride Semicond. Res. 10, 1.

[177] Hasegawa, H., Koyama, Y., Hashizume, T., 1999, Jpn. J. Appl. Phys. Part 1, 38, 2634.

[178] Li, D., Sumiya, M., Fuke, S., Yang, D., Que, D., Suzuki, Y., Fukuda, Y., 2001, J. Appl. Phys., 90, 4219.

[179] Hashizume, T., Hasegawa, H., 2004, Appl. Surf. Sci. 234, 387.

[180] Schober, A., Kittler, G., Buchheim, C., Ali, M., Cimalla, V., Fischer, M., Yanev, V., Himmerlich, M., Krischok, S., and Schaefer, J. A., Romanus, H., Sändig, T., Burgold, J., Weise, F., Wurmus, H., Drüe, K.H., Hintz, M., Thust, H., Gebinoga, M., Kittler, M., Spitznas, A., Gottwald, E., Weibezahn, K-F., Wegener, D., Schwienhorst, A., and Ambacher, O. 2005, Techn. Proc. 2005 Nanotechnol. Conf. Trade Show, Taylor & Francis, Boca Raton, 489.

[181] Schober, A., Kittler, G., Lübbers, B., Buchheim, C., Ali, M., Cimalla, V., Fischer, M., Spitznas, A., Gebinoga, M., and Yanev, V. et al., 2005, Proc. 7. Dresdener Sensor-Symposium, TUD Press, Dresden, 143.

[182] Kittler, G., Spitznas, A., Luebbers, B., Lebedev, V., Wegener, D., Schober, A., Gebinoga, Schwierz, F., Polyakov, V., Weise, F., and Ambacher, O. 2006, 51st Internat. Wiss. Kolloq., Technische Universität Ilmenau, September 11-15, 2006, 4-4-4.

[183] Kittler, G., Spitznas, A., Luebbers, B., Lebedev, V., Wegener, D., Gebinoga, M., Weise, F., Schober, A., and Ambacher, O. 2007, Mater. Res. Soc. Symp. Proc., 955, I14.

[184] Van der Wal, P. D., Skowronska-Ptasinska, M., Van den Berg, A., Bergveld, P., Sudholter, E. J., and Reinhoudt, D. N., 1990, Analytica Chimica Acta, 231, 41.

[185] Brunink, J. A., Haak, J. R., Bomer, J. G., Reinhoudt, D. N., McKervey, M., and Harris, S. J. 1991, Analytica Chimica Acta, 254, 75.

[186] Alifragis, Y., Chaniotakis, N. A., Konstantinidis, G., Volosirakis, A., Adikimenakis, A., and Georgakilas, A., 2006, E-MRS Spring Meeting, Nice

[187] Alifragis, Y., Volosirakis, A., Chaniotakis, N. A., Konstantinidis, G., Iliopoulos, E., and Georgakilas, A., 2007, phys. stat. sol. (a), 204, 2059.

[188] Kang, B. S., Suku Kim, Ren, F., Gila, B. P., Abernathy, C. R., and Pearton, S. J., 2005, Sensors Journal, IEEE, 5, 677.

[189] Ozasa, K., Nemoto, S., Hara, M., and Maeda, M., 2006, phys. stat. sol. (a), 203, 2287.

[190] Kemeny, D. M., 1991, Pergamon Press, Oxford.

[191] Bergveld, P., 1996, Sens. Actuat. A, 56, 65.

[192] Clark, L. C., and Lyons, C., 1962, Ann. N. Y. Acad. Sci., 102, 29.

[193] Caras, S., and Janata, J. 1980, Anal. Chem., 52, 1935.

[194] Lübbers, B., Kittler, G., Ort, P., Linkohr, S., Wegener, D., Baur, B., Gebinoga, M., Weise, F., Eickhoff, M., Maroldt, S., Schober, A., and Ambacher, O., 2008, phys. stat. sol. (c), 5, 2361.

[195] Ingebrandt, S., Han, Y., Nakamura, F., Poghossian, A., Schoning, M. J., and Offenhausser, A., 2007, Biosens. Bioelectron., 22, 2834.

[196] Souteyrand, E., Cloarec, J. P., Martin, J. R., Wilson, C., Lawrence, I., Mikkelsen, S., and Lawrence, M. F., 1997, J. Phys. Chem. B, 101, 2980.

[197] Mohan, D. K., Molnar, P., and Hickman, J. J., 2006, Biosens. Bioelectron., 21, 1804.

[198] Heer, F., Franks, W., Blau, A., Taschini, S., Ziegler, C., Hierlemann, A., and Baltes, H., 2004, Biosens. Bioelectron., 20, 358.

[199] Offenhäusser, A., Sprossler, C., Matsuzawa, M., and Knoll, W., 1997, Biosens. Bioelectron., 12, 819.

[200] Lehmann, M., Baumann, W., Brischwein, M., Gahle, H.-J., Freund, I., Ehret, R., Drechsler, S., Palzer, H., Kleintges, M., and Sieben, U. et al., 2001, Biosens. Bioelectron., 16, 195.

[201] Freshney, R. I., 2005, Culture of Animal Cells: A Manual of Basic Technique, John Wiley & Sons, Inc.

[202] Minuth, W.W., Strehl R., Schumacher K., 2002, Pabst Science Publishers.

[203] www.atcc.org

[204] Borkholder, D.A., 1998, PhD Thesis, Stanford University USA.

[205] Imanishi Takashi, Matsushima Kayoko, Kawaguchi Akinori, Wada Tetsuyuki, Masuko Takashi, Yoshida Shigeru, Ichida Seiji, 2006, Biol. Pharm. Bull., 29, 701.

[206] Krystosek, A., 1985, J. Cell. Physiol., 125, 319.

[207] Ma, Wu, Joseph, J. Pancrazio, J. J., Margaret, Coulombe, M., Judith, Dumm J., RamaSri Sathanoori, R., Jeffery, L. Barker J.L., Vijay, C. Kowtha, V.C., David, A. Stenger, D.A., James, J. Hickman, J.J., 1998, Developmental Brain Research, 106,155.

[208] Seidman, K. J. N., Barsuk, J. H., Johnson, R. F., Weyhenmeyer, J. A., 1996, J. Neurochem., 66, 1011.

[209] Goshima, Y., Ohsako, S., Yamauchi, T., 1993, J. Neurosci., 13, 559.

[210] Rouzaire-Dubois, B., and Dubois, J.M., 2004, Gen. Physiol. Biophys., 23, 231.

[211] Chen, Xiao - Liang, Zhong, Zhen-Guo, Yokoyama, Shigeru, Bark, Ch., Meister, B., Berggren, Per-Olof, Roder, J., Higashida, Haruhiro and Jeromin, A., 2001, J. Physiol., 532.3,649.

[212] Schmitt, H., Meves, H., 1995, J. Physilogy, 89, 181.

[213] Schmitt, H., Meves H., 1995, J. Membrane Biol., 145, 233.

[214] Schäfer, S., Béhé, Ph., Meves, H., 1991, Pflügers Arch 418, 581.

[215] Chin, T.-Y., Hwang, HM., Chueh, Sh.-H., 2002, Mol. Pharmacol., 61, 486.

[216] Chau, L.-Y., Lin, T. A., Chang, W.- T., Chen, C.-H., Shue, M. –J., Hsu, Y.- S., Hu, C.- Y., Tsai, W.-H., Sun, G. Y., 1993, J. Neurochem , 60, 454.

[217] Hsu, L. - S., Chou, W.-Y., Chueh, Sh.-H., 1995, J. Biochem., 309, 445.

[218] Mima, K., Donai, H., Yamauchi, T., 2002, Biol. Proced. Online, 3, 79.

[219] Spilker, C., Gundelfinger, E.D., Braunewell, K.-H., 2002, Biochim. Biophys. Acta 1600, 118.

[220] Mohan, D. K., Molnar, P., Hickman, J. J., 2006, Biosens. Bioelectron., 21, 1804.

[221] Yano, K., Higashida, H., Inoue, R., Nozawa, Y., 1984, J. Biol. Chem., 259, 10201.

[222] Zhang, B.-F., Peng, F.-F., Zhang, J.-Z., Wu D.-C., 2003, Acta Pharmacol. Sin. 24, 663.

[223] Kugawa, F., Arae, K, Ueno, A, Aoki, M., 1998, Eur. J. Pharmacol. 347,105.

[224] Nelson, Ph., Christian, C., Nirenberg, M., 1976, Proc. Nat. Acad. Sci. USA, 73, 123.

[225] Shimohira-Yamasaki, M., Toda, S., Narisawa, Y., Sugihara, H., 2006, Cell structure and function, 31, 39.

[226] Roy, C.Y. Choi, San Pun, Tina, T.X. Dong, David, C.C. Wan, Karl W.K. Tsim, 1997, Neurosci. Lett., 236, 167.

[227] Sprössler, Ch., Richter, D., Denyer, M., Offenhäusser, A., 1998, Biosens. Bioelectron., 13, 613.

[228] Ingebrandt, S., 2001, PhD Thesis, Johannes Gutenberg-Universität Mainz.

[229] Schmidtner, M., Fromherz, P., 2006, Biophys. J. 90,183.

[230] ECACC Handbook, SIGMA, Cell culture.

[231] Kao, K., Ross, J.S., Albee, A., Goodnight, D. M., Fuhr, B., Caple, M. V., Sigma – Aldrich Corporation, USA.

[232] Braun, D., and Fromherz, P., 1998, Phys. Rev. Lett., 81, 5241.

[233] Corry, B., 2006, Mol. BioSyst., 2, 527.

[234] Dulbecco, R. and Freeman, G., 1959, Virology, 8, 396.

[235] Polyakov, V. M. Schwierz, F., Cimalla, I. Kittler, M. Lübbers, B. and Schober, A., 2009, J. Appl. Phys., 106, 023715.

[236] Polyakov, V. M., private communication.

List of publications

Published in Journals

[1]   V. Cimalla, Ch. Förster, G. Kittler, I. Cimalla, R. Kosiba, G. Ecke, O. Ambacher, R. Goldhahn, S. Shokhovets, A. Georgakilas, H. Lu, and W.J. Schaff: „Correlation between strain, optical and electrical properties of InN grown by MBE", phys. stat. sol. (c) 0 (2003) 2818-2821.

[2]   S. Krischok, V. Yanev, O. Balykov, M. Himmerlich, J.A. Schaefer, R. Kosiba, G. Ecke, I. Cimalla, V. Cimalla, O. Ambacher, H. Lu, W.J. Schaff, and L.F. Eastman: "Investigations of MBE grown InN and the influence of sputtering on the surface composition", Surf. Sci. 566-568 (2004) 849-855.

[3]   V. Cimalla, U. Kaiser, I. Cimalla, G. Ecke, J. Pezoldt, L. Spiess, O. Ambacher, H. Lu, and W.J. Schaff: "Cubic InN on r-plane sapphire", Superlattices and Microstructures 36 (2004) 487-495.

[4]   V. Lebedev, I. Cimalla, V. Cimalla, R. Wagner, U. Kaiser, and O. Ambacher: "Defect related absorption and emission in AlGaN solar-blind UV photodetectors", phys. stat. sol (c) 2 (2005) 1360-1365.

[5]   V. Lebedev, I. Cimalla, U. Kaiser, O. Ambacher: "Gap state absorption in AlGaN photoconductors and solar-blind photodetectors", physica status solidi (c) 1 (2004) 233-237.

[6]   I. Cimalla, F. Will, K. Tonisch, M. Niebelschütz, V. Cimalla, V. Lebedev, G. Kittler, M. Himmerlich, S. Krischok, J. A. Schaefer, M. Gebinoga, A. Schober, T. Friedrich, and O. Ambacher: "Impact of Device Technology Processes on the Surface Properties and Biocompatibility of Group III Nitride Based Sensors", Mat.-wiss. u. Werkstofftech. 37 (2006) 919-923.

[7]   G. Cherkashinin, V. Lebedev, R. Wagner, I. Cimalla, and O. Ambacher: "The performance of AlGaN solar blind UV photodetectors: responsivity and decay time", phys stat sol (c) 3 (2006) 243-247.

[8]   I. Cimalla, Ch. Förster, V. Cimalla, V. Lebedev, D. Cengher, and O. Ambacher: "Wet chemical etching of AlN in KOH solution", phys. stat. sol. (c) 3 (2006) 1767-1770.

[9] V. Lebedev, G. Cherkashinin, G. Ecke, I. Cimalla and O. Ambacher: "Space charge limited transport in AlGaN photoconductors", J. Appl. Phys. 101 (2007) 033705.

[10] V. Lebedev, K. Tonisch, F. Niebelschütz, V. Cimalla, D. Cengher, I. Cimalla, Ch. Mauder, S. Hauguth, O. Ambacher, F. M. Morales, J. G. Lozano, and D. González: "Coalescence aspects of III-nitride epitaxy", J. Appl. Phys. 101 (2007) 054906.

[11] I. Cimalla, F. Will, K. Tonisch, M. Niebelschütz, V. Cimalla, V. Lebedev, G. Kittler, M. Himmerlich, S. Krischok, J.A. Schaefer, M. Gebinoga, A. Schober, T. Friedrich, and O. Ambacher: "AlGaN/GaN biosensor—effect of device processing steps on the surface properties and biocompatibility", Sens. Actuat. B 123 (2007) 740–748.

[12] V. Cimalla, F. Niebelschütz, K. Tonisch, Ch. Foerster, K. Brueckner, I. Cimalla, T. Friedrich, J. Pezoldt, R. Stephan, M. Hein, O. Ambacher: „Nanoelectromechanical devices for sensing applications", Sens. Actuat. B 126 (2007) 24-34.

[13] V. M. Polyakov, F. Schwierz, I. Cimalla, M. Kittler, B. Lübbers, and A. Schober: „Intrinsically limited mobility of the two-dimensional electron gas in gated AlGaN/GaN and AlGaN/AlN/GaN heterostructures", J. Appl. Phys. 106 (2009) 023715.

[14] A. Schober, C. Augspurger, U. Fernekorn, K.-F. Weibezahn, G. Schlingloff, M. Gebinoga, M. Worgull, M. Schneider, Ch. Hildmann, F. Weise, J. Hampl, L. Silveira, I. Cimalla, and B. Lübbers: "Microfluidics and biosensors as tools for NanoBioSystems research with applications in the "Life Science"", Mater. Sci. Eng. B 169 (2010) 174–181.

[15] M. Gebinoga, L. Silveira, I. Cimalla, A. Dumitrescu, M. Kittler, B. Lübbers, A. Becker, V. Lebedev, and A. Schober: "Nanosensors for label-free measurement of sodium ion fluxes of neuronal cells", Mater. Sci. Eng. B 169 (2010) 182–185.

Book chapters

[16] M. Gebinoga, I. Cimalla, L. Silveira, M. Klett, V. Lebedev, K. Tonish, F. Niebelschütz, O. Ambacher, and A. Schober: "Response of nerve cell to inhibitors recorded by AlGaN/GaN field effect transistors", in: "Sensors for Environment, Health and Security - Advanced Materials and Technologies" (ed. M.-I. Baraton), Springer, Dordrecht, Netherlands, 2008, pp 311-316.

[17] I. Cimalla, B. Lübbers, V. Cimalla, M. Gebinoga, A. Schober, and O. Ambacher: "Group III-Nitride based sensors – Advances towards a new generation of biosensors", in: "Advanced Semiconductor Materials and Devices Research: III-Nitrides and SiC", (ed. Ho-Young Cha), Research Signpost Publishers, Trivandrum, India, 2010, p. 341-374.

[18] I. Cimalla, M. Gebinoga, A. Schober, V. Polyakov, V. Lebedev, and V. Cimalla: "AlGaN/GaN sensors for direct monitoring of nerve cell response to inhibitors", in: "Semiconductor device-based sensors for gas, chemical, and biomedical applications" (eds. F. Ren and S. J. Pearton), CRC Press, Boca Raton, London, Tokyo, 2011, p. 1-43..

Conference proceedings

[19] I. Cimalla, V. Lebedev, V. Cimalla, and O. Ambacher: "Investigation of the absorption behavior of thin layers of group III-nitrides by PDS and SRP", 48. Internationales Wissenschaftliches Kolloquium, 22.-25. 9. 2003, 05-01-06.

[20] V. Cimalla, Ch. Förster, I. Cimalla, R. Kosiba, G. Ecke, W. Schaff, H. Lu, R. Goldhahn, S. Shokhovets, A. Georgakilas, and O. Ambacher: "InN – ein Halbleiter mit weitem oder niedrigem Bandabstand?", 48. Internationales Wissenschaftliches Kolloquium, 22.-25. 9. 2003, 05-01-09.

[21] V. Cimalla, V. Lebedev, S. Linkohr, I. Cimalla, B. Lübbers, K. Tonisch, K. Brückner, F. Niebelschütz, M. Hein, and O. Ambacher: "Nitride based sensors", 17th Europ. Workshop Heterostruct. Technol. HETECH, Venice, Italy, November 3-5, 2008, pp. 33 – 40.

[22] I. Cimalla, M. Gebinoga, M. Klett, B. Lübbers, V. Lebedev, K. Tonisch, V. Cimalla, O. Ambacher, and A. Schober: "Bioreactor with integrated nanosensor for the recording of extracellular potential of nerve cells: response to inhibitors recorded with an AlGaN/GaN field effect transistor", NSTI Nanotech 1.-5. 6. 2008, Boston, USA, ISBN: 978-1-4200-8504-4, 566-568.

Further conference contributions

[23] I. Popa, V. Lebedev, V. Cimalla, and O. Ambacher: "Investigation of the absorption behavior of thin layers of group III nitrides by Photothermal Deflection Spectroscopy and Constant Photocurrent Measurement", Frühjahrstagung des Arbeitskreises Festkörperphysik (AKF) der DPG, Dresden, 24.03. - 28.03.2003

[24] I. Cimalla, V. Lebedev, V. Cimalla, and O. Ambacher: "Investigation of the absorption behavior of thin layers of group III-nitrides by PDS and SRP", 48. Internationales Wissenschaftliches Kolloquium Technische Universität Ilmenau 22.-25. September 2003, Session 5.1: GaN Based Crystals, Hetero- and Nanostructures, 05-01-06.

[25] V. Cimalla, Ch. Förster, I. Cimalla, R. Kosiba, G. Ecke, W. Schaff, H. Lu, R. Goldhahn, S. Shokhovets, A. Georgakilas, and O. Ambacher: „InN – ein Halbleiter mit weitem oder niedrigem Bandabstand?", 48. Internationales Wissenschaftliches Kolloquium Technische Universität Ilmenau 22.-25. September 2003, Session 5.1: GaN Based Crystals, Hetero- and Nanostructures, 05-01-09.

[26] V. Cimalla, Ch. Foerster, V. Lebedev, R. Wagner, I. Cimalla, J. Pezoldt, O. Ambacher, K. Brückner, R. Stephan, M. Hein: "Novel AlGaN and SiC based micro- and nanomechanical resonator beams", 13th European Heterostructure Technology Workshop HETECH 2004, October 3-6, 2004 Koutouloufari, Crete, Greece.

[27] I. Cimalla, Ch. Foerster, V. Cimalla, V. Lebedev, D. Cengher, K. Tonisch, and O. Ambacher: "Wet chemical etching of AlN in KOH solution", Intern. Symp. Comp. Semicond. (ISCS-2005), Sep 18 - 22, 2005, "Europa-Park", Rust, Germany, Mo P10.

[28] I. Cimalla, V. Cimalla, V. Lebedev, K. Tonisch, F. Will, O. Ambacher, E.S. Zaus, M. Eickhoff, A. Ababneh, H. Seidel, U. Schmid, Proc. 5th Intern. Workshop on Physical Chemistry of Wet Etching of Semiconductors (PCWES), Saarbrücken, (2006) 34.

[29] I. Cimalla, F. Will, K. Tonisch, M. Niebelschütz, M. Himmerlich, S. Krischok, V. Cimalla, G. Kittler, C. Kremin, M. Gebinoga, T. Friedrich and O. Ambacher: "Impact of the device technology processes on the surface properties and biocompatibility of group III nitride based sensors", EMRS 2006, May 29 to June 2, Nice, France.

[30] I. Cimalla, F. Will, K. Tonisch, V. Lebedev, M. Niebelschütz, M. Himmerlich, S. Krischok, V. Cimalla, G. Kittler, C. Kremin, T. Friedrich and O. Ambacher: „Impact of device processing on the surface properties and the biocompatibility of AlGaN/GaN HEMT sensors", 51st Internationales Wissenschaftliches Kolloquium Technische Universität Ilmenau, September 11 – 15, (2006) 299-300.

[31] O. Ambacher, B. Lübbers, I. Cimalla, V. Cimalla: "Extremely sensitive GaN-based sensors for monitoring of Bioreactions" (Invited Paper), SPIE Optics East, 9–12 September 2007, Seaport World Trade Center, Boston, Massachusetts USA.

[32] O. Ambacher, V. Cimalla, B. Lübbers, I. Cimalla, and A. Schober: "Extremely sensitive GaN-based sensors for monitoring of bioreactions (Invited Paper)", SPIE Photonics West 24–29 January 2009, San Jose, California, USA.

Patent

[33] M684-EP "Ladungsensitiver Halbleitersensor", 2008.

Theses

1. AlGaN/GaN heterostructures exhibit a number of superior properties compared to Si or conventional III-V semiconductors, which make them promising candidates for biosensors.

2. The passivation and good encapsulation of the sensor structure is a very important factor to achieve stability and reproducibility of the device in liquids such as electrolytes.

3. For good electrical stability and noise reduction of the biosensor signal, an electrically screened measurement setup with mechanically stable contacts and reliable implemented reference electrode is necessary.

4. In addition to their pH sensitivity, AlGaN/GaN FETs are sensitive to changes in Na^+ and K^+ ions flux.

5. The chemical reaction between titrated Na^+ and neuroinhibitors in the Na-free buffer SCZ can be recorded by the AlGaN/GaN sensor.

6. The group III nitrides are highly biocompatible and nerve cells adhere with high proliferation rate.

7. The media (electrolytes) used for cell-transistor coupling must have a stable pH value.

8. In cell media exposed to normal environment, spontaneous cell activity (breathing) can be monitored by the AlGaN/GaN sensor.

9. The nerve cell react on DFP and PMSF by keeping Na^+ channels in an open state and depletes positive ions in the cleft.

10. The nerve cell reacts on amiloride, which blocks of Na^+ channels. The reaction depends on the preliminary treatment.

11. The simulation of the ion fluxes supports the assumption that in the cell-transistor coupling experiments in this work Na^+ has the dominant effect in signal generation.